Radial Ion Transport in a Limited Axisymmetric ECR Plasma

by

Gerald Warren Gibson, Jr.

B.S. North Carolina State University, 1987

Submitted to the Department of Physics
in pa ial fulfillment of the requirements for the degree of

Doctor of Philosophy

at the
Massachusetts Institute of Technology
October 17, 1994

Signature of Author Gerald W. Gibson Jr.
Department of Physics
October 17, 1994

Certified by Herbert H. Sawin
Herbert H. Sawin
Joint Professor of Chemical and Electrical Engineering
Thesis Supervisor

Accepted by George F. Koster
George F. Koster
Chairman, Departmental Graduate Committee

Radial Ion Transport
in a
Limited Axisymmetric ECR Plasma

by

Gerald Warren Gibson, Jr.

Submitted to the Department of Physics
on October 17, 1994 in partial fulfillment of the
requirements for the degree of
Doctor of Philosophy

Abstract

An experimental study of the radial transport of ions in the presence of a limiter for an axisymmetric plasma sustained by the resonant absorption of 2.45 GHz whistler waves is presented. In steady state, approximately 30% of the particles ionized in the core plasma flow radially into the scrape-off layer. The magnitude of radial ion flux is observed to be bounded from below by the radial electron transport rate and from above by the classical collisional ion transport rate of the cold *edge* ions. The system proves to be susceptible to a Kelvin-Helmholtz instability.

The transport experiments were performed at a set input power of 300 W and over the neutral pressure range of 1-3 mTorr in Argon gas. The bulk ions possess a typical temperature of 1eV and do not obey a diffusion equation in the core plasma. Strong radial electric fields are observed and appear to provide the principal means by which radial ion diffusion is controlled.

The presence of strongly sheared electric fields in this system excites a hydrodynamic instability of the Kelvin-Helmholtz type. The most frequently observed mode is driven by a region of depressed potential at the plasma edge. A theory for instability in the presence of a localized inverted Gaussian radial potential is presented and compared with experimental measurements. The convection of edge plasma into the core under influence of this mode leads to an increased edge temperature and, hence, enhanced axial losses from the scrape-off layer, thereby modifying the radial profile of the scrape-off layer.

Thesis Supervisor: H.H. Sawin

Acknowledgements

Reflecting upon those who have helped in this endeavor comprises the most enjoyable aspect, by far, of thesis preparation. First, I thank my thesis supervisor Professor Herbert Sawin, who has overseen this project from its inception. Herb has greatly influenced my approach to experimental research problems, and it is no understatement to say that what I know of engineering design has been learned from him. Thanks also are due to Donna Smatlak and Barton Lane who provided early tutelage in plasma physics research. Members, past and present, of the METL group have enriched these graduate school days immeasurably. Those who have served as friends, mentors and foils are: John Arnold, Bill Conner, Tony Chiang, Tim Dalton, Dave Gray, Gil Huppert, Linda Kiss, Scott Lawing, Joanne Liu, Vivek Mohindra, Frank Ross, Igor Tepermeister, Colin Wolden and Gavin Zau. Special thanks go to John Cremin, from whom I learned the art of machining.

Various teachers deserve credit for what has been accomplished herein. Suzie Thrift and Frances Thompson first awakened me to the beauty of mathematics and physics, respectively, and are largely responsible for my choice of a career in science. Professor Dale Sayers took time out of a heavy state school teaching load to encourage and challenge an enthusiastic sophomore (and to badger him into picking up a second major in physics). I thank Professor Miklos Porkolab for serving on my thesis committee. Professor Porkolab introduced me to the remarkable zoo of collective modes in plasmas and provided invaluable assistance in the identification of the Kelvin-Helmholtz mode which was studied in this thesis. Professor George Bekefi also served on this thesis committee and has been, since his days as my graduate advisor, a continual source of excellent suggestions and insights regarding my research.

None of this work could have been accomplished without the friendship and support of a number of people who are entirely unrelated to physics or M.I.T. First, I thank my mother and father. In a very real sense, this thesis is a paean to the virtues of work ethic and the love of nature which they instilled in me. My brother Murray has always served as comrade and confidante, and to this day I rely on his uncommon good sense when the way doesn't seem clear. My sincere thanks go to my inlaws, the McClungs, who have been nothing short of family for the last five years, and especially to Jim, Judy and Kathy for their hospitality in these last hectic weeks. Finally, and most importantly, I thank my wife Maura for her understanding and support during what was our first year of marriage and *our* last year of graduate school. She has added an essential dimension to my life which I had no idea was missing.

Contents

1 Introduction 10

1.1 Background 10

1.2 Previous Work 12

1.3 Problem Statement 14

1.4 Thesis Organization 15

2 The Radial Ion Transport Experiment 17

2.1 Basic Systems 17

2.2 Diagnostics and Data Acquisition 21

3 Ion Transport Theory 33

3.1 Transport Coefficients 33

3.2 Transport Mechanisms 44

3.3 Transport Equations 49

3.4 Kelvin-Helmholtz Instability 54

4 Experimental Method 61

4.1 General Experimental Considerations 61

4.2 Quantitative Transport Measurements 66

5 Experimental Results 80

5.1 Experimental Observations 80

5.2 Experimental Determination of Ion Transport 93

5.3 Kelvin-Helmholtz Instability 117

6 Conclusions 126

6.1 Summary of Results 126

6.2 Future Work 130

A Instrumentation 132

List of Figures

2-1 Experimental Apparatus 18
2-2 Microwave Antenna and Tuning 19
2-3 Single Langmuir Probe Construction 22
2-4 Single Langmuir Probe Access 22
2-5 Floating Double Langmuir Probe Construction 24
2-6 Signal Generation and Data Acquisition for Floating Double Langmuir Probe 24
2-7 Current-Voltage Trace for Floating Double Langmuir Probe . . . 26
2-8 Retarding Field Ion Energy Analyzer Construction 28
2-9 Ion Energy Distribution Function 28
2-10 Plated Collector for Retarding Field Ion Energy Analyzer 31
2-11 (a) RFA Data Acquisition via A/D Board (b) RFA Fast Sweep Data Acquisition 32

3-1 Theoretical Ion Diffusion Coefficients 39
3-2 Schematic of Ion Transport 48

4-1 Diagnostic Access (a) View Along Axis (b) View From Side . . . 62
4-2 Magnetic Field Topologies 67
4-3 Bimodal Ion Energy Distribution Function 75

5-1 Global Plasma Behavior in Pressure-Power Parameter Space . . . 81

5-2 Floating Potential Fluctuations Associated With Region U1 (of Figure 5-1) 84
5-3 Floating Potential Fluctuations Associated With Region U2 (of Figure 5-1) 84
5-4 Normalized Axial Profiles Before and After Mode Transition . . . 87
5-5 Variation of Plasma Density and Electron Temperature with Microwave Power for 3.0 mTorr Neutral Pressure 89
5-6 Variation of Plasma Parameters with Neutral Pressure at 300 W 90
5-7 (a) Variation of Ion Temperature with Neutral Pressure (b) Peak Normalized IEDF's at 3.0 mTorr 92
5-8 (a) Pressure Variation of Ion Flux at 300 W Microwave Power (b) Microwave Power Variation of Ion Flux at 3.0 mTorr 94
5-9 (a) Pressure Dependence of Ion Confinement Times at 300 W (b) Power Dependence of Ion Confinement Times at 3.0 mTorr 95
5-10 Radial Dependence of Electron Temperature for 3.0 mTorr and 300 W 97
5-11 FDP Trace in the Outer Edge of the Scrape-Off Layer 98
5-12 Radial Dependence of Plasma Potential for 2.0 mTorr and 300 W 100
5-13 Radial Variation of Plasma Density for 2.0 mTorr and 300 W . 102
5-14 Parallel Ion Flux to the Wafer Mapped back to the Midplane for 3.0 mTorr and 300 W 104
5-15 Radial Variation of Ion Temperature for 3.0 mtorr and 300 W . 105
5-16 Ionizations per Second in a Cylindrical Shell 106
5-17 Ionizations Within and Parallel Ion Flux Out of a Cylindrical Shell for 3.0 mTorr and 300 W 107
5-18 Number of Electron-Electron-Ion Recombinations per Second in a

Cylindrical Shell at 3.0 mTorr and 300 W 109
5-19 Radial Variation of Neutral Temperature due to Ion Heating .. 111
5-20 Radial Variation of Neutral Density due to Ion Heating 111
5-21 Total Radial Ion Flux versus Radius 113
5-22 Ratio of Radial Flux into Scrape-Off Layer to Axial Flux from the Core Plasma 115
5-23 Radial Potential Step Voltage versus Pressure 115
5-24 Radial Density Profiles Normalized to Unity at the Edge of the Scrape-Off Layer 116
5-25 Floating potential on Two Probes Separated by 90° in Azimuth 118
5-26 Radial Profile of Peak to Peak Fluctuation Level 118
5-27 Pressure Dependence of Mode Frequency 119
5-28 Pressure Dependence of Edge Density 119
5-29 Ion Temperatures in the Scrape-Off Layer in the Presence Of Instability 121
5-30 Potential Well in the Scrape-Off Layer 122
5-31 Theoretical and Experimental Values for Kelvin-Helmholtz Instability Frequency 124

6-1 Radial Variation of Radial Ion Flux 127

A-1 High-Bandwidth Floating Current Amplifier for RFA 133
A-2 Current and Voltage Measurement Circuit for FDP 135

List of Tables

3.1 Typical Parameters for the Ion Transport Experiment 36

4.1 External Variables for the Ion Transport Experiment 65

5.1 Classification of the Collective Modes observed in the Ion Transport Experiment 83

Chapter One

Introduction

1.1 Background

In the last two decades, the application of plasmas to disparate materials processing problems has undergone substantial growth. At present, plasmas are being used to deposit and/or remove materials as different as copper, SiO_2, polymers, and diamond, and provide the principal means by which semiconductor products are fabricated in industry. The popularity of plasma processing derives from the unique ability of the plasma state to drive non-equilibrium processes. In etching applications, the relatively hot electrons of the plasma dissociate molecular gases such as Cl_2 or C_2F_6, producing a high fraction of radicals in a gas which remains at or near room temperature, which is many orders of magnitude below temperatures necessary for substantial thermal dissociation. At the surface where etching proceeds, the flux of energetic ions which have fallen through the sheath drive non-equilibrium surface chemistry and sputter material away. With careful control of the process, structures possessing dimensions of a fraction of a micron are routinely created.

The essential role of the ions which impinge upon the surface being processed is to provide energy flux along the macroscopic surface normal. Surfaces receiving directed ion energy tend to etch the fastest, and since one is typically interested in etching deep, narrow features ("trenches") the ratio of normal energy to lateral energy spread of incident ions represents an oft used

figure of merit. Given a thermal distribution of ions, and a collisionless sheath, it should be possible to render the mean impingement angle arbitrarily small by biasing the workpiece relative to the vacuum chamber. However, as device dimensions shrink, damage to these small structures from energetic ions becomes evermore problematic, so that one would like to operate under conditions of minimal ion temperature. It is therefore of great importance to ascertain the ion temperature in processing plasmas.

At the macroscopic level, whatever process might be occurring on the workpiece should proceed at a uniform rate across it. A typical semiconductor wafer of 8 inch diameter is subdivided into hundreds of identically patterned 1 cm square dies. Each die is a complicated structure composed of layers of metal, semiconducting, and dielectric material. These layers can be as thin as 100 Å or less, and it is often necessary to etch through a 1 micron layer of another material before stopping upon this thin layer. Thus, the macroscopic uniformity of etch is of extreme importance. In state of the art etching chemistries such as HBr, the requirements of ion flux uniformity may be less stringent than once had been thought [Gibson et al., 1994], but it is difficult to imagine marketing a plasma source which possesses less than +/-5% ion flux uniformity across its working area. Macroscopic uniformity of ion flux is of importance for another reason. Local imbalance of ion and electron fluxes can lead to potential differences across a wafer surface which, in turn, damage delicate dielectric structures such as field effect transistor gates. By these considerations, one can hardly overestimate the importance of understanding ion transport in plasma processing systems.

1.2 Previous Work

Plasma sources which employ the resonant absorption of whistler waves have been used commercially in Japan for over a decade. It was only in the late 1980's, however, that ECR sources began to receive attention in the United States. Early research suggested that ion and neutral temperatures in these sources could be as high as 3 and 0.2 eV, respectively [McKillop et al., 1989]. These claims were made on the assumption that the observed emission line-widths were due entirely to Doppler broadening. More detailed analysis, performed at AT&T Bell Telephone Laboratories, which utilized Doppler Shifted Laser Induced Fluorescence (LIF) techniques, showed that perpendicular ion temperatures were typically 0.5 eV and neutrals <0.1 eV [Nakano et al., 1991], [Sadeghi et al., 1991]. From several isolated observations of radial ion flow, the Bell Laboratories group also determined that ions followed the magnetic field lines to a good approximation. One significant caveat to the interpretation of these results is that the LIF was performed on a metastable ion for which the collisional cross-sections are unknown. Also, the LIF measurements were made at only a few different locations in the plasma so that radial and axial profiles were not determined.

The absorption of microwave power by the plasma has been investigated in some detail by Stevens, Cecchi and others at Princeton [Stevens, et al., 1992], who used rf probes to measure the microwave fields interferometrically. They showed that the microwave power is absorbed over a typical axial distance of several centimeters (depending upon magnetic field gradient and plasma density) and at magnetic field values near, but above, that corresponding to nominal electron cyclotron resonance (875 G). They also performed rudimentary ray tracing calculations which were solved self-consistently with a

local plasma density model in order to understand the effects of power deposition upon radial profile control. The qualitative results of their investigation showed that the whistlers refract toward regions of low density, thereby smoothing out radial non-uniformity in a self-consistent manner, since the proportionality of local density to incident power was assumed.

The most detailed numerical simulation of ion transport in ECR sources which has been performed to date is the hybrid code of Porteous, Wu and Graves [Porteous, et al., 1994]. This code self-consistently couples a fluid electron model to a Particle-in-Cell (PIC) ion trajectory calculation. The ion trajectories near the plasma edge are shown to have significant cross-field components for conducting boundary conditions, but also possess anomalously high energies (compared to experimental values) which apparently result from large electric fields near the plasma edge. The major short-comings of this code were: (1) the electrons were allowed to flow only along magnetic field lines, (2) the microwave power deposition profile was not determined self-consistently, (3) ion-ion collisions were not taken into account, and (4) ion and neutral transport were decoupled.

It has been noted by the author, as well as by others [Samukawa, 1994] that ECR sources are susceptible to low frequency, apparently hydrodynamic, fluctuations and collective modes, especially for neutral pressures near and below 1 mTorr. Because these modes are observed to propagate azimuthally, and at frequencies between 1 and 10 kHz, they may well influence ion transport and plasma uniformity.

1.3 Problem Statement

The investigations outlined in the previous section have provided information bearing on ion transport in ECR sources which is of the highest quality. However, to date, a comprehensive study of ion transport which determines the source and sink functions as well as the particle flows as functions of spatial position has not been undertaken. Such studies are urgently needed for comparison with engineering design models. To this end, we have determined to perform accurate, *local* measurements of all the relevant plasma parameters, including plasma density and potential, electron and ion temperatures, neutral density and ion fluxes. With a complete set of experimental numbers in hand, the question of radial ion transport can be addressed in an unambiguous manner.

The experiment has been constructed to possess simple, well defined boundary conditions which also accurately reflect those found in industrial plasma sources. Specifically, the chamber is cylindrical with all surfaces insulating except for the down-stream axial boundary which is conducting and held at ground potential. The addition of an annular quartz limiter at the resonance zone represents a departure from industrial construction, but creates a scrape-off layer which provides a wealth of information on the behavior of plasma in this regime of fractional ionization (5-10%), and moderate density (10^{17}-10^{18} m^{-3}) and magnetic field (500-1000 G).

The specific question to be answered by this thesis is: to what extent do ions, which are not strongly magnetized, stream across the magnetic field lines? En route to making this determination, subsidiary questions will be answered, a number of which possess importance outside of the specific ion transport issue. Among these are:

- What is the ion temperature?
- What is the magnitude and radial uniformity of plasma potential?
- What are the radial profiles of neutral density and temperature?
- What physical mechanism drives the low frequency plasma oscillations?

The importance of the first and second of these questions was touched on in the first section of this chapter. The observation that neutral temperature and density may not be radially uniform in the presence of collisional heating by ions originates with this thesis, and is of generic applicability to high density (10^{18} ions/cm^3) plasma sources. The final query, though of practical importance, stands on its own as a question of inherent scientific interest.

1.4 Thesis Organization

This thesis is organized into six chapters and an Appendix. Chapter One, Introduction, provides a general motivation for, and a specific statement of the thesis problem. Chapter Two, The Ion Transport Experiment, provides detailed information on the experimental apparatus, its operation, and the diagnostics which have been employed in this thesis work. Chapter Three, Ion Transport Theory, provides background information on the relevant physical processes encountered in these experiments, derives transport equations for electrons and ions, and outlines the theory for a Kelvin-Helmholtz type instability which is suspected to cause the observed low frequency plasma oscillations. The fourth chapter, Experimental Method, explains how each physical quantity required for evaluation of the ion transport equation is determined; it also provides calculations of experimental error for each of these measurements. The results of the ion transport experiment are given in

Chapter Five, Experimental Results, and the meaning of these measurements is discussed. A summary of this thesis work is provided in Conclusions, Chapter Six. The Appendix provides information on instruments which have been designed and utilized in the course of this work.

Chapter Two

The Radial Ion Transport Experiment

This chapter will consist of two sections, each describing a separate aspect of the overall experiment. The first section will detail the basic equipment which comprises the experiment. The second contains information on both the various diagnostics which have been utilized in this thesis and the data acquisition system.

2.1 Basic Systems

An overall schematic of the basic experimental apparatus of this thesis is given in Figure 2-1. Power is coupled into the plasma via electron cyclotron resonance (ECR) absorption of high-field launched whistler waves propagating at a frequency of 2.45 GHz. The magnetic field which supports the whistlers is generated by two solenoidal water-cooled magnets, each of which is powered by its own c.w. current source and which, when operated in tandem, can place the resonance zone at any desired axial position. The microwaves are generated c.w. by a magnetron and launched from a cylindrical dipole antenna (Figure 2-2) through a quartz vacuum window upon which the plasma terminates. The nominal mode for the cylindrical dipole is TM_{01}. Under normal operating conditions the antenna excites whistler waves in the plasma which are resonantly absorbed. The whistler waves possess wavelengths of approximately one centimeter. The magnetron is controlled by an ASTeX S-1500 power supply which provides both the tungsten filament cathode bias

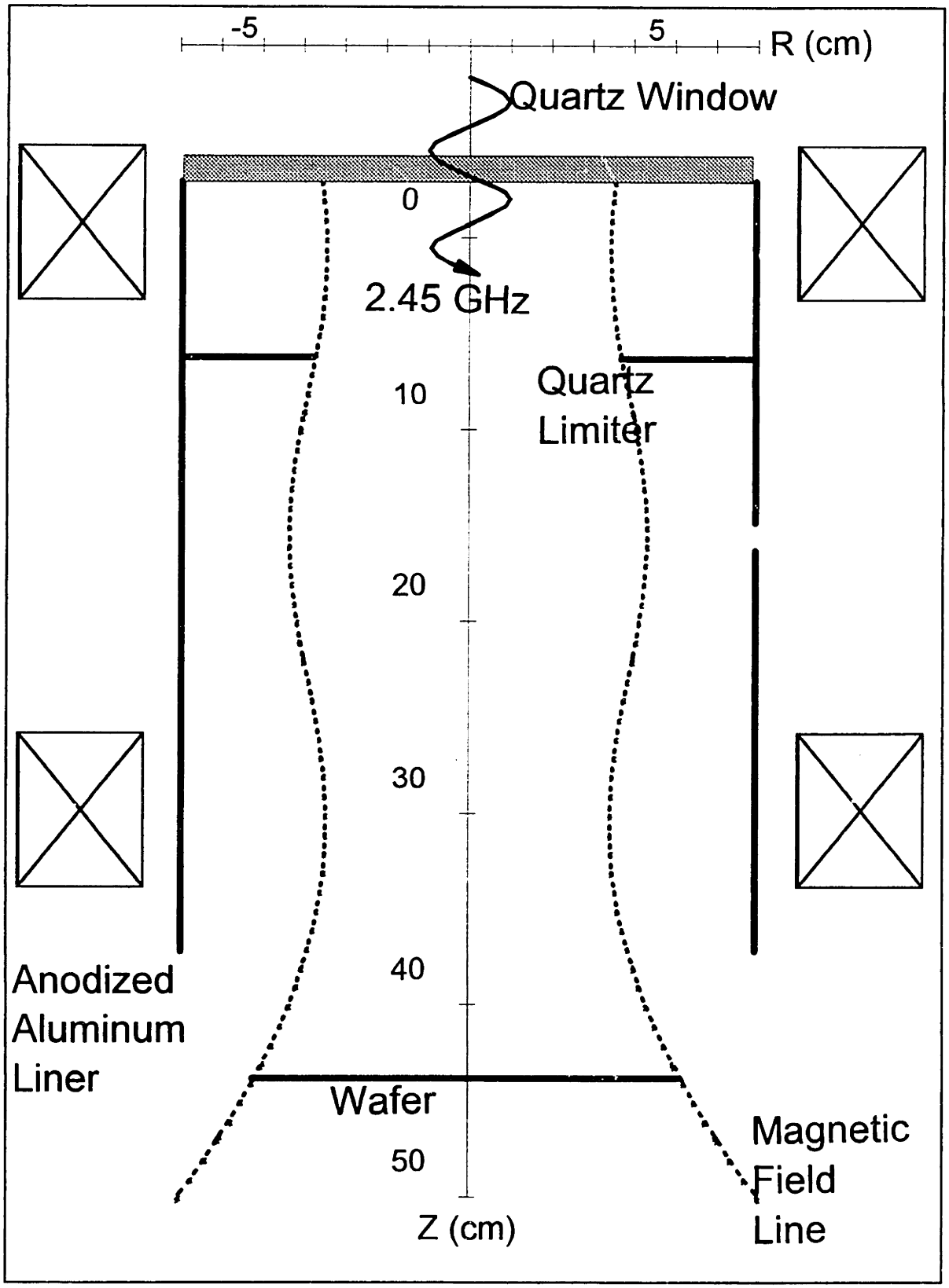

Figure 2-1: Experimental Apparatus

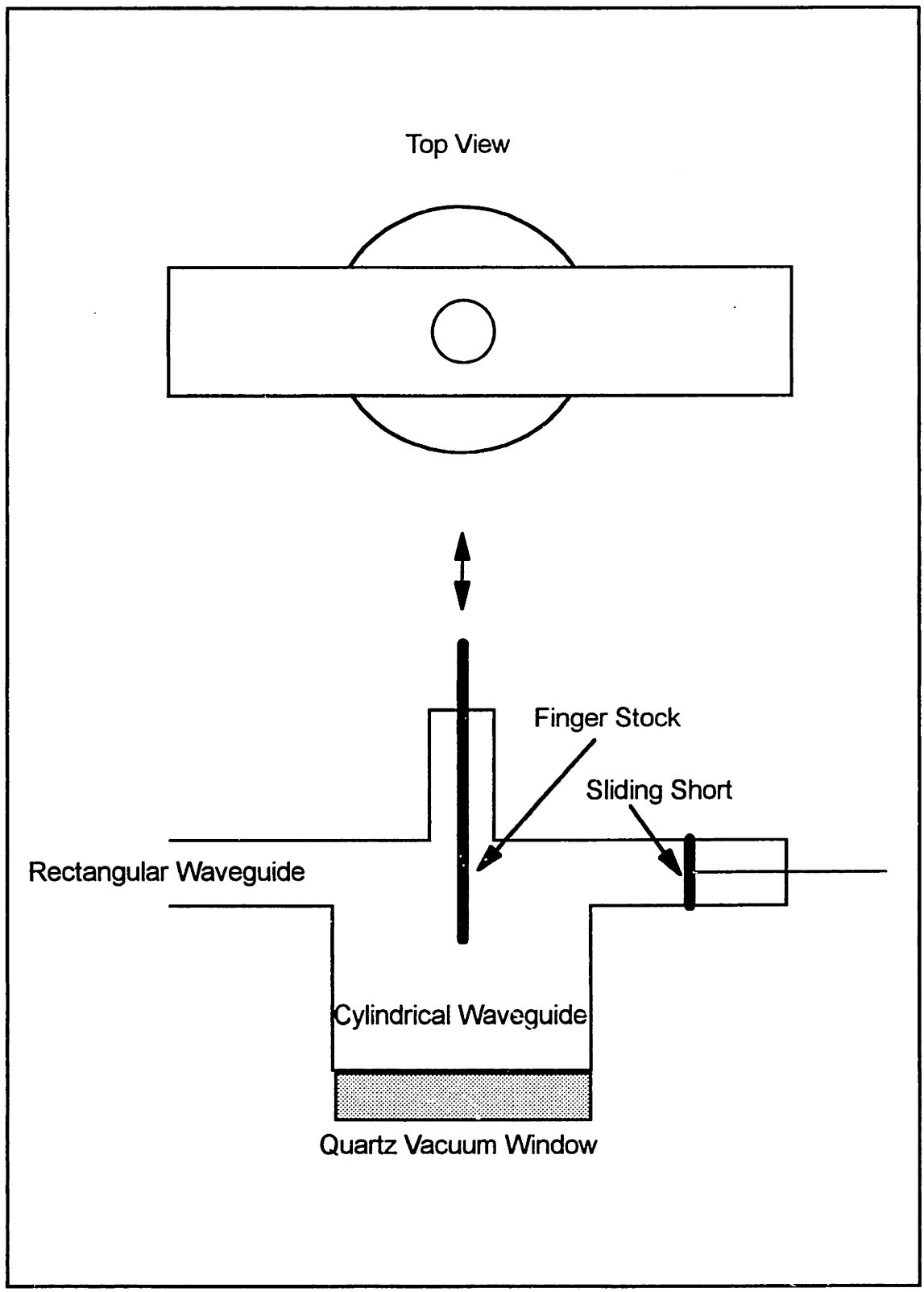

Figure 2-2: Microwave Antenna and Tuning

voltage (3000 V) and a variable source of regulated current (0.1%) to the filament. Microwave power can be varied over the range of 300-1500 W. Reflected power is sampled by a directional coupler and detected by a diode. The entire rf system and magnets are a commercial unit which is marketed by ASTeX.

Vacuum for the system is maintained by a 1500 l/s cryo-pump (CT-8). An ionization gauge and a capacitance manometer monitor base pressure and neutral pressure respectively under experimental conditions. Base pressures for the system are typically 10^{-7}-10^{-8} Torr while experiments are run at neutral pressures between 0.5-3.0 mTorr. The working gas for these experiments has been argon, and the flow of this gas is controlled by a 100 sccm mass flow controller (Unit Instruments U-100). The gas is introduced into the chamber from an annular array of orifices positioned around the outside diameter of the microwave window.

Between the plasma and the wall of the water-cooled 304 Stainless Steel vacuum vessel is an anodized aluminum liner. Such liners are typically used in plasma sources to minimize the sputtering of metal atoms from chamber walls, which may contaminate the surface of the material to be processed. A chromel-alumel thermocouple is placed in thermal contact with the liner in order to monitor the approximate neutral gas temperature. At an axial distance of 7.5 inches below the quartz microwave window, a quartz limiter of i.d. 3 inches is installed. It creates a scrape-off layer in the region between the magnetic flux surface which contacts its inner edge and the anodized aluminum liner. As a practical matter, the limiter drastically reduces both heat flux to, and sputtering of, the liner wall. The plasma terminates down-stream on an aluminum disk which simulates the silicon wafers often processed by such sources. This disk can be moved axially without breaking vacuum and presents

the plasma with its only ground reference. It is important to stress that, excepting the limiter, the physical boundaries encountered by the plasma in these experiments are typical of those occurring in numerous types of industrial plasma processing reactors, so that the gross behavior and trends which appear should be generic to ECR plasma processing sources.

2.2 Diagnostics and Data Acquisition

There are three basic diagnostics which have been utilized in this experimental study: single Langmuir probes for monitoring plasma fluctuations, a floating double Langmuir probe for monitoring electron density, electron temperature and estimating the plasma potential, and a miniature retarding field ion energy analyzer of novel design which is capable of measuring ion temperatures with sub-eV resolution at a repetition rate of 20 kHz in plasmas as dense as 10^{12} cm^{-3}. Below, a sub-section will be devoted to each of these diagnostics. Each sub-section will include a description of the design and fabrication of, and data acquisition system for the diagnostic.

Single Langmuir Probes

The materials and construction of the single Langmuir probes used to monitor plasma fluctuations and collective phenomena are illustrated in Figure 2-3. A center conductor of 0.003" diameter Tungsten wire is insulated from an 0.040" diameter 304 stainless steel ground-shield with a 0.020" diameter Al_2O_3 tube. A 0.05" tip of Tungsten wire is left exposed to the plasma. The entire probe assembly resides within an Al_2O_3 sleeve of outer diameter 0.060". The sleeve prevents the conducting ground-shield from serving as a low-impedance

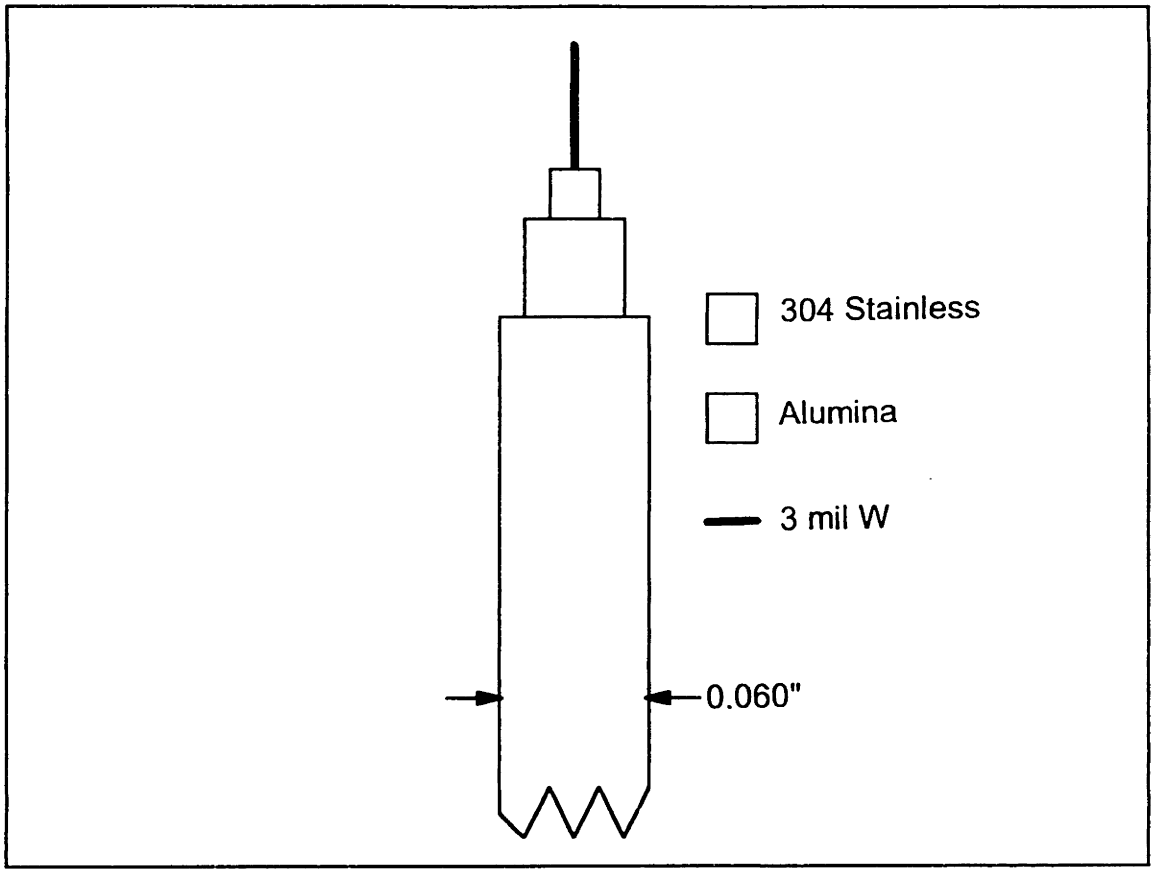

Figure 2-3: Single Langmuir Probe

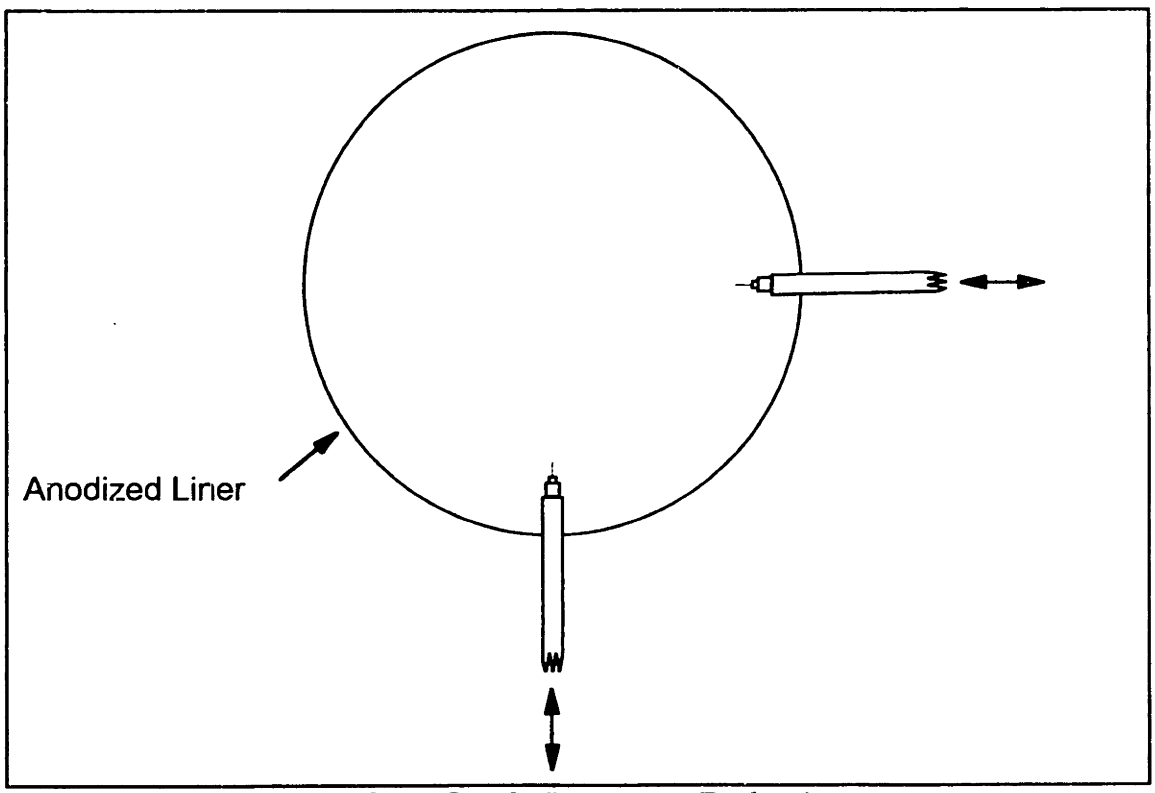

Figure 2-4: Single Langmuir Probe Access

path for plasma current across magnetic field lines. The probe dimensions have been minimized to the greatest possible extent in order to avoid perturbation of the plasma. Two identical probes accessed the plasma system at the mid-plane with an azimuthal separation of $\pi/2$ as shown in Figure 2-4, and monitor the plasma floating potential. Each can be moved radially to any position between the magnetic axis and the anodized aluminum liner. Each of the probes is connected to a 10 MΩ input of a LeCroy 9414 four channel 150 MHz digital storage oscilloscope which, in turn, is connected to a personal computer (80286 CPU) and mass storage via an IEEE 488 GPIB interface. Thus, both fluctuation spectra and azimuthal phase information can be acquired. Furthermore, fourier spectra can be taken in real time through the Fast Fourier Transform hardware which resides in a second (Lecroy 9400) two channel 150 MHz DSO. The computer control of the oscilloscopes comprises part of an overall data acquisition code which acquires and stores all data used in this thesis.

Floating Double Langmuir Probe

The preponderance of insulating boundaries in the experiment led to difficulties with shifting plasma ground reference when single Langmuir probes were used to measure electron temperature and density. As a result these parameters were measured by a floating double Langmuir probe (FDP), which was found to give superior results. Indeed, as will be discussed in Chapter 4, the FDP yielded measurements of electron density and temperature which were in excellent agreement with Thompson scattering data from a similar experiment. The materials and construction of the FDP are shown in Figure 2-5. The probe tips were identical 0.1" x 0.020" diameter tungsten and were

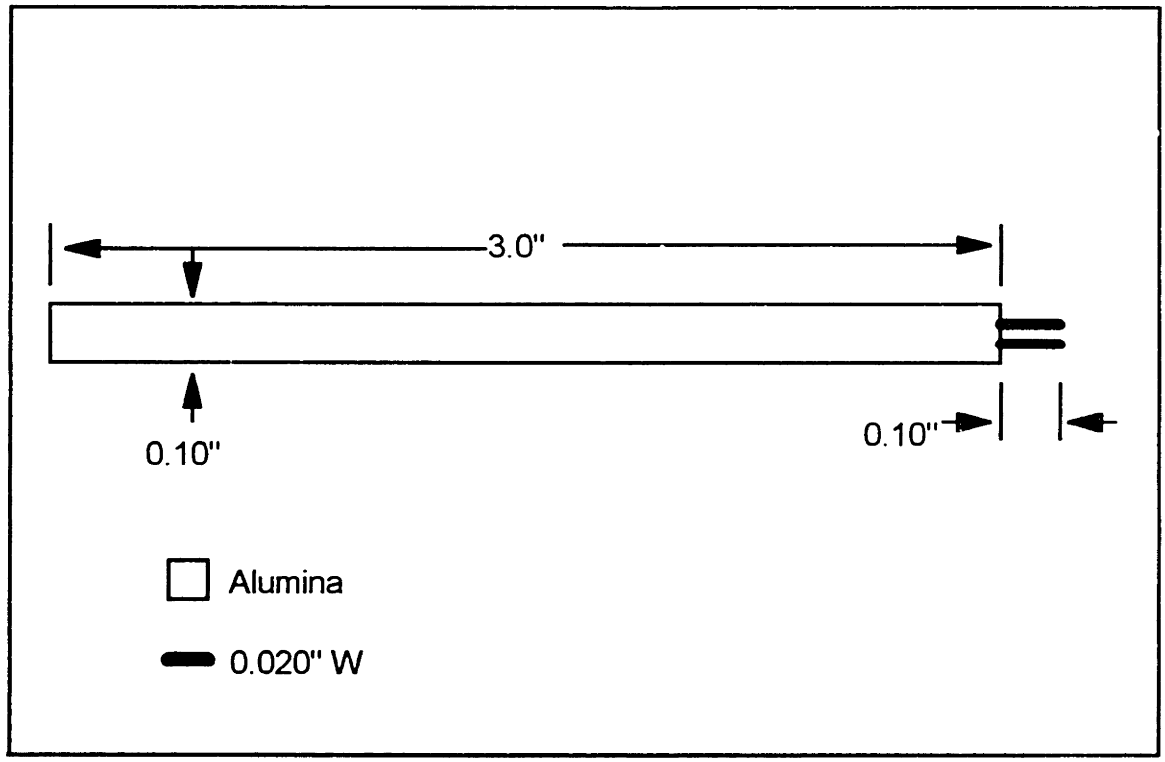

Figure 2-5: Materials and Construction of Floating Double Langmuir Probe

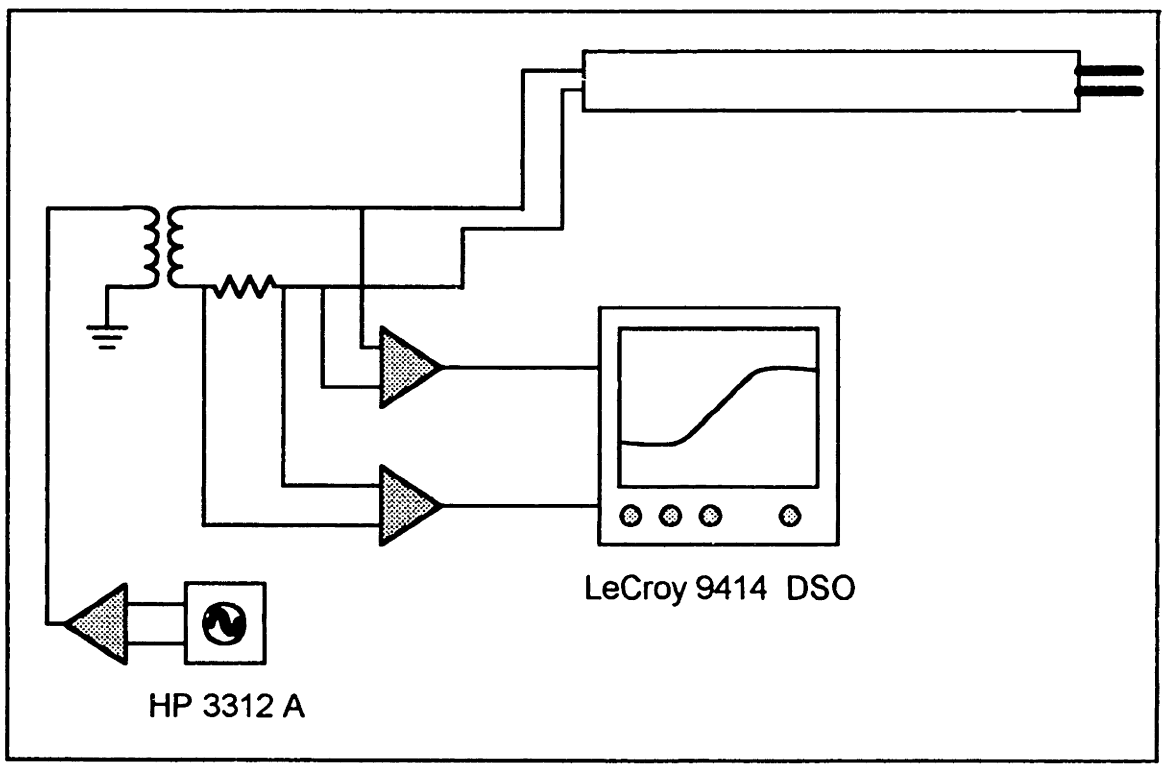

Figure 2-6: Signal Generation and Waveform Acquisition
for Floating Double Langmuir Probe

housed in an Al_2O_3 sleeve. Two such probes were built. The first accessed the plasma through a compression seal feedthrough mounted on one of the four mid-plane ports (Figure 4-1a) and could be scanned radially from the magnetic axis to the liner wall. The second had access from the endflange and was mounted on a dog-leg as shown in Figure 4-1b. It could thus be moved both axially and radially.

Figure 2-6 illustrates the operation of the FDP. A 100 Hz sinusoidal differential voltage (produced by an HP 3312A function generator) is coupled to the FDP tips via a transformer. The voltage on each conductor, and the current which flows between them, is monitored by an electronic circuit which is detailed in Appendix A. The conductor voltages are read off by separate, identical, high impedance voltage followers which, in turn, feed into a differential amplifier. The current is measured by a floating current to voltage circuit which has gain adjustable over three decades so that dynamic range is not forfeited as the diagnostic is scanned across the plasma radius and into the scrape-off layer. The current and voltage signals are acquired by the Lecroy 9414 and stored. Electron temperature and density are determined from the current versus voltage (I-V) characteristic by fitting the experimental data with the functional form [Chen, 1965]

$$I = I_s \tanh\left(\frac{V}{2T_e}\right) \quad , \qquad (2.1)$$

where I_s is the ion saturation current to one probe tip and T_e is in eV. This functional form assumes a Maxwellian velocity distribution of electrons, which for usual operating conditions is an excellent assumption. A typical I-V characteristic along with its fit is shown in Figure 2-7. Under conditions of large amplitude plasma fluctuations such clean fits were obviously not possible.

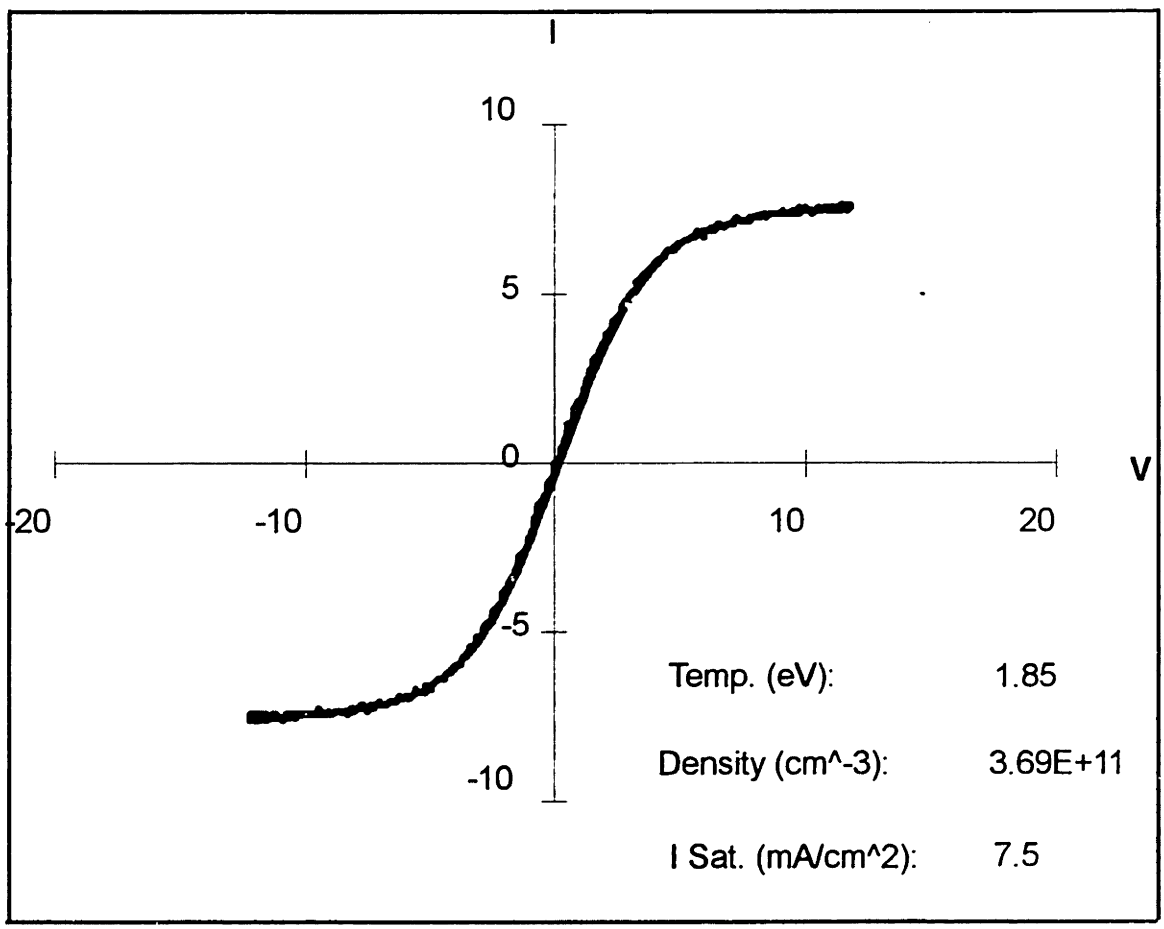

Figure 2-7: Current-Voltage Trace for Floating Double Langmuir Probe with Fit.

Also, for the coldest electrons (<0.5 eV) found at the extreme outer edge of the scrape-off layer, the functional form shown above gave a less than perfect fit to the I-V characteristic. The meaning of this departure from ideal behavior will be discussed in Chapter Five.

Retarding Field Ion Energy Analyzer

In the course of this work, a miniature Retarding Field Ion Energy Analyzer (RFA) of novel design and an unprecedented combination of spatial, temporal and energy resolution has been conceived and implemented. A schematic drawing of the RFA is shown in Figure 2-8. Ions and electrons, having fallen through the sheath in front of the RFA, impinge on the grounded metal (gold) face-plate and pass through the orifice, which has 0.040" diameter and is backed with 2000 line/inch electro-formed Ni mesh (Buckbee-Mears). The mesh is required since debye lengths as small as 10 μm are encountered in these plasmas. A single, negatively biased grid (2000 lines/inch Ni) serves as an electron repeller and to return secondaries back to the collector. The collector is connected to a variable voltage source through a floating picoammeter (Keithley 488), and thus serves as the ion discriminator. Because of the low plasma potentials (~15 V) and electron temperatures (~2 eV) of this experiment, few secondaries are generated at the electron repeller grid (typically biased to -30 V), and most of those are created on the front surface so that they flow to the face-plate and not to the collector. Although the RFA is an inherently invasive diagnostic, it possesses physical dimensions (Figure 2-8) which are small on the scale of both axial and radial plasma gradients, and can achieve spatial resolution of ion energy distribution functions (IEDF's) of ~3mm.

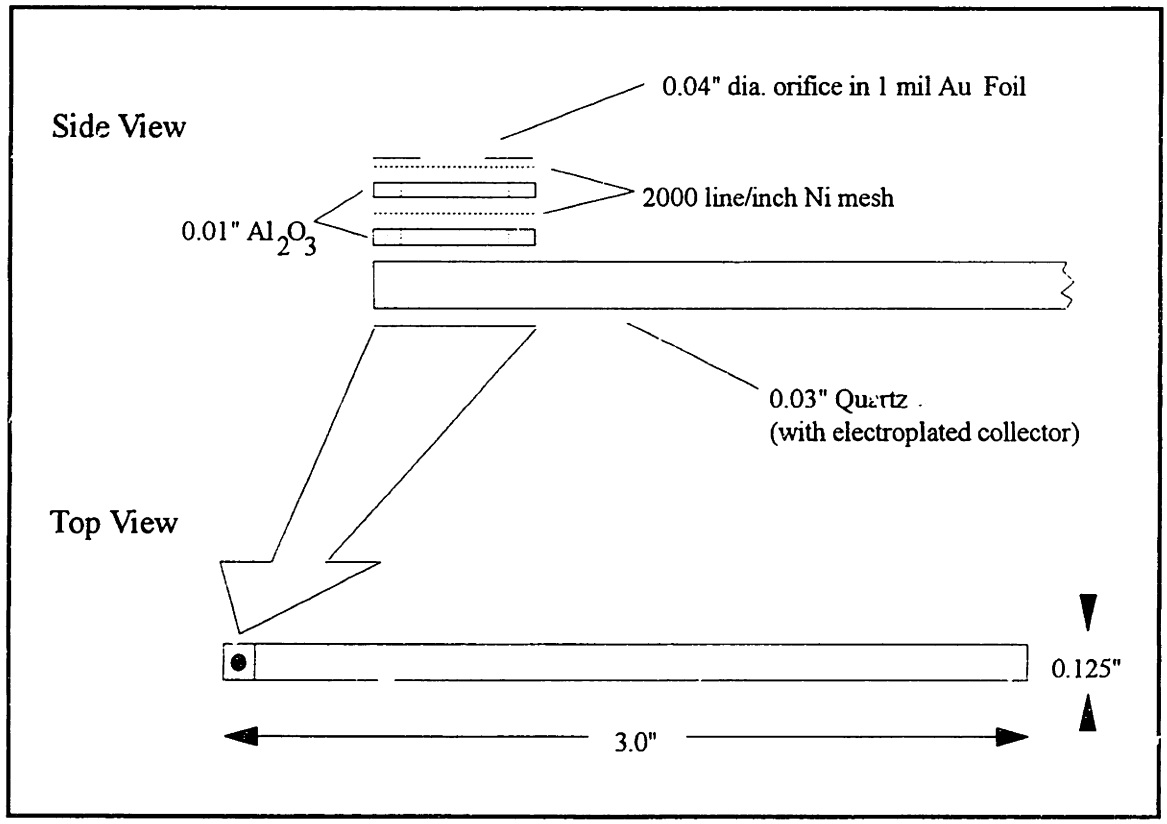

Figure 2-8: Retarding Field Ion Energy Analyzer Materials and Dimensions

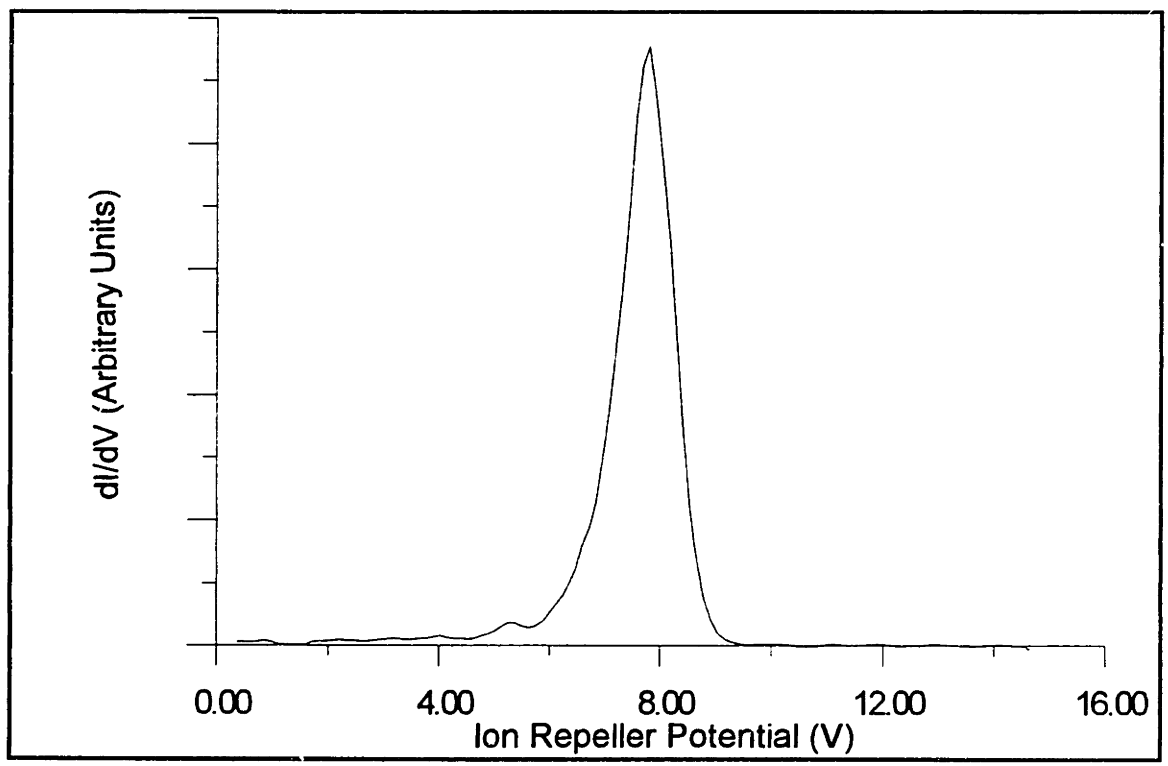

Figure 2-9: Ion Energy Distribution Function Acquired by Retarding Field Energy Analyzer

The RFA's diminutive size is, in fact, a byproduct of energy resolution requirements. The usual RFA design criterion on energy resolution requires that inter-grid spacing not exceed the Debye length within the analyzer [Hutchinson, 1986] if space-charge corruption of the IEDF is to be avoided. In the present case, space-charge effects should be most severe in the region between the electron repeller and the collector where only ions flow. In that region the ion flux has been reduced from that at the orifice by a factor of ~ 10 due to attenuation by the two grids (transmission 0.36), and average density is, furthermore, less than that in the bulk plasma due to the constraints of continuity ($\nabla \cdot nv = 0$). Thus, an inter-grid spacing of several hundred μm is required if maximal energy resolution is to be achieved. Figure 2-9 shows an IEDF which has been acquired under typical conditions and illustrates the RFA's ability to resolve sub-eV IEDF's. The measured IEDF's always represent an upper bound on energy spread since a certain amount of broadening in the pre-sheath is inevitable. Two pieces of evidence, however, suggest that this effect is minimal. First, the full width at half maximum (FWHM), which we measure is greater than, but within a factor of 2 of , Doppler shifted laser induced fluorescence measurements of perpendicular ion temperatures made in an identical source under similar conditions and is in nearly exact agreement with streaming ion energy spreads measured by the LIF technique. Second, we have been able to observe the decay of FWHM from $\sim$1eV to $\sim$0.3eV in a region where plasma density remained nearly constant, and electron temperature *dropped* precipitously, which indicates that neither collisional nor space-charge broadening occurs to a significant degree in these measurements.

As noted in the introduction, low frequency, large amplitude (typically 1V p-p at 1-2 kHz) plasma fluctuations are a relatively common occurrence in this plasma source. The presence of such fluctuations will broaden the

measured IEDF since the plasma potential is superimposed on the thermal spread in RFA data. To handle this difficulty, the substrate upon which the grid-spacers are stacked has been designed as a patterned, electroplated planar triaxial line (Figure 2-10) and can be used in a driven shield configuration for high sweep-rate operation.

Two means of data acquisition have been utilized for this diagnostic. For quiescent plasmas, a computer controlled circuit, shown schematically in Figure 2-11a, applies voltage to the collector and reads floating picoammeter current through an AD-289J isolation amplifier. All D/A and A/D is handled by a Data Translation DT-2811 card. The current measured at each voltage step is an average over a number of readings (typically 25-100). When acquiring data under conditions of a fluctuating plasma, the setup shown in Figure 2-11b is utilized. The waveform applied to the collector is a 10-20 kHz triangle wave, which is generated by an HP 3312A function generator and amplified by an Apex PA-08 power op amp. The current is measured by a high-bandwidth, floating, current measuring circuit with sensitivity of approximately 10nA. The output from this circuit is acquired by the LeCroy 9414 DSO. Further details of the electronics can be found in Appendix A.

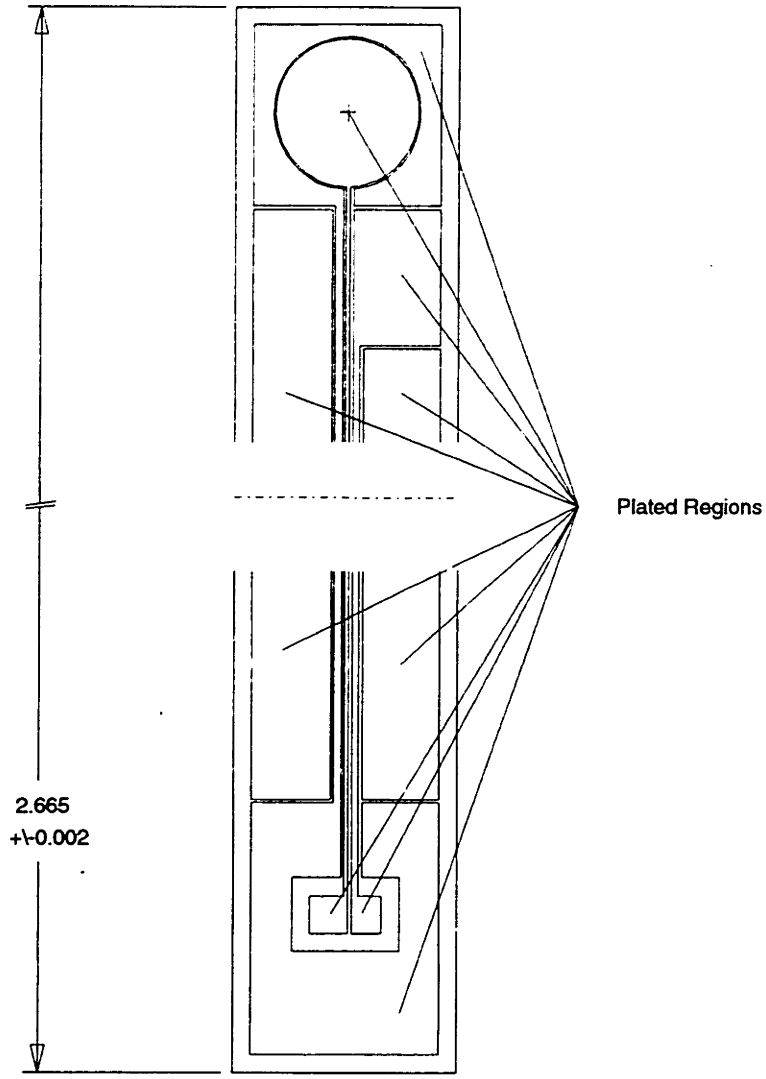

Collector II

Tolerance on all dimensions to be +/- 0.001 unless otherwise specified

Plating to be chrome/gold on 0.03" fused silica as per Quotation

File: FAST2.DV

Figure 2-10: Plated Collector for Retarding Field Ion Energy Analyzer

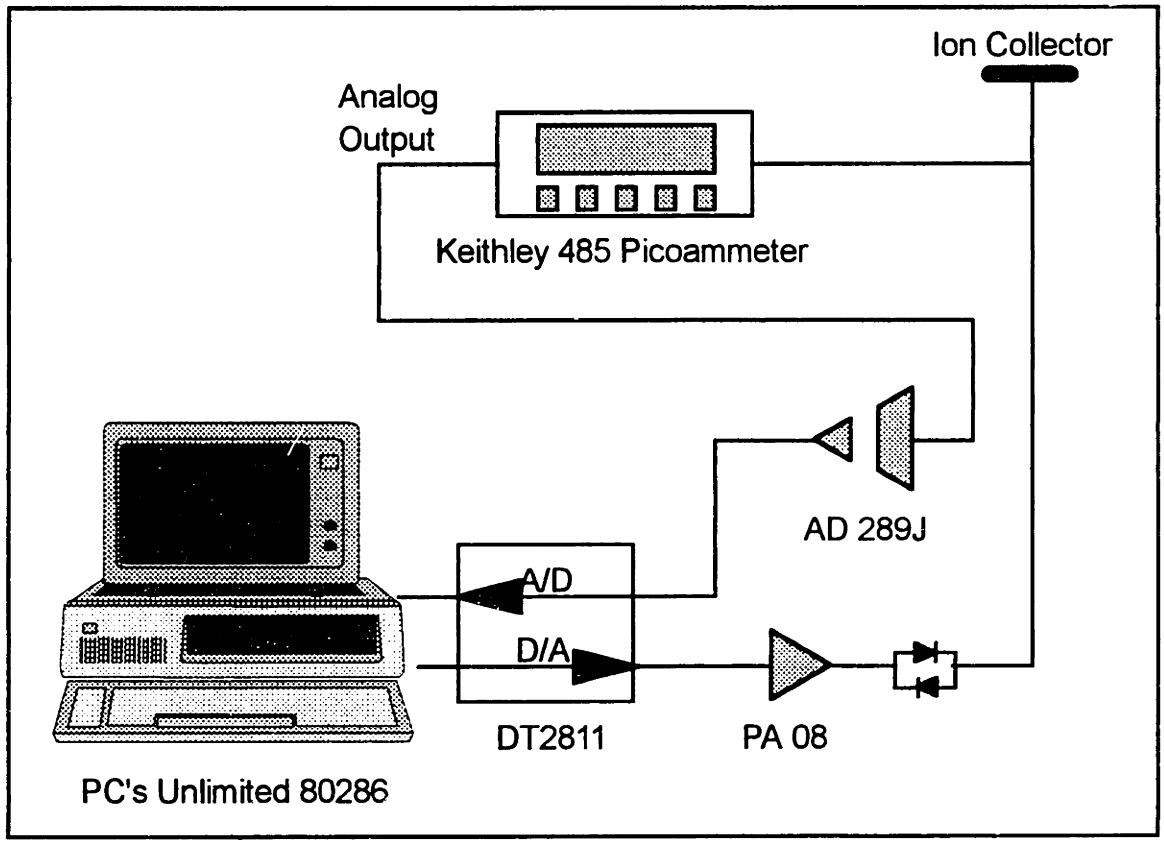

Figure 2-11a: RFA Data Acquisition for Quiescent Plasmas

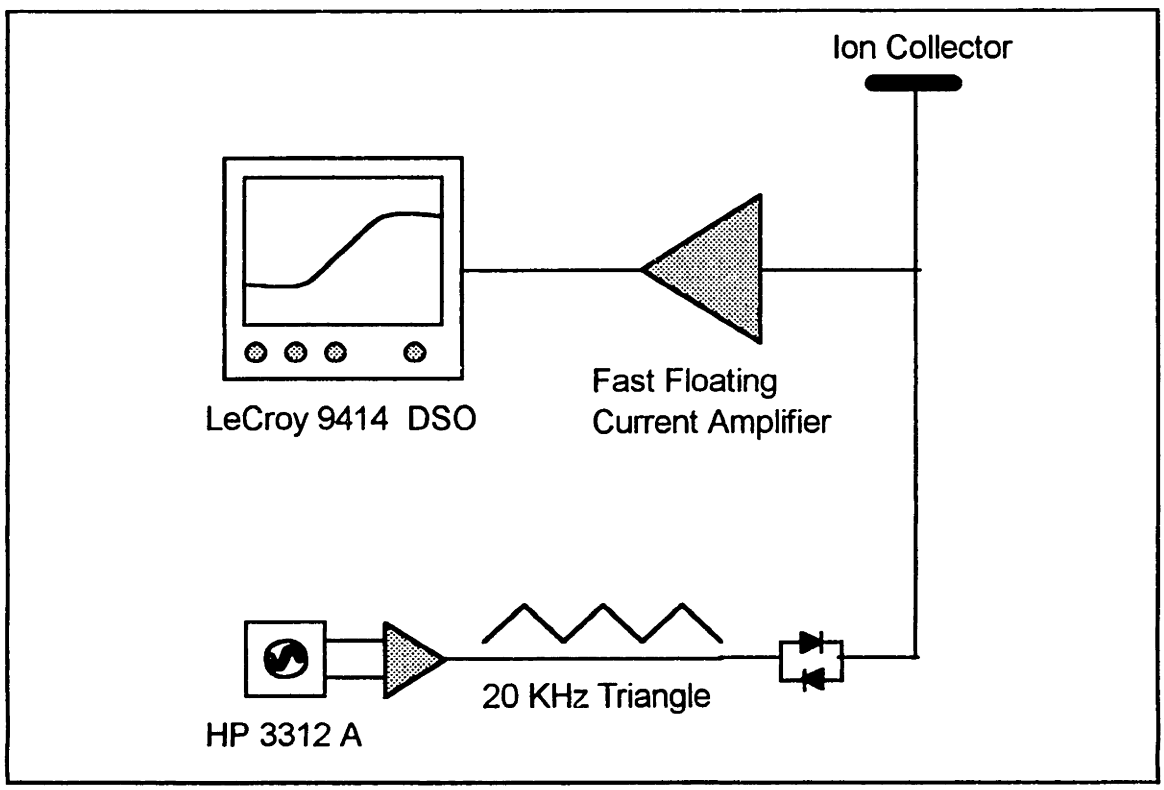

Figure 2-11b: High Speed RFA Data Acquisition

Chapter Three

Ion Transport Theory

The purpose of this chapter is to lay the theoretical groundwork through which the results of the experiments described in Chapters Four and Five may be interpreted. The chapter is broken up into four sections. The first addresses the determination of various coefficients appearing in the transport equations along with a discussion of fundamental processes upon which these quantities are based. Section Two illuminates the various mechanisms for radial ion transport which are operative in these experiments. Section Three consists of a formal derivation of the radial transport problem and of the formulae by which theory and experiment may be compared. The final section outlines the theory for a Kelvin-Helmholtz-type instability which has been observed in the course of this thesis work.

3.1 Transport Coefficients

Collisions

At the heart of any transport theory lies the detailed nature of the collisional processes by which energy and momentum are transferred amongst the various constituents of the system under consideration. It is therefore worth considering which are the dominant collisional mechanisms in these experiments.

Ions undergo collisions with neutrals, electrons and, furthermore, collide

amongst themselves. The relative magnitudes of these collision frequencies are $\nu_{ie} << \nu_{io} << \nu_{ii}$, where the expressions for the particular collision frequencies are given by [Braginskii, 1965]:

$$\nu_{ie} = 3.96 \times 10^{-11}\, n_e(\ln\Lambda)T_e^{-3/2}\ \text{sec}^{-1}$$
$$\nu_{ii} = 4.78 \times 10^{-8}\, n_i Z^2(\ln\Lambda)T_i^{-3/2}\ \text{sec}^{-1}$$
$$\nu_{io} = 1.51 \times 10^{-9}\, n_o T_i^{1/2}\ \text{sec}^{-1}$$

and $\nu_{ie} \approx (m_e/m_i)\nu_{ei}$. Here the units are Gaussian cgs except for temperatures, which are in eV. The ion mass has been taken to be that of Ar, and the cross section for ion-neutral collisions is composed of the sum of elastic and charge-exchange cross-sections measured at 1.36 eV [Vestal et al., 1978].

Ion radial diffusion depends predominantly upon collisions with neutrals. The ion-ion collisions have a negligible effect upon the cross-field transport since these collisions lead to no net displacement of the two guiding centers. Thus, since $\nu_{ii} >> \nu_{io}, \tau_{conf}^{-1}$, (where τ_{conf} is the ion confinement time defined by N/L, and N is the total number of ions in the plasma and L is the number of ions lost axially per second) the role of ion-ion collisions is simply to bring the ion velocity distribution function into near-Maxwellian form [Braginskii, 1965]. Of course, if ions in different charge-states were to exist in the plasma, then collisions between ions differing in charge state would also contribute to the cross-field transport. At these low electron temperatures, however, the fractional population of Ar^{2+} is entirely negligible. This assertion is born out experimentally by the absence of any energy-doubled component in the observed ion energy distribution functions. Since the electron energy transferred in an e-i collision is proportional to the electron-ion mass ratio, ($m_e/m_i = 1.36 \times 10^{-5}$ and $\nu_{ei} \sim 10^7\ \text{sec}^{-1}$) an electron will dissipate an energy

totaling nearly its own temperature in collisions with ions during its lifetime of several milliseconds. This energy is, however, effectively dissipated into the neutral population since ion-neutral collisions occur on a timescale nearly a factor of 10^2 shorter than an ion lifetime, and therefore cannot account for the surprisingly high ion temperatures encountered in this work.

Finally, we consider electron collisions. From Table 3.1 it can be seen that electron-ion and electron-electron collisions dominate over collisions with neutrals. The expression for the electron-ion collision frequency has been indicated above, and is typically one half of that for electron-electron collisions. Throughout this work it will be assumed that electrons have a Maxwellian distribution of energy. For this assumption to hold in an ECR source, the coulomb collision frequencies must exceed the axial bounce frequency of the (electrostatically) confined electrons. Taking the bounce time to be simply the transit time for a thermal electron over twice the machine length we have

$$\nu_{ei}\tau_{bounce} \approx 6 n_e T_e^{-2} \quad , \tag{3.1}$$

where n is in $10^{12}cm^{-3}$ and T_e is in eV. This expression is close to, and generally exceeds, unity for the conditions in this thesis. Below neutral pressures of 1 mTorr, however, electron temperatures increase dramatically, while the plasma density decreases (Figure 5-7), and multiple passes through the resonance zone become possible. Under these low pressure conditions one begins to observe anisotropy in the parallel and perpendicular components of the electron distribution function, though these components remain nearly Maxwellian in form [Bowden, et al. 1994].

Ion Transport Experiment Parameters	
Feed Gas	Argon
Midplane Magnetic Field	700 G
ECH Power	300 W
Plasma Length	40 cm
Midplane Plasma Radius	4 cm
Electron Temperature	2 eV
Ion Temperature	1 eV
Plasma Density	10^{12} cm^{-3}
Neutral Density	5×10^{13} cm^{-3}
ν_{ei}	10^{7} sec^{-1}
ν_{eo}	2×10^{5} sec^{-1}
ν_{ii}	2×10^{5} sec^{-1}
ν_{io}	8×10^{4} sec^{-1}
τ_{conf}	3 msec

Table 3.1 Typical Parameters for the Ion Transport Experiment

Ion Transport Coefficients

In the absence of fluctuating fields, the mechanisms by which ions are transported across magnetic field configurations possessing axisymmetry, as in this system, must be collisional in nature; that is, no "neoclassical" [Chen, 1984] effects are to be expected since these rely upon guiding center drift off of magnetic flux surfaces due to torsion of the magnetic field lines. As stated above, only collisions involving an ion and another species (or charge state) can lead to appreciable cross-field transport, so we will use ν_{io} for the collision frequency inserted into the diffusion and mobility coefficients.

At the upper end of the pressure range under investigation (~3 mTorr), the ion gyro-frequency and the net ion collision frequency are of similar order, while ion-ion collisions occur on a much faster time scale, and it is appropriate to treat the ions as a conducting fluid. Under these conditions the ion diffusion coefficient can be taken as [Krall and Trivelpiece, 1986]

$$D_i = \frac{\frac{eT_e}{m_i \nu_i}}{1 + \frac{\omega_{ci}^2}{\nu_i^2}} \equiv \frac{D_i^o}{1 + \frac{\omega_{ci}^2}{\nu_i^2}} . \qquad (3.2)$$

Experimentally, little change in the ion temperature is observed over the pressure range considered here, 1-3 mTorr. Thus, ω_{ci}^2/ν_{io}^2 varies from near unity at 3 mTorr to order 10 at the lower end of the pressure range. Furthermore, as the neutral pressure is decreased from 2 mTorr, the plasma undergoes a precipitous change in charged particle density, falling to about half of its previous value. Therefore, at pressures below the transition point, ion-ion collisions occur on a time-scale commensurate with that of ion gyration

and the fluid picture of transport breaks down, with radial ion transport taking on the character of a random walk of step size ρ_i. Under these conditions, one expects the diffusion coefficient to have the form

$$D_i = \rho^2 \nu_i \quad . \tag{3.3}$$

Clearly, the underlying physics of equation 3.2 differs fundamentally from that of equation 3.3. However, expression 3.2 for the diffusion coefficient goes continuously over to that of 3.3 in the appropriate limit. Thus, throughout this work, we will use the general expression, equation 3.2, for the diffusion coefficient, while always keeping in mind that we are in fact observing the transition from hydrodynamic to kinetic behavior. Figure 3-1 plots equation 3.2 as a function of ion temperature with neutral pressure as a parameter (for a neutral temperature of 500 °K and a magnetic field strength of 700 G). Because we have assumed a diffusive model for transport, the ion mobility, μ_i, can be obtained from D_i through the Einstein relation [Chen, 1984]:

$$\mu_i = \frac{D_i}{T_i} \quad . \tag{3.4}$$

The use of a limiter in these experiments creates a region of strongly sheared radial pressure and electric field gradients, and furthermore sets up axial velocity gradients ($v_z = v_z(r)$) for conditions when a cold, dense scrape-off layer forms. Thus, the effects of ion viscosity warrant consideration. The importance of ion viscosity depends upon the product of the ion-ion collision time and the various components of the tensor $\partial v_j/\partial x_k$. Ion flow velocities along field lines in the central plasma are around 10^4 cm/sec, given a machine length of 40cm and confinement time of several msec. The parallel velocity

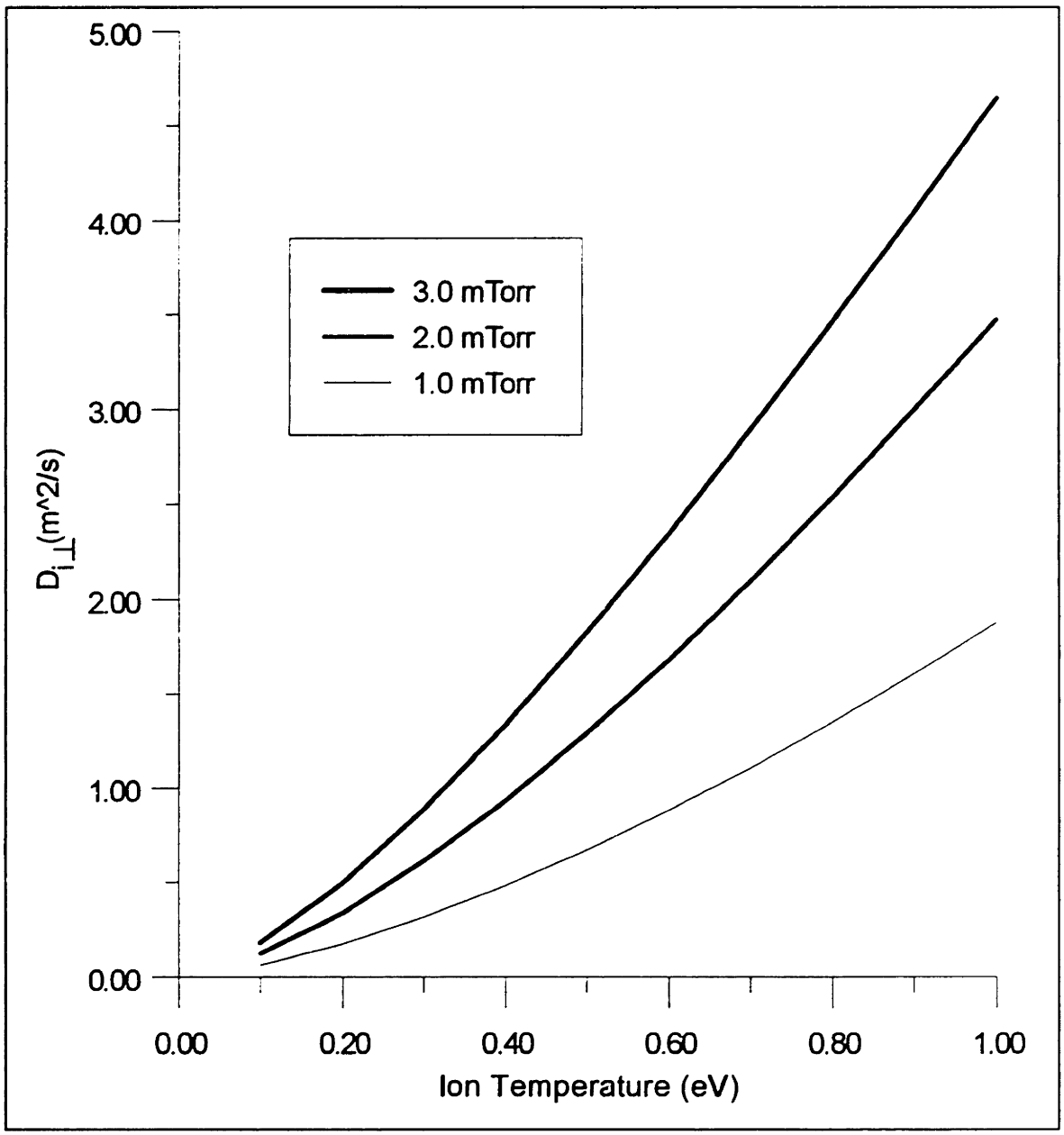

Figure 3-1: Theoretical Values for Ion Perpendicular Diffusion Coefficient for Neutral Temperature of 500 K and 700 G.

decays in the scrape off layer on a scale length of about 1 cm so that parallel viscous effects can be neglected for ion collision times below 10^{-5} sec. Both diamagnetic and **ExB** drifts can be as high as 10^5 cm/sec in the plasma edge, shearing over the typical 1cm length scale; however, potential and density gradients in this region tend to be in opposite directions, so that these two radial forces on the ions approximately balance. Consequently, perpendicular ion viscosity is also not important. In any case, none of these viscous effects contributes directly to radial ion transport and in all probability provides only lower order corrections to the structure of the sheared layers.

Electron Transport

As will be discussed more thoroughly in the next section, for the particular boundary conditions of this experiment, the radial transport of ions couples to a certain extent with that of the electrons. Therefore we take up the problem of developing expressions for cross-field electron transport. The orderings for electron transport are $\nu_{ei} << \omega_{ce}$ and $\rho_{le} << L_r$, where L_r is the length scale of any radial gradient. The ratios (ν_{ei}/ω_{ce}) and (ρ_{le}/L_r) thus provide expansion parameters for a perturbative solution of the Boltzmann equation. The procedure for accomplishing such a solution is well known [Sigmar, 1989], so only an outline will be given below.

The Boltzmann equation in a locally rectangular coordinate system with $z = b$, $r = y$ and $x = \phi$ can be written as [Braginskii, 1965]

$$\omega_\alpha \frac{\partial}{\partial \alpha} f_e = v \cdot \nabla f_e + \left(\frac{q}{m_e} E + \omega_\alpha v \times \frac{B_1}{B_o}\right) \cdot \frac{\partial}{\partial v} f_e - C(f_e) \tag{3.5}$$

$$C(f_e) = \nu_{ei} \left[\frac{1}{2\sin\theta} \frac{\partial}{\partial \theta} \sin\theta \frac{\partial}{\partial \theta} f_e + \frac{1}{\sin^2\theta} \frac{\partial^2}{\partial \alpha^2} f_e \right] \tag{3.6}$$

where α is the gyro-angle, θ is the pitch-angle and $v = v_\parallel z + v_\perp \cos\alpha\, x + v_\perp \sin\alpha\, y$, with $v_\parallel = v\cos\theta$, $v_\perp = v\sin\theta$. The Lorentz collision operator accounts for the effects of pitch-angle scattering of electrons off of ions only, but is nonetheless more accurate than the often used Krook operator [Bhatnager et al., 1954]. Taking $E_\perp$ to scale as $T_e L_r^{-1}$ and noting that for our conditions $(\nu_{ei}/\omega_{ce}) \sim (\rho_{le}/L_r) \equiv O(\delta)$, it is clear that all terms on the right hand side (RHS) of equation (3.5) are down by δ from the LHS. We proceed by writing $f(x,v)$ as

$$f(x,v) = f_o(x,v) + f_1(x,v) \quad , \tag{3.7}$$

with $f_1/f_0 \sim O(\delta)$. We can expand equation (3.5) order by order, and to first order we have

$$\frac{\partial}{\partial \alpha} f_o = 0 \tag{3.8a}$$

$$\omega_\alpha \frac{\partial}{\partial \alpha} f_1 = v \cdot \nabla f_o + \left(\frac{q}{m_e} E + \omega_\alpha v \times \frac{B_1}{B_o}\right) \cdot \frac{\partial}{\partial v} f_o - C(f_o) \; . \tag{3.8b}$$

It is clear that equation 3.8a is satisfied for arbitrary anisotropy in $v_\perp$, $v_\parallel$.

However, the temperature isotropization time for electrons is [Braginskii, 1965]

$$\tau_T = 1.2 \times 10^6 T_e^{3/2} / n(\ln\Lambda)$$

which for this plasma is a few tenths of a microsecond and significantly shorter than transport timescales. Thus, the previously ignored e-e collisions have been invoked in order to relax the zero order distribution to a Maxwellian equilibrium. The assumption of a zero-order Maxwellian *requires* that the electron bounce time exceeds τ_T. If it does not, electrons can make multiple passes through the resonance zone, receiving random "kicks" in perpendicular velocity. In the limit of many passes, a Fokker-Planck treatment of the RF induced velocity space diffusion [Mauel,1985], [Hokin,1987] must be considered. As was noted previously, this regime occurs at pressures near and below 0.5 mTorr where neutral fluxes are insufficient for efficient plasma processing.

The differential operators involved in equation (3.8b) are most easily dealt with by expanding f_1 in spherical harmonics [Sigmar, 1989]:

$$f_1 = \sum_0^\infty a_{lm} Y_l^m \quad . \tag{3.9}$$

The partial derivatives with respect to velocity can be written in terms of the spherical harmonics as well:

$$\frac{\partial}{\partial v_x} = \frac{1}{2}\left[Y_1^{-1} + Y_1^{1}\right]\frac{\partial}{\partial v}$$

$$\frac{\partial}{\partial v_y} = \frac{i}{2}\left[Y_1^{-1} - Y_1^{1}\right]\frac{\partial}{\partial v}$$

$$\frac{\partial}{\partial v_z} = Y_1^{0}\,\frac{\partial}{\partial v}$$

$$\frac{\partial}{\partial \alpha}Y_l^m = imY_l^m \quad .$$

For f_o Maxwellian, the right hand side of 3.8b therefore contains only Y_l^m's with $l \leq 1$ by virtue of the velocity operators above and the identity

$$C(Y_l^m) \equiv -\frac{l(l+1)}{2}\,Y_l^m \quad . \tag{3.10}$$

Furthermore $\partial f_1/\partial\alpha$ couples only to the m's. We therefore have

$$a_{lm} = 0\,; \qquad l > 1 \quad . \tag{3.11}$$

Since the series contains only a few terms, the a's are easily evaluated. Moments of the full distribution, $f_m + f_1$, yield the desired transport fluxes in a straightforward manner.

The major purpose of this analysis was to verify that the usual technique of finite larmor radius expansion of the Boltzmann equation applies to the electrons of this system. The algebra and intermediate results are therefore

omitted and the end result for the radial electron flux will simply be quoted [Sigmar, 1989]:

$$\Gamma_{e\perp} = -m_e n \nu_{ei} \left[\frac{\left[\frac{\nabla\Phi}{B} + \frac{\nabla(nT_e)}{neB} \right] \times b}{eB} \right] \times b \quad . \tag{3.12}$$

Thus, the radial electron fluxes are driven by $\mathbf{R}_\perp$x**B** forces, where $\mathbf{R}_\perp$ is the friction on the azimuthal drift motion generated by radial gradients in pressure and potential. Note that negative pressure and positive potential gradients lead to radially outward directed electron fluxes.

3.2 Transport Mechanisms

Boundary Conditions

Any useful discussion of transport should be prefaced by a careful definition of the boundary conditions. It is the stated intention of this thesis to understand ion transport in a configuration which possesses boundary conditions at once simple and well defined and bearing close resemblance to industrial plasma sources. In such sources, to avoid sputtering of metal contaminants, the surfaces exposed to the plasma are insulators, typically quartz or anodized aluminum. The only ground reference for these sources is the workpiece and perhaps some part of the chuck used to hold the workpiece in place. The workpiece itself, if it is a semiconductor wafer, presents an intricate pattern (on the scale of 1μm and below) of insulators and conductors which varies temporally on the timescale of seconds as etching or deposition proceeds. Since these scales are small compared to typical radial transport

lengths, the wafer provides what is, effectively, a conducting boundary. As previously noted, the experimental configuration bears close resemblance to the industrial norm (Figure 2-1).

Diffusion Mechanisms

For an open-ended, magnetized plasma in which there are no fluctuations and in which neo-classical diffusion does not occur, there exist two limiting regimes for radial ion transport: ambipolar diffusion and Simon diffusion. In which of these regimes a plasma exists, or indeed, whether it can be classified by one or the other at all, depends intimately upon the boundary conditions of the experiment. Two limiting boundary conditions make the distinction between the two mechanisms of transport most clear. In the case of a perfectly insulating boundary, the flux of electrons and ions to each point on the wall must equilibrate. (The wall will charge until they do). The plasma adjusts its charge distribution until electric fields are set up to reduce the flux of the more diffusive species, and one has the familiar case of ambipolar diffusion. The only difference between this and the usual discussion of ambipolar diffusion for a non-magnetized plasma is that ions, due to their large Larmor radii, tend to move across flux surfaces more rapidly than do the magnetized electrons, so that the radial ambipolar field points into the plasma while the axial field, as usual, points out.

For the case of a perfectly conducting boundary, the ability of charges to flow in the walls of the vacuum vessel obviates the need for "local ambipolar diffusion" [Simon, 1959]. With magnetic field strengths sufficiently strong to render perpendicular electron diffusion and mobility negligible, small changes in the local potential can, due to the high parallel electron conductivity,

enhance or deplete the flow of electrons along the magnetic field lines in such a way that these losses balance the cross-field loss of ions which diffuse at what is, essentially, their intrinsic rate. The plasma thus remains quasi-neutral, with global electron and ion losses equal, but with currents flowing in the plasma and through the chamber walls.

A variant of this mechanism has been observed in the scrape-off layer of tandem mirror machines [Hooper and Cohen, 1994]. In these experiments, a limiter was used to place a gap between the core plasma and the chamber wall. It was found that ions streamed into the scrape-off layer at a rate well above that expected for cross-field electron flow. The global fluxes were balanced via currents flowing in limiters and endwalls. The upshot of these considerations is that even for relatively simple configurations the determination of ion radial transport presents formidable difficulties.

The Transport Problem

We now proceed to define the transport problem of this thesis. The electrons in these experiments are tightly magnetized and can travel a significant fraction of the machine length before undergoing a collision (Table 3.1). This means that the proper coordinate system for describing both the transport of electrons and the ionization source function is magnetic flux coordinates. The usual system of flux coordinates (ψ,χ,θ) will thence be adopted with ψ being the magnetic flux, $\nabla\chi = \mathbf{B}$, and θ being the azimuthal angle in the axisymmetric system. The flux has been evaluated both by means of an off axis expansion [Morozov and Sol'vev, 1962]:

$$\psi(r) = 2\pi r J_1(rB_o(z)) \quad , \tag{3.13}$$

where $B_o(z)$ is the on-axis B-field and J_1 is the ordinary Bessel function of the first kind, order 1; and by means of a finite element magnetic field evaluation code (Soldesign). For the high axial-to-radial aspect ratio of this experiment, the two methods agree to within experimental positioning error. Thus, in constructing the experiment Soldesign was used, while in data analysis, where analytic expressions are helpful, use was made of the formula 3.13.

One of the basic problems in formulating a theory for transport in this system is the lack of symmetry about the midplane, both in terms of the magnetic coordinate system and the boundary conditions. The difficulties inherent in this situation can be illuminated by formally dividing the reactor into two regions, I and II, upstream and downstream respectively, of an as yet unspecified surface $S_o(\chi,\psi)$. The construction is illustrated in Figure 3-2.

For each species, j, there must exist, at a finite distance from the microwave window, a surface $\chi = S_j(\psi)$ (assuming axisymmetry) on which $\Gamma_j \cdot \mathbf{b} \equiv 0$, where Γ_j is the particle flux of species j. In a statistical sense, all particles of type j born between the window and $S_j(\psi)$ must flow to an adjacent radial or axial wall. In region I, the boundary conditions are purely insulating and, furthermore, the electrons are effectively pinned to fieldlines. Now if $S_i(\psi)$ and $S_e(\psi)$ coincide, then there can be no net radial flow into or out of the differential volume of the flux surface since flows to the window are equal, and ambipolar diffusion along the field lines obtains. The degree to which $S_i(\psi)$ and $S_e(\psi)$ are allowed to differ is set by the requirement that the axial flow of ions across S_e (which consists of ionizations between S_i and S_e) must be balanced by radial transport into or out of the flux surface within Region I. Coincidence of $S_i(\psi)$ and $S_e(\psi)$ does not, however, force ambipolar diffusion on Region II. In the analysis of the data we will assume that $S_i(\psi)$ and $S_e(\psi)$ overlap, and will determine the location of $S_o(\psi)$ in Figure 3-1 by integrating

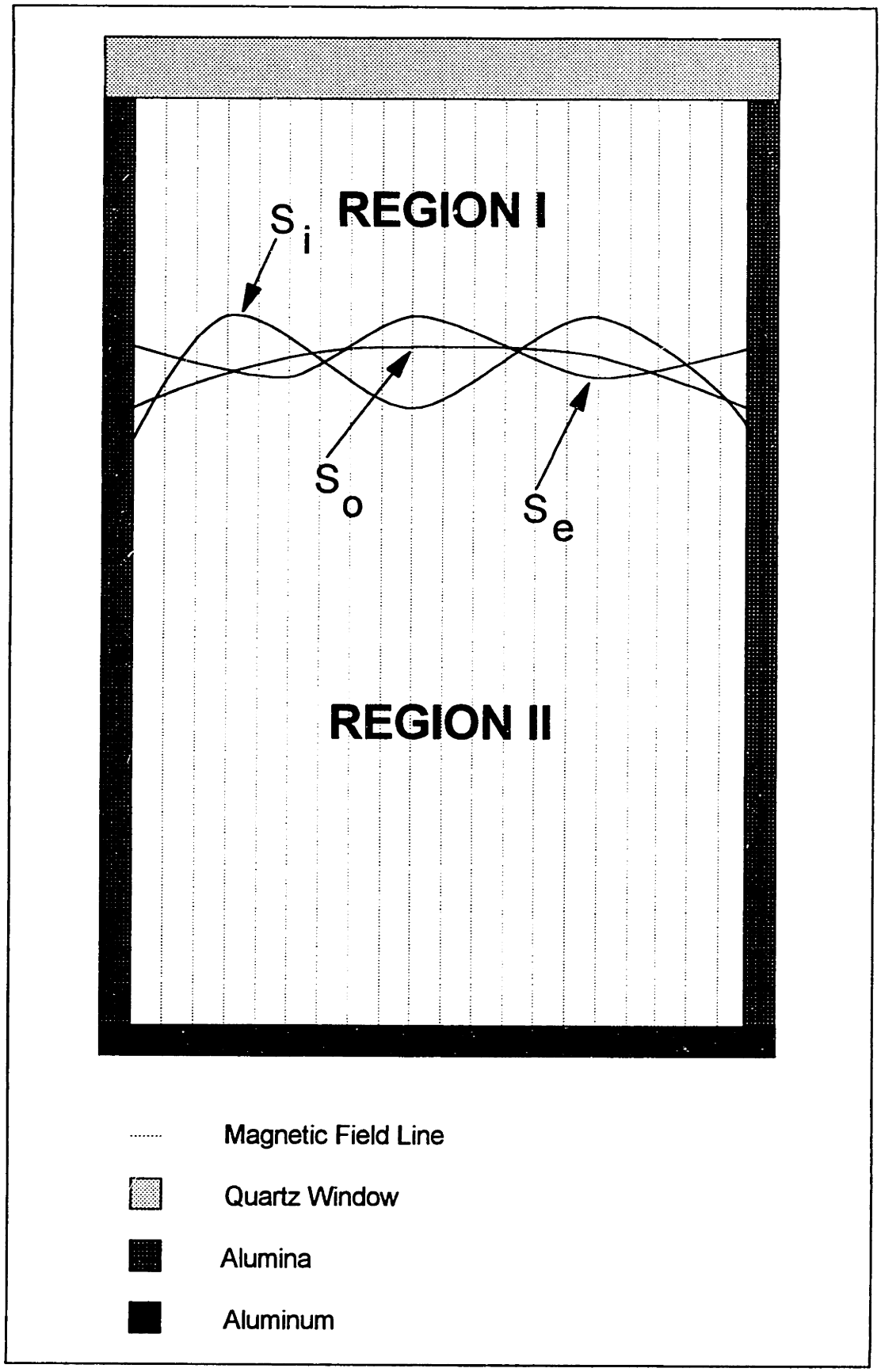

Figure 3.2: Ion Transport Schematic

the ionization, starting from the wafer, along a flux surface until it balances the electron flux to the wafer. The error in this approximation will be calculated in Chapter Four.

3.3 Transport Equations

The basic equation for steady state transport is

$$\nabla \cdot \Gamma = I(\chi,\psi) \quad , \tag{3.14}$$

where Γ is the flux, and $I(\chi,\psi)$ is the source function for the ions (ionization - recombination). Breaking equation 3.14 down into components parallel and perpendicular to **B** gives

$$\nabla_{\parallel}\Gamma_{\parallel} + \nabla_{\perp}\Gamma_{\perp} = I(\chi,\psi) \quad . \tag{3.15}$$

The first term on the LHS can be evaluated as follows:

$$\nabla_{\parallel}\Gamma_{\parallel} = \nabla \cdot \left(\frac{\boldsymbol{B}}{B}\right)\Gamma_{\parallel} = \frac{\nabla \cdot \boldsymbol{B}}{B}\Gamma_{\parallel} + \boldsymbol{B} \cdot \nabla \frac{\Gamma_{\parallel}}{B} \tag{3.16}$$

$$\nabla \cdot \boldsymbol{B} \equiv 0 \quad .$$

To simplify the ensuing math we note that the usual power-series expansion of the Bessel function:

$$J_n(x) = \frac{x^n}{2^n n!} - \frac{x^{n+2}}{2^{n+2}(n+1)} + \cdots$$

gives, for equation 3.13,

$$\psi = \pi r^2 B_o(z) \tag{3.17}$$

to an excellent approximation. The volume element for integration is

$$dV = \frac{d\psi d\chi}{B^2} = \frac{d\psi ds}{B} , \tag{3.18}$$

where ds is the differential length along the fieldline.

The approach here is to collapse the two dimensional (χ,ψ) problem into one dimension (ψ) by averaging along the magnetic field lines. The averaging procedure used here follows that of Goodman [Goodman, 1989]. Bounds for the integrals along field lines are defined by the surfaces $S_w(\psi)$ and $S_o(\psi)$ which are described by the wafer and vanishing $\Gamma_{\parallel i}$ (as described in the previous sub-section), respectively. Using (3.16) in (3.15) and integrating over s gives

$$\int_{S_w(\psi)}^{S_o(\psi)} \frac{ds}{B} \left[\boldsymbol{B} \cdot \nabla \left(\frac{\Gamma_i}{B} \right) + \nabla_\perp \Gamma_\perp \right] = \int_{S_w(\psi)}^{S_o(\psi)} \frac{ds}{B} I(s,\psi) , \tag{3.19}$$

and, upon rearrangement,

$$\int_{S_w(\psi)}^{S_o(\psi)} \frac{ds}{B} \nabla_\perp \Gamma_\perp = \int_{S_w(\psi)}^{S_o(\psi)} ds \left[\frac{I(s,\psi)}{B} - \boldsymbol{b} \cdot \nabla \left(\frac{\Gamma_i}{B} \right) \right] . \tag{3.20}$$

The last term on the RHS of (3.20) is

$$\int_{S_w(\psi)}^{S_o(\psi)} ds\ \boldsymbol{b}\cdot\nabla\left(\frac{\Gamma_I}{B}\right) = \int_{S_w(\psi)}^{S_o(\psi)} ds\ \frac{\partial}{\partial s}\left[\frac{\Gamma_I}{B}\right]$$

$$= \frac{\Gamma_I(S_w(\psi))}{B(S_w(\psi))} \tag{3.21}$$

since Γ_I vanishes identically on the upper bound. Using equation 3.21 in equation 3.20 gives

$$\int_{S_w(\psi)}^{S_o(\psi)} \frac{ds}{B}\,\nabla_\perp\Gamma_\perp = \int_{S_w(\psi)}^{S_o(\psi)} ds\ \frac{I(s,\psi)}{B} - \frac{\Gamma_I(S_w(\psi))}{B(S_w(\psi))}\ . \tag{3.22}$$

Now integrate over ψ:

$$\int_0^{\psi} d\psi' \int_{S_w(\psi')}^{S_o(\psi')} ds\ \frac{\nabla\cdot\Gamma_\perp}{B} =$$

$$\int_0^{\psi} d\psi' \left[\int_{S_w(\psi')}^{S_o(\psi')} ds\ \frac{I(s,\psi')}{B} - \frac{\Gamma_I(S_w(\psi'))}{B(S_w(\psi'))}\right]\ . \tag{3.23}$$

The RHS of equation 3.23 can be put into a form more amenable to comparison with experiment by observing that $\Gamma_I(S_w(\psi))$ represents a raw experimental quantity, while the first term, representing the source for the volume enclosed by ψ, derives from a calculation involving data from several ancillary measurements. Noting that, by equation (3.17), $B(S_w(\psi)) \equiv B_w$ is

independent of ψ, we make the following definitions:

$$\int_0^{\psi} d\psi' \int_{S_w(\psi')}^{S_o(\psi')} ds \frac{I(s,\psi')}{B} \equiv \bar{I}(\psi)$$

$$\frac{1}{B_W} \int_0^{\psi} d\psi' \, \Gamma_{\parallel}(S_w(\psi')) \equiv F(\psi) \quad .$$

Then equation (3.23) can be rewritten as

$$\int_0^{\psi} d\psi' \int_{S_w(\psi')}^{S_o(\psi')} ds \frac{\nabla \cdot \Gamma_{\perp}}{B} = \bar{I}(\psi) - F(\psi) \quad . \tag{3.24}$$

Now the ψ dependence of the bounds for the s integral on the LHS of (3.24) disallows the use of the divergence theorem in evaluating that expression. For the long-thin geometry of this experiment, distances measured from the wafer along the machine axis and those measured along field lines to the same z = constant plane differ by only a few percent even for the outer-most field lines, so that the lower bound, $S_w(\psi')$, can be taken to be independent of ψ. In the previous sub-section, we argued for taking $S_o(\psi) = S_e(\psi)$. Experimentally, $S_e(\psi)$ is found to vary by less than 10% over the radius, which justifies exchanging the order of integration in equation (3.24). We then have:

$$\int_{S_w(\psi)}^{S_o(\psi)} \int_0^{\psi} \frac{ds d\psi'}{B} \nabla \cdot \Gamma_{\perp} = \bar{I}(\psi) - F(\psi) \quad . \tag{3.25}$$

A thorough discussion of the errors involved in utilizing equation (3.25) in the interpretation of experimental results will be given in Chapter Four.

To proceed, we replace the volume integral on the LHS of (3.25) with a surface integral, and use a diffusion equation for $\Gamma_\perp$:

$$\Gamma_\perp = -D_\perp(\psi)\left(2\sqrt{\pi B\psi}\right)\left[\frac{\partial}{\partial\psi}n + \frac{n}{T_i}\frac{\partial}{\partial\psi}\phi\right] .$$

The resulting expression is

$$\int_{S_w(\psi)}^{S_o(\psi)} -ds\ \frac{2\sqrt{\pi\psi}}{\sqrt{B}}\ D_\perp(\psi)\left(2\sqrt{\pi B\psi}\right)\left[\frac{\partial}{\partial\psi}n + \frac{n}{T_i}\frac{\partial}{\partial\psi}\phi\right]$$

$$= \bar{I}(\psi) - F(\psi) , \qquad (3.26)$$

from which the equation for $D_\perp(\psi)$ is finally obtained:

$$D_\perp(\psi) = \frac{F(\psi) - I(\psi)}{4\pi\psi \int_{S_w(\psi)}^{S_o(\psi)} ds\left[\frac{\partial}{\partial\psi}n + \frac{n}{T_i}\frac{\partial}{\partial\psi}\phi\right]} . \qquad (3.27)$$

The use of a diffusion equation for the perpendicular ion flux requires some justification. The value for ion temperature and ion-neutral collision frequency found in Table 3.1 indicates that neither Larmor radius nor mean free path for thermal ions vanishes when compared with the plasma radius. Furthermore, as will be shown in Chapter Five, the radial profiles of n and ϕ possess regions of significant curvature over "diffusional" length scales. By this we mean that the perpendicular derivatives of n and ϕ change over the length of a typical step size in the assumed random walk process. A strictly local interpretation of equation 3.27 is therefore incorrect.

3.4 Kelvin-Helmholtz Instability

Several types of collective mode were observed in the course of this thesis work. It was our good fortune that they generally occurred near or beyond the boundary of the parameter regimes of interest to plasma processing. There was, however, one notable exception, which appeared at low power and neutral pressures in the 1-2 mTorr range. The mode was observed to propagate with a large amplitude in the ion diamagnetic direction and at a frequency below that of ion diamagnetic drift. The wave was well localized radially, typically appearing at the plasma edge, and always in the region of a localized depression in the plasma potential. Direct measurement of ion temperatures across the radii where the mode was excited revealed no ion temperature gradients, thereby ruling out that source of free energy for driving the instability.

It became apparent that the mode must be related to the broad class of Kelvin-Helmholtz instabilities which describe plasma collective modes in regions of strong velocity shear. The basic radial wave equation for arbitrary density and potential gradients with finite ion larmor radius terms included was derived by Rosenbluth and Simon [Rosenbluth and Simon, 1965]:

$$(T\psi')' + \left[\frac{1-m^2}{r^2}\,T + r^2\omega^2 n'\right]\psi = 0 \quad , \tag{3.28}$$

where

$$T \equiv nr^3\overline{\omega}(\overline{\omega} - \omega_{di})$$

$$\overline{\omega} \equiv \omega - \frac{m}{r} v_o(r)$$

$$\omega_{di} \equiv \frac{eT_i}{B} \frac{m}{r} \frac{n'}{n}$$

$$\psi \equiv \frac{E_\phi}{\overline{\omega}} \quad .$$

Here, E_ϕ is the azimuthal electric field and $v_o(r)$ represents a sheared ExB drift. Kent, Jen and Chen [Kent et al., 1969] employed this equation in the analysis of low frequency instabilities which they observed in the edge of Q machine plasmas. Their approach was to treat the velocity shear and density gradient as step discontinuities and to derive jump conditions connecting the solutions of equation 3.28 in each region of constant velocity. The jump conditions in turn yielded frequency and growth rate for the mode. They showed that multiple steps could be added in order to represent more faithfully the measured profiles; however, the jump condition formulae became quite cumbersome as the number of steps increased.

In this work, it has been undertaken to solve equation 3.28 for an inverted gaussian potential function localized about some non-zero radius:

$$\phi(r) = -\phi_o e^{-\frac{(r-r_o)^2}{2\sigma^2}} \quad . \qquad (3.29)$$

Taking $v_o(r)$ to be the ExB velocity of the ions we obtain

$$v_o(r) = -\frac{1}{\sigma}\left(\frac{\phi_o}{B\sigma}\right)(r-r_o)e^{\frac{(r-r_o)^2}{2\sigma^2}}$$

$$\equiv -S_o(r-r_o)e^{\frac{(r-r_o)^2}{2\sigma^2}} \quad . \tag{3.30}$$

Now T and T' can be evaluated for the Gaussian potential to yield

$$T = nr_o^3\left[\omega(\omega-\omega_{di}) + (2\omega-\omega_{di})mS_o\frac{\epsilon}{r_o}e^{\frac{\epsilon^2}{2\sigma^2}} + \left(mS_o\frac{\epsilon}{r_o}\right)^2 e^{-\frac{\epsilon^2}{\sigma^2}}\right]$$

$$T' = nr_o^3\left(\frac{mS_o}{r_o}\right)\left[1-\left(\frac{\epsilon}{\sigma}\right)^2\right]e^{\frac{\epsilon^2}{2\sigma^2}}\left[(2\omega-\omega_{di}) - 2mS_o\frac{\epsilon}{r_o}e^{\frac{\epsilon^2}{2\sigma^2}}\right]$$

$$\epsilon \equiv r - r_o \quad . \tag{3.31}$$

It is convenient to put the radial equation into dimensionless form by normalizing ϵ to σ and all frequencies to ω_{di}. To this end, the following quantities are defined:

$$z \equiv \frac{\epsilon}{\sigma}$$

$$\omega_s^* \equiv \frac{\frac{1}{r_0}\left(\frac{\phi_o}{B\sigma}\right)}{\omega_{di}}$$

$$\omega^* \equiv \frac{\omega}{\omega_{di}} \quad .$$

Then 3.28 can be written as

$$(T^*\psi')' + \left[(1-m^2)\delta^2 T^* + \omega^{*2}\delta\kappa\right]\psi = 0 \quad , \tag{3.32}$$

where the primes now denote differentiation with respect to z, and where

$$T^* \equiv \omega^*(\omega^*-1) + (2\omega^*-1)m\omega_s^* z e^{-\frac{z^2}{2}} + m^2\omega_s^{*2} z^2 e^{-z^2} \quad , \tag{3.33}$$

$$\delta \equiv \frac{\sigma}{r_o} \quad ,$$

$$\kappa \equiv \sigma\nabla_r \ln(n) \equiv \frac{\sigma}{L_n} \quad ,$$

with L_n carrying the sign of the radial density gradient. Thus far, no assumption has been made regarding the degree of localization or relative strength of potential and density gradients (parameterized by δ and κ, respectively) of the potential well. In order to gain some insight into equation 3.32, we consider its form near z = 0 by keeping leading terms in T^* and $T^{*'}$. As $z \to 0$ these become

$$T^* \to \omega^*(\omega^*-1) \quad ,$$

$$T^{*'} \to m\omega_s^*(2\omega^*-1)z \quad ,$$

and the radial wave equation (3.32) is written in the form

$$\omega^*(\omega^*-1)\psi'' + m\omega_s^*(2\omega^*-1)z\psi' + \left[(1-m^2)\delta^2\omega^*(\omega^*-1) + \omega^{*2}\delta\kappa\right]\psi = 0. \tag{3.34}$$

This equation can be put in the form of Hermite's differential equation by the substitution

$$z \rightarrow x \sqrt{\frac{2\omega^*(1-\omega^*)}{m\omega_s^*(2\omega^*-1)}} ,$$

which gives

$$\Psi'' - 2x\Psi' + 2 \frac{[(1-m^2)\delta^2\omega^*(\omega^*-1) + \omega^{*2}\delta\kappa]}{m\omega_s^*(1-2\omega^*)} \Psi = 0 . \qquad (3.35)$$

The eigenvalue condition on this equation is that the factor multiplying ψ be equal to 2n, where n is an integer. It would not be expected that the eigenvalue condition would yield accurate predictions for frequency and growth rate of these modes, since this treatment effectively ignores regions where the potential gradient becomes large. On the other hand, we now know something of the character of the solutions of equation 3.32, at least in the region of the potential trough minimum.

In order to determine the frequencies and growth rates of this mode, it is necessary to solve equation 3.32 as an eigenvalue problem. If a reasonable trial function for ψ can be guessed, then the approximate eigenvalues for this Sturm-Liouville problem can be determined via the Rayleigh-Ritz variational method. We would expect the disturbance, ψ, to be localized about the potential trough. Furthermore, the solution must behave as the Hermite polynomials in the region about the trough minimum, as shown above. It is therefore quite natural to select the weighted Hermite polynomials as trial

functions:

$$\psi_n = H_n(z)e^{-\frac{z^2}{2}} \quad .$$

Here $H_n(z)$ are the Hermite polynomials:

$$H_0(z) = 1$$

$$H_1(z) = 2z$$

$$H_2(z) = 4x^2-2$$

$$\vdots$$

The Rayleigh-Ritz formula for the eigenvalues [Arfken, 1985] is written

$$\omega^{*2}\delta\kappa = \frac{\int_{-\infty}^{\infty} dz \left[T^*\psi'^2 - (1-m^2)\delta^2 T^*\psi^2\right]}{\int_{-\infty}^{\infty} dz\ \psi^2} \qquad (3.36)$$

whereby the ordering $\delta \ll 1$ is implicit in the infinite bounds. Specializing to m=1, n=0 the above integrals over products of Gaussians and polynomials are easily performed to give the eigenvalue equation

$$\delta\kappa\omega^{*2} = \omega^*(\omega^*-1) + \frac{1}{2}\omega_s^* \qquad (3.37)$$

which is quadratic in ω^* and possesses the roots

$$\omega^* = \frac{1}{2(1-\delta\kappa)}\left[1 \pm \sqrt{1 - 2\,\omega_s^{*2}(1-\delta\kappa)}\right] \tag{3.38}$$

and instability for

$$\omega_s^{*2} > \frac{1}{2(1-\delta\kappa)} \quad . \tag{3.39}$$

The coupling between the ExB and diamagnetic drift modes is through the term κ, which vanishes for small radial extent of the potential trough and for large density gradient length. In either case, assuming non-vanishing ω_s^* for the former, the mode goes over into the usual ExB instability frequency regime. For $\omega_s^* \to 0$, ion diamagnetic flute modes obtain. The equations 3.38 and 3.39 give good agreement with the observed low frequency modes, as will be shown in Chapter Five.

Chapter Four

Experimental Method

The present chapter provides a thorough description of the experiments which have been conducted in the course of this thesis work. At a more pedagogical level, it serves to link our theoretical development of the transport problem with the various quantities which can actually be measured. To this end, Chapter Four consists of two subsections: General Experimental Considerations and Quantitative Transport Measurements. The first simply describes the overall ion transport experiment. The second explains how the raw data from the diagnostics can be used to determine the constituents of expression for $D_{\perp}(\psi)$, equation 3.27.

4.1 General Experimental Considerations

The experimental setup, including diagnostic access, is illustrated in Figures 4-1a and 4-1b. The vacuum vessel has at the nominal mid-plane (i.e. midway between the magnets) four access ports, 90 degrees apart, which are fitted with 2-3/4" conflat flanges. The anodized aluminum liner has 0.5" diameter holes which align with the four ports. Of these ports, one is dedicated to the capacitance manometer, and an adjacent one to an optical access window and electrical feedthroughs. The remaining two are used for probe access. The end of the system opposite the microwave window is fitted with an 8" conflat flange which has one compression-seal feedthrough at its center and four others at a radius commensurate with that of the anodized

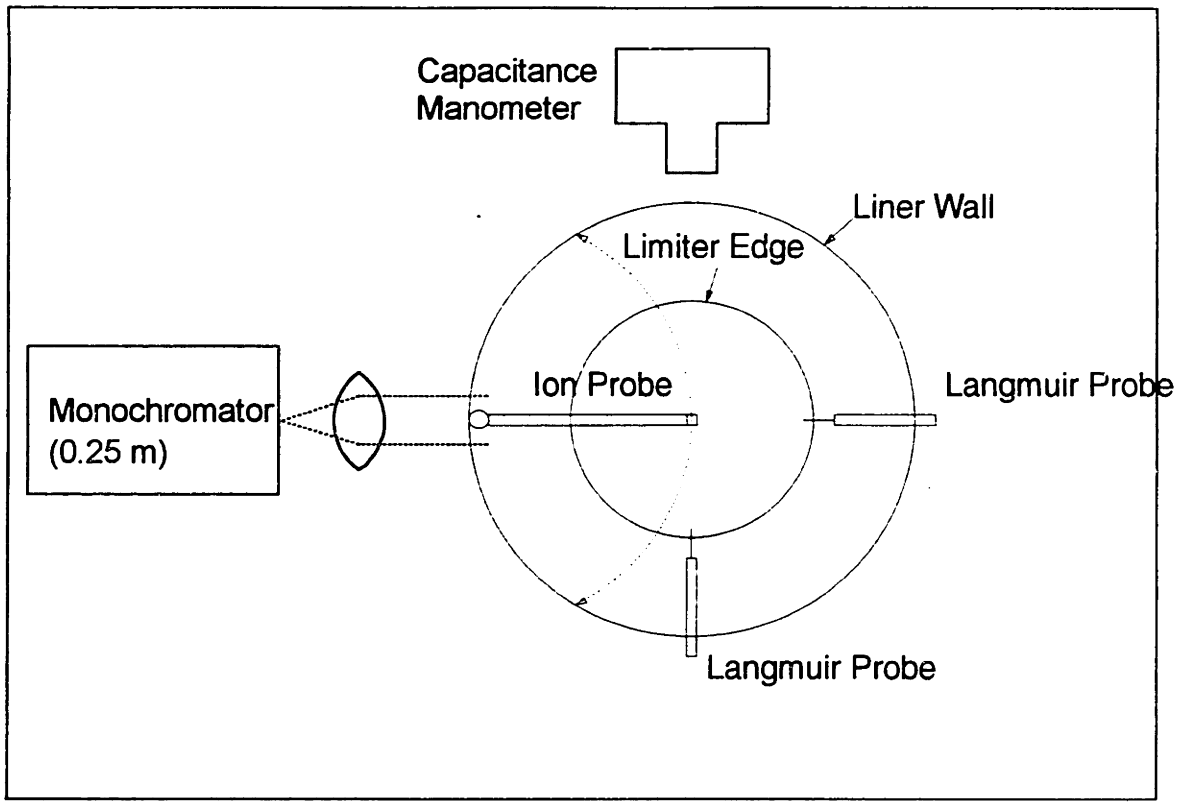

Figure 4-1a: Diagnostic Access (view along axis)

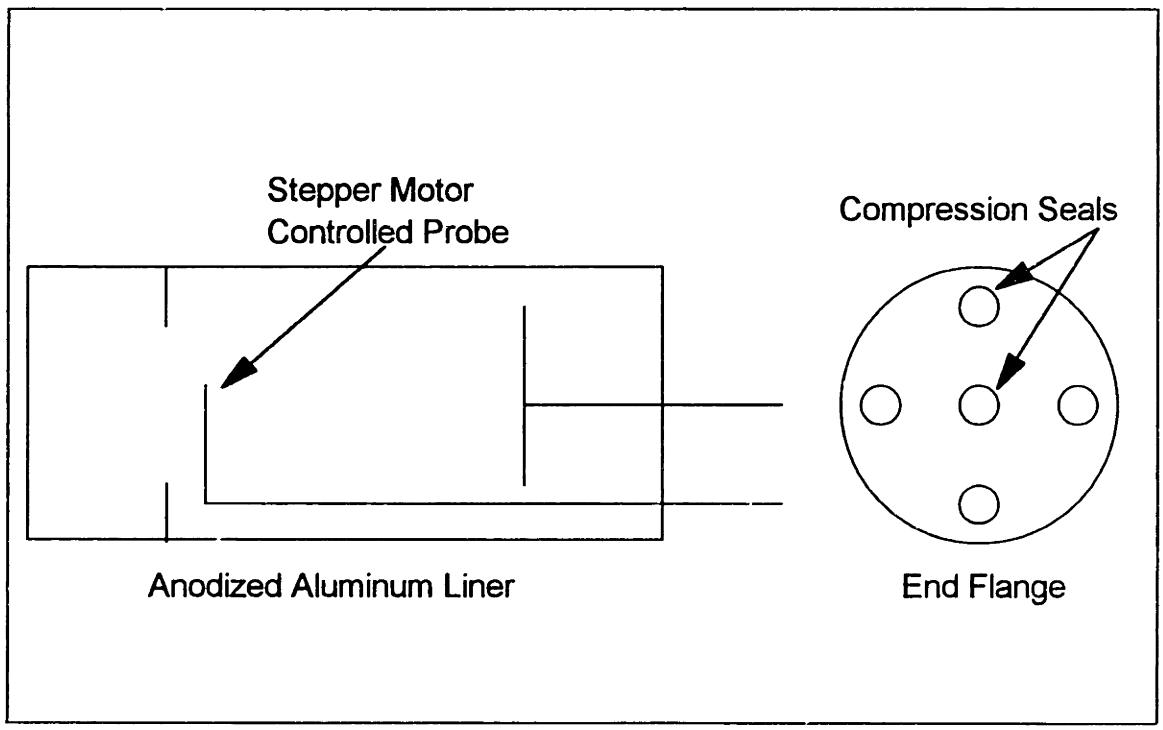

Figure 4-1b: Diagnostic Access (view from side)

aluminum liner, and spaced by 90°. The center feedthrough seals a 304 Stainless Steel rod which is used to move the wafer assembly. Two of the off-axis feedthroughs are permanently occupied, the first by a rod used to move the limiter in a fashion analogous to that of the wafer assembly. The second is addressed by a computer controlled stepper-motor system which allows a probe on a "dog-leg" (Figure 4-1) to be moved axially and radially in a precise, repeatable manner. The Langmuir probes (single and double) as well as the RFA can be operated from axial or radial diagnostic ports.

The diagnostics can be positioned with an accuracy well below transport scale lengths. Radial scans at the mid-plane were performed at a spacing of 0.25 cm with ~ +/- 1 mm positioning accuracy. The 2.6 inch dogleg was driven by a 1.8 degree stepper motor giving a minimum resolution of 0.2 cm (which occurs on axis). The axial resolution of the stepper motor system was 0.001". The relative positioning accuracy between the two radial scanning methods was ~0.2 cm. The axial scans from ports other than the one addressed by the stepper motors were done on a 1 cm grid, by hand, with +/- 0.1 cm positioning accuracy. Although the experimental configuration was designed so as to be easily altered and, in fact, frequently was, the simple, robust positioning system allowed any configuration to be re-created to within experimental error.

Ultimately, the control of neutral density proved to be the single most important factor in the reproducibility of results. Radial profiles, in particular, are extremely sensitive to this quantity, and if the neutral density drifts as it does when, for instance, chamber walls change temperature, the measured quantities undergo discontinuous (on the transport timescale) jumps, from one metastable state to another, with typical transition times of 1 msec. To remedy this problem, a capacitance manometer was installed at the midplane

and a thermocouple was placed on the anodized aluminum liner as shown in Figure 4-1. Every time an experiment was run or experimental parameters were changed, the system was allowed to stabilize thermally. The combination of mass flow control of the feed gas and careful monitoring of the neutral *density* produced both extremely quiescent plasmas (in the absence of instability) and highly reproducible data.

The overall experimental plan was comprised of two stages: 1) a preliminary mapping of parameter space and 2) a set of detailed transport measurements at select points in parameter space. The preliminary mapping was intended to serve two purposes. The first consisted in identifying what were, hopefully, contiguous regions of the parameter space in which the plasma was quiescent, and thus, where scalings could be checked. The second centered on elucidating any anomalies characteristic of the ECR species as a whole, as well as those indigenous to specific configurations. The parameter space covered is shown in Table 4-1. In this preliminary phase of the experiments, gross plasma behavior was noted and general scalings of plasma parameters with the external variables were determined. Regions of large plasma fluctuations were mapped and probable sources of instability were determined.

There are, effectively, three external variables for this system, these being the microwave power, the neutral density and the magnet current ratio. One also has the choice of process gas. Ideally, one would employ the reactive gases actually used in plasma processing (e.g. Halogens and CFC's). However, there does not exist the wealth of atomic physics data for theses species that one finds for the noble gases such as Ar. Of more practical concern, the presence of adsorbed halogens on delicate diagnostic surfaces (such as the grids or electroplating of the RFA) causes rapid corrosion when these surfaces also adsorb water vapor, which inevitably enters the system upon venting. CFC's,

Parameter Space for Ion Transport Experiments	
Power	300 - 1000 W
Neutral Pressure	0.5 - 3.0 mTorr
Magnetic Field	Symmetric Mirror (M=1.5:1)
	"Magnetic Beach"

Table 4.1 External Variables for Ion Transport Experiments

on the other hand, tend to deposit polymeric films, which can corrupt probe measurements. Therefore, Ar gas has been used throughout these experiments since its atomic physics is well represented in the literature, and because its mass (40) lies close to that of Cl^+ (35), a popular process gas. The ranges for power and neutral density typical of industrial processes are those of Table 4.1. At the time this work was undertaken, there were two competing magnetic field topologies (Figure 4-2), one monotonically decaying (magnetic beach) with fieldlines impinging near-normal to the wafer surface and the second a mirror configuration of varying current ratio. Data was taken for a symmetric mirror configuration (mirror ratio ~ 1.5) and for the magnetic beach.

4.2 Quantitative Transport Measurements

The quantitative measurement of transport coefficients, which comprises the second stage of the experimental plan, presents the researcher with many severe difficulties. Perhaps the greatest of these is the measurement of the very quantity with which one is concerned: the motion of ions. Although ion flows have been measured directly in plasmas similar to those of this experiment with Doppler-shifted laser induced fluorescence techniques (LIF) [Sadeghi, 1991], the measurements were taken at only a few spatial points so that little could be said regarding transport coefficients. Also problematic is that LIF is performed on a single (usually metastable) ion state which may have considerably different collision cross-sections than the ground-state ions presumed to make up the bulk of the distribution. Any attempt to measure well sub-sonic flows in the bulk plasma by invasive means usually introduces unconscionable errors as well. It is precisely this difficulty of measuring flows within the plasma which motivated the theoretical development of Chapter

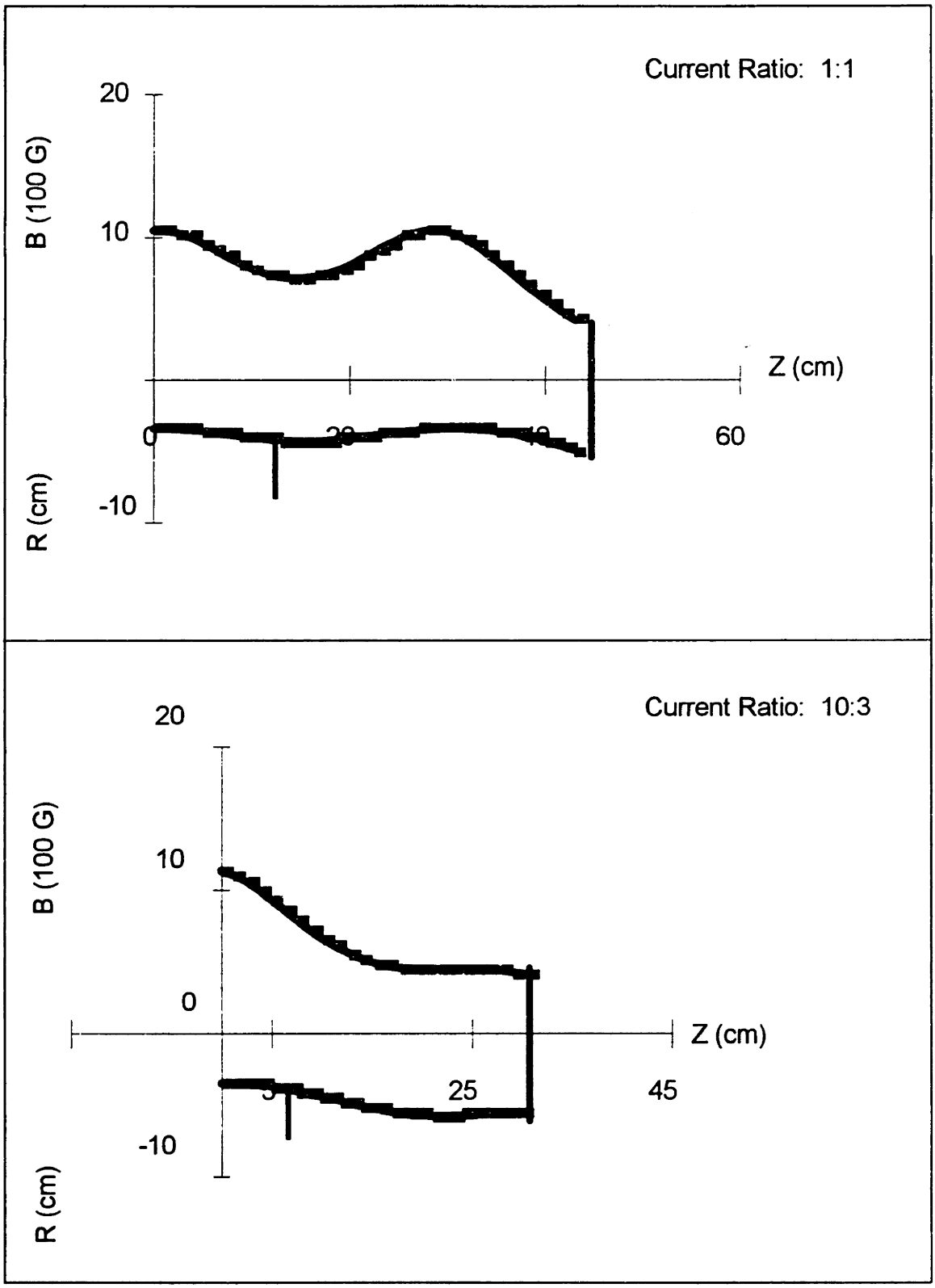

Figure 4-2: Magnetic Field Topologies
Top cuve is B on axis
Bottom curve is magnetic fiieldline touching limiter

Three, whereby only the fluxes through the plasma boundaries need be measured.

In order to quantify radial transport we must, then, measure each of the quantities which appear on the right hand side of equation 3.27 for $D_\perp$. Specifically, the ion flux to the wafer and the line averages of plasma density, plasma potential, ion temperature, and ionization rate must be determined. Below we will discuss how each of these quantities is experimentally determined, and the expected experimental error.

Plasma Density and Electron Temperature

The current versus voltage (I-V) trace of the floating double Langmuir probe (FDP) provides electron temperature and plasma density. Interpretation of the I-V trace is simplest for the case of a Maxwellian electron population, zero ion flow velocity and a sheath which is thin compared to the probe tip diameter. In this case, the current collection area of the probe is independent of voltage, and the electron current is merely the Boltzmann weighted flux to the probe:

$$I = \frac{1}{4} e A n_e v_{the} e^{\frac{(V-\Phi)}{T_e}} \qquad (4.1)$$

where v_{the} is the electron thermal velocity, $(eT_e/m_e)^{1/2}$, V is the probe tip voltage, A is the effective probe tip area in the magnetic field and ϕ is the plasma potential. Since the two tips are electrically connected, the currents to them must be equal and opposite and are assumed to be the difference between ion saturation and Boltzmann electron currents. These assumptions lead directly to the expression for the I-V characteristic equation 2.1. We now

justify fitting equation 2.1 to the experimental data by checking the accuracy of the above assumptions for our experimental conditions. The thin-sheath criterion is well satisfied for these conditions, the Debye length being always a few tens of μm while the probe tip diameter is 500μm. The approximation of no ion flow will not necessarily hold in regions of the plasma where strong density, temperature or potential gradients exist. To check the extent to which these flows affected the results, the probe was inserted radially into the region just outside of the flux surface which mapped back to the limiter inside edge where the strongest radial gradients exist. The probe was rotated through 360° with I-V traces taken every 45° in order to observe any "shadowing" effects which might occur. No differences between these traces were observed, although the relative floating potentials of the two tips with no differential voltage applied did depend upon the probe orientation ($\delta V_f/V_f \sim 0.1$).

The subtlest question is that of the electron distribution function. As mentioned in Chapter Three, if the electron collision time is small compared to the electron bounce time an isotropic Maxwellian is expected. This question were addressed by Bowden and co-workers [Bowden et al. a, 1994], [Bowden et al. b, 1994] in a series of Thompson scattering experiments on a similar ECR source in Argon. They found that for pressures of 1 mTorr and above the electron distribution function was completely isotropic, and furthermore showed no evidence of a hot tail. In our own experiments, for pressures of 1.0 mTorr and above, everywhere except very close to the liner wall, the equation 2.1 provides an excellent fit to the experimental I-V characteristic. Thus, the assumption of an isotropic Maxwellian electron distribution function appears to be well justified for these experiments.

In analyzing the FDP results, the magnitude of the assumed hyperbolic tangent fit was first set to correspond with the saturation currents. Then T_e

was adjusted until the slopes of data and fit matched at the origin. It was found that under most conditions, optimization of the fit depended on variations in T_e of less than 0.1 eV. In light of the expected and observed accuracy of the functional form for the fit, we claim a 0.1 eV accuracy for the determination of electron temperature, which gives 6% error for 1.5 eV electrons (the coldest bulk value measured).

The error involved in measuring the density is composed of two parts. The first is the error involved in evaluation of electron temperature which is necessary for the calculation of the saturation current. Since T_e enters into the expression for I_s under a radical, the error there is expected to be quite small. The second is knowledge of the actual probe collection area. For such thin sheaths, we are limited mainly by the mechanics of measuring and constructing the tips. The mechanical collection area of the probe can be measured to an accuracy of better than 5%.

Neutral Density

Since the ionization rate and the theoretical transport coefficients are proportional to neutral density, some care should be taken in the determination of this quantity. As noted in the previous section, a capacitance manometer is used to determine the neutral pressure in the source, and a thermocouple on the liner wall gives the approximate gas temperature in that region. Experimentally, it has been found that ion temperatures in the core plasma are approximately 1eV and fall off sharply in the scrape-off layer. It is therefore possible that ion heating of the neutrals can lead to non-uniform neutral density across the machine radius. Electron heating has been ignored since the electron-neutral cross-section is nearly two orders of magnitude below

that of the ions and since, for equal temperatures, the momentum transfer is down by the square root of the masses.

The heat transfer equation for this problem is

$$-\kappa\frac{1}{r}\frac{\partial}{\partial r}r\frac{\partial}{\partial r}T_o = \frac{kT_i}{4}\sigma_{io}v_{tha}n_o n_i = \frac{T_i}{4}\sigma_{io}v_{tha}n_i\frac{P}{T_o} \qquad (4.2)$$

where the temperatures are in degrees Kelvin and an ideal gas law has been assumed. The thermal conductivity, κ, is evaluated from the kinetic theory of dilute gases using experimental viscosity data [Hirschfelder, Curtiss and Bird, 1954]. To solve the problem, the ion temperature was taken to be a constant average value in the core plasma and zero in the scrape-off layer. The non-linear, inhomogeneous PDE for the core plasma was solved by commercially available software using Runge-Kutta and Shooting techniques, and was matched to the analytical homogeneous solution in the scrape-off layer. The liner temperature was taken as a boundary condition. The results of these calculations will be presented in Chapter Five.

Ionization Rate

Once the electron distribution function and neutral density are known, the ionization rate is easily determined by performing the integration

$$I = \int_0^\infty dv\ vf(v)\sigma_i(v) \quad , \qquad (4.3)$$

where $\sigma_i(v)$ is the ionization cross-section and I has units of volume$\circ$time^{-1} and must be multiplied by electron and neutral densities to get the ionization rate per unit volume. Because the electron temperatures for neutral pressures in the

mTorr range are always small compared to the 15.75 eV ionization threshold energy for Ar and no hot tail is observed, the usual technique of representing the ionization cross section by its slope at threshold has been applied to all ionization rate calculations [Delcroix, 1987]. In this case the ionization cross section becomes

$$\sigma_i(v) = 1.3 \times 10^{-17} (\epsilon - 15.75) \quad cm^2 \cdot eV^{-1} \qquad \epsilon \geq 15.75 \tag{4.4}$$

where ϵ is electron kinetic energy. The resultant expression for I is

$$I = 4.3^{-10} T_e^{\frac{3}{2}} \left[1 + \frac{15.75}{2T_e}\right] e^{\frac{-15.75}{T_e}} \quad cm^3 \cdot s^{-1} , \tag{4.5}$$

with temperatures given in eV's. The possibility of enhanced ionization through metastable channels has also been considered. The equilibrium metastable population was calculated to be $\sim 2 \times 10^{-5}$ that of the ground-state neutrals. This resulted in an enhanced ionization rate of only about 0.1%. Therefore, metastables have been ignored.

The accuracy of the calculated ionization rate depends upon knowledge of neutral and electron densities and electron temperature. Of these dependencies, the electron temperature is obviously the most critical since it appears in the argument of an exponential. Using the estimated fit accuracy of 0.1 eV we find that the error in absolute ionization rate for 2 eV electrons is less than 30%. This choice of T_e corresponds to that found on flux surfaces where the large proportion of ionization occurs.

Recombination

The bulk recombination path usually observed for Argon is dissociative recombination, $Ar_2^+ + e \rightarrow Ar^* + Ar$, which has a rate of $\sim 10^{-6}$ $cm^3 s^{-1}$ [Biondi, 1963]. However, at pressures of 1 mTorr, the production of Ar_2^+ via the three body process $Ar^+ + 2Ar \rightarrow Ar_2^+ + Ar$ should be well below the measured axial ion loss rate [Biondi, 1963] so that this mechanism has little bearing upon the calculated source function.

In the scrape-off layer, the electron temperature drops sharply with increasing radius. For electron temperatures of a fraction of an eV and densities near 10^{12} cm^{-3}, recombination via the three-body process $e + e + Ar^+ \rightarrow e + Ar^*$ becomes a viable mechanism due to the $T_e^{-9/2}$ dependence of the rate. The theoretical expression for this process is

$$R = 2.3\times10^{-8} T_e^{-\frac{9}{2}} n_i n_e^2$$

where the electron temperature is in Kelvin, and the densities are in cm^{-3} [Makin and Keck, 1963]. Recombination via this channel is calculated and added to the source function when the radial ion transport is evaluated.

Ion Energy Distributions and Fluxes

The RFA provides the spread of ion energies and the full-width-at-half-maximum (FWHM) of the energy distribution has been used wherever an ion temperature is required. All of the energy distributions measured in these experiments under quiescent plasma conditions were well characterized by a Gaussian shape. The axial flux of ions was measured by placing the RFA a few

millimeters in front of the wafer and scanning radially. Since the face-plate of the RFA is held at the same potential as the wafer and since it was well within an ion collisional mean free path of the wafer surface, the flux to the probe should be precisely the same as the flux to the wafer.

Under conditions when the plasma was perturbed by low frequency fluctuations on the order of kHz, the fast probe electronics could be used to capture a "snapshot" of the distribution function. The existence of a bimodal energy distribution function (Figure 4-3) was noticed early on in these experiments. Its appearance was eventually correlated with the presence of large amplitude plasma fluctuations in the ion-cyclotron or ion acoustic frequency range, and simply represented the time average of a monomodal distribution function shifted by plasma potential fluctuations. Thus, provided that the fluctuations were of sufficiently large amplitude to cause the shifted peaks to exceed the Rayleigh limit for resolution of two Gaussian peaks, ion temperatures could be determined under conditions of high frequency fluctuations.

The energy resolution of the RFA was discussed in Chapter Two. The accuracy of the absolute flux measurements depends upon knowledge of the orifice area, the grid transmission, and the angle of ion impingment with respect to orifice normal. The orifices were formed with a precision micro-drill (Najet 7M) which is specified to 0.001" on the diameter, giving 5% accuracy in area. The quoted grid transmission from Buckbee-Mears, the supplier, is 0.36% and since the inter-grid spacing exceeds the grid hole dimension by a factor of approximately 40, grid alignment is not an issue and transmission of successive grids is multiplicative.

The thermal spread of the ions is 1 eV or less for all plasma conditions, and the plasma potential has a typical value of less than 7 V. Since the ions

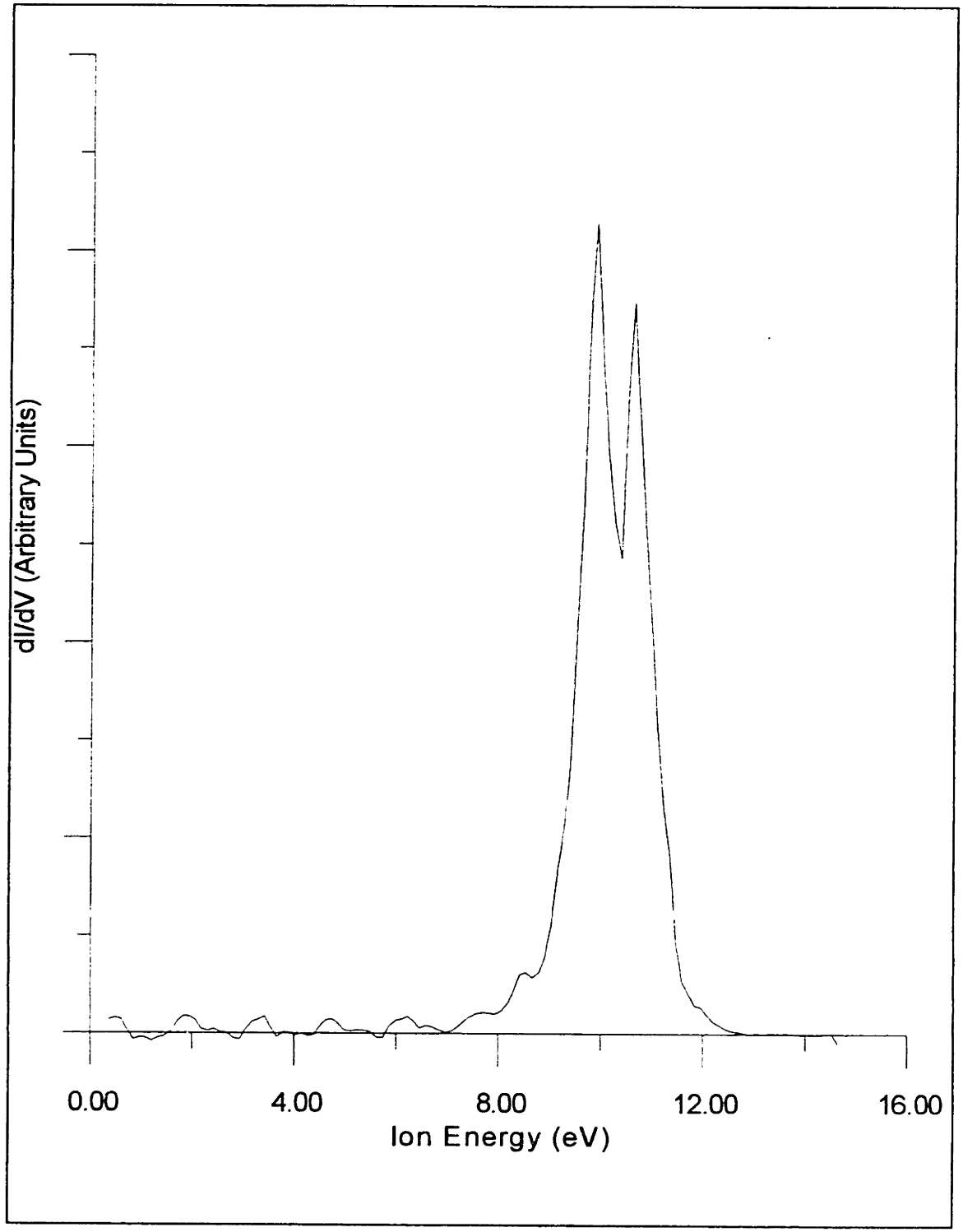

Figure 4-3: Bimodal Ion Energy Distribution Function

are only weakly magnetized and maintain sub-sonic rotational flow, the majority of off-normal ion impingement is expected to come from thermal spread of the ions. Since the orifice diameter is almost two orders of magnitude greater than the typical sheath dimension, boundary effects for the collection area should be minimal. Each hole in the mesh which backs the orifice is itself an orifice in miniature. To account for the attenuation of the off-normal flux, we assume that the attenuation varies as the cosine of the off-normal angle. Then we have for a thermal ion:

$$T_{ON} = \cos\left(\arctan\left(\sqrt{\frac{T_i}{\Phi_p}}\right)\right) \approx 94\%$$

where T_{ON} is the effective transmission for thermal ions. T_{ON} can be absorbed into the analysis, and does not represent a source of error. Thus, uncertainty in the orifice area represents the only source of error giving an instrumental error of 5% in the determination of absolute ion fluxes.

Plasma Potential

The plasma potential can be determined from the relationship

$$V_p = V_f + \frac{T_e}{2}\left[\ln\left(2\pi\frac{m_e}{m_i}\right) - 1\right] \qquad (4.6)$$

where V_f is the plasma floating potential [Hutchenson, 1987]. The floating potential can be obtained from the FDP by reading off the probe potential at the current zero crossing. The RFA provides a convenient calibration of the plasma potential measurements made by the FDP. While the FDP does a good job of determining the relative spatial variation of plasma potential, the

absolute value of these potentials can be of a dubious nature. On the other hand, the streaming, or mean, ion energy given by the RFA when placed close to the wafer is always large compared to the energy spread in these experiments and therefore gives an accurate absolute value of the flux averaged peak plasma potential. (Frequent ion collisions tend to smooth out the radial potential variations.) The absolute difference between the two methods for measuring plasma potential is typically near 15%, but the relative error for spatially resolved measurements with the FDP should be considerably less.

Determination of Line Integrated Quantities

The plasma in these experiments has a high length-to-radius aspect ratio and extremely high parallel electron conductivity, and small (in comparison with plasma radius) perpendicular transport lengths for electron quantities. Furthermore, the axial variation of measured quantities has been found to be quite smooth. It has therefore been assumed that the actual plasma, *excluding ion transport*, is well approximated by the procedure of flux mapping the radial profiles taken at the mid-plane and scaling each of these by its corresponding axial profile taken along the machine axis from the limiter to the wafer. This construction is used to represent electron temperature and density, plasma potential, and to calculate the spatial distribution of ionization and indicated line integrals. The construction of magnetic flux surfaces, the flux mapping, and the line integrals are performed by the computer code PROF which was written by the author.

Limits of Integration

Because radial electron transport is minimal, in Chapter 3, the upper bound of the line integrals, $S_o(\psi)$, was defined by integrating the ionization rate along the flux surface, beginning from the wafer, until the integrated ionization rate equals the electron flux. That is

$$\Gamma_{i\perp}(\psi) = \int_{S_w(\psi)}^{S_o(\psi)} dl\ I(\psi,l) \quad . \tag{4.7}$$

The error involved in taking this value for $S_o(\psi)$ will be evaluated presently. In practice, the electron flux is difficult to measure. A net current probe was constructed of a 0.125" square of 0.001" thick gold foil and held at ground potential immediately in front of the wafer. It gave, however, neither consistent nor believable results.

The flux of electrons should, however, be the thermal electron flux into the pre-sheath of the wafer weighted by the Boltzmann factor for the difference between plasma potential in the vicinity (within say one ion collisional mean free path) of the wafer and wafer potential. Since we know n_e, T_e and ϕ_p as functions of ψ and l, the electron flux to the wafer can be calculated and normalized to balance the total axial ion flux.

The error in taking $S_o(\psi) = S_e(\psi)$ when calculating equation (3.27) for $D_\perp(\psi)$ consists of two parts, each of which has been previously discussed, and can be expected to dominate the other sources of error in these experiments. First, S_e does generally depend upon ψ so that the interchange of ψ and s integration between equations (3.24) and (3.25) is not rigorously justified. The error in making this approximation, $E_i(\psi)$, can be estimated as

$$E_i(\psi) = \frac{\sqrt{\int_0^{\psi} d\psi' \left(S_e(\psi')-S_e(\psi)\right)^2}}{S_e(\psi)} , \qquad (4.8)$$

the volume weighted variance of $S_e(\psi)$. A typical value for $E_i(\psi)$ is 0.1. The second source of error occurs because $S_e(\psi)$ does not necessarily coincide with $S_i(\psi)$, the true upper bound for the integrals. Because of the insulating boundary conditions at the microwave window end of the system, which requires local net neutral flux there, the downstream parallel flux, integrated over ψ, must be neutral as well. This means that the variation of $S_e(\psi)$ and $S_i(\psi)$ must vanish when integrated across the plasma radius. In Chapter Three, it was noted that ionization between these two surfaces must be compensated for by radial diffusion upstream. Using the experimental diffusion coefficient to calculate the variance, then, in some sense begs the question. It can be argued qualitatively, however, that "wiggles" in $S_i(\psi)$ with radial scale R would be collisionally washed out over an axial distance L for

$$L > R \frac{\lambda_{io}}{r_{li}} .$$

Taking R to be the plasma radius, at the lowest pressures (1 mTorr), L approaches half of the plasma length. The variance of $S_i(\psi)$ about $S_e(\psi)$ would in this case be L/2, giving an estimated error of 25% in the worst case.

Chapter Five

Experimental Results

In the three sections which follow, the results of the ion transport experiments will be presented. We will begin with a general discussion of plasma behavior under variation of the external parameters in order to place the transport results in proper perspective. Thus oriented, we proceed in section two to examine the results of steady state transport measurements. The third section provides experimental verification of the Kelvin-Helmholtz instability predicted in Chapter Three and provides evidence for enhanced heat conduction into the scrape-off layer due to these fluctuations.

5.1 Experimental Observations

As previously stated, these experiments were performed on a commercial plasma source, the ASTeX S-1500. Pedigree notwithstanding, it proved host to a plethora of the non-linearities and instabilities generally expected of the plasma state. In Figure 5-1, which maps plasma behavior in pressure-power space for the symmetric mirror configuration, the difficulty in finding even a small region of quiescent plasma is manifest. Although the magnetic beach configuration produced qualitatively similar radial profiles to the symmetric mirror, poor tuning and noise rendered the quantification of ion transport in that configuration very difficult. The symmetric mirror configuration, on the other hand, proved fairly quiet and was thus chosen for the detailed transport measurements. The various regions of Figure 5-1 can be categorized as

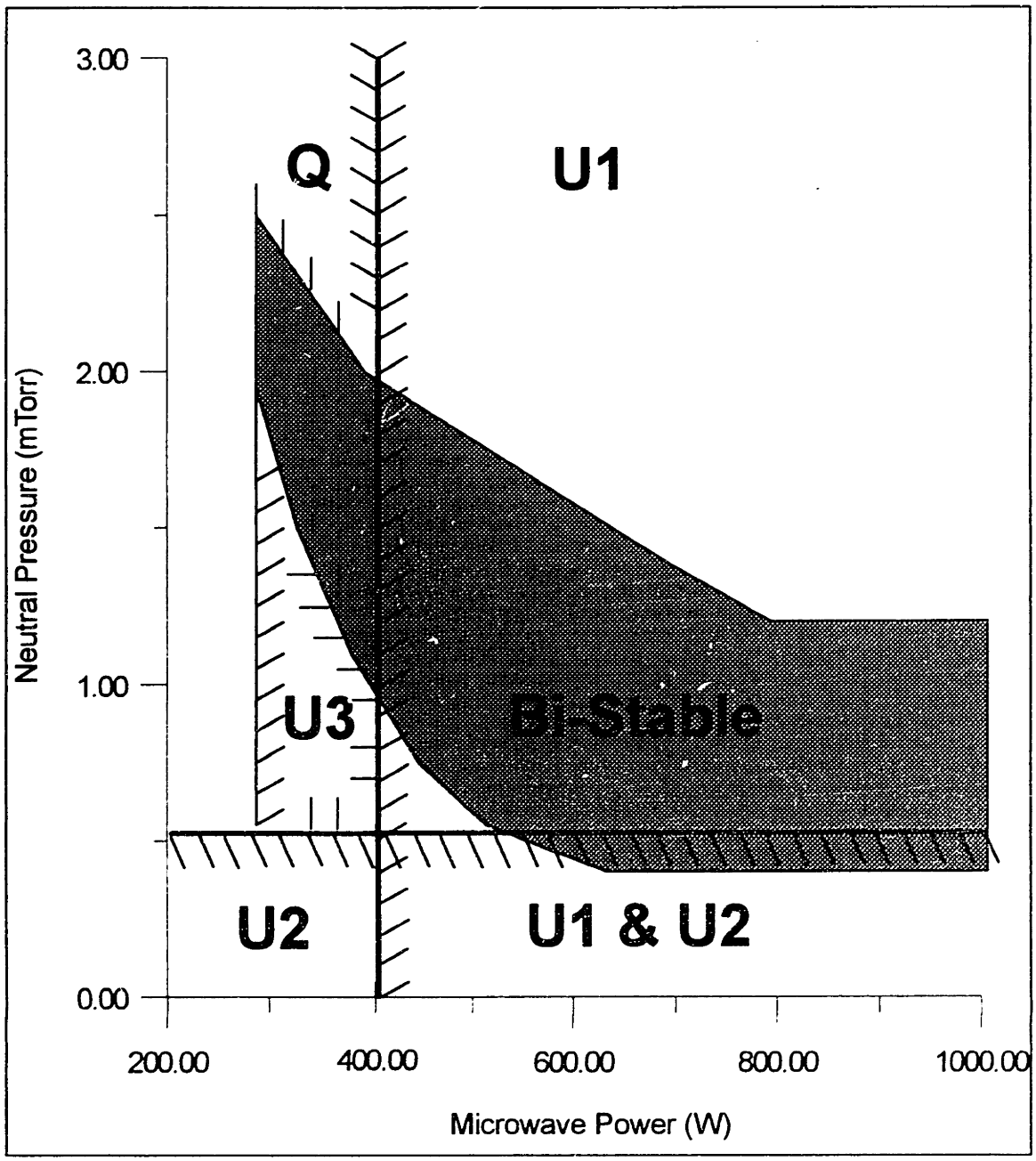

Figure 5-1: Global Plasma Behavior in Pressure-Power Parameter Space
Keyletters: U - Unstable
Q - Quiescent

quiescent, bistable or unstable. Each type of region will be discussed in a sub-section below. Since it is not possible for a single researcher to investigate thoroughly each of these phenomena, only behavior which bears direct relevance to the thesis topic has received in-depth treatment. A preliminary investigation of each region has, however, been undertaken, and probable mechanisms for the observed behavior determined.

Unstable Regions

Three unstable regions appear in Figure 5-1. The first, labeled U1 in the diagram, is observed to occur for microwave powers above approximately 400W and is not spatially localized. The second (U2) appears when pressure is reduced below 0.5 mTorr and possesses its largest amplitude in the region of strong density gradient which separates the core plasma from the scrape-off layer. The third (U3) is highly localized at the plasma edge and has been identified as a Kelvin-Helmholtz instability. These modes will henceforth be referred to as modes 1, 2, and 3 respectively. The frequency and direction of propagation for each mode is given in Table 5.1.

An oscilloscope trace of the floating potential variations associated with mode 1 is shown in Figure 5-2. No phase shift was observed between two probes separated by 90° in azimuth. Its frequency is well above ion cyclotron, but significantly below the ion plasma or lower hybrid frequencies. The most probable candidate for this mode is, then, an ion acoustic wave. That there appears to be an input power threshold associated with this mode suggests it might be one daughter wave from a parametric decay of the incoming whistlers. The decay of 2.45 GHz whistlers into MHz range ion acoustic waves is well documented [Porkolab et al., 1972]. Similar threshold behavior

Region (from Fig. 5-1)	Probable Classification	Frequency	Propagation Direction
U1 - Mirror U1 - Beach	Ion Acoustic Ion Cyclotron	1 MHz 20 kHz	b b, r
U2	Electron Drift	5 kHz	Electron Diamagnetic
U3	Ion Kelvin-Helmholtz	1-2 kHz	Ion Diamagnetic

Table 5.1: Classification of Collective Modes Observed in the Ion Transport Experiment

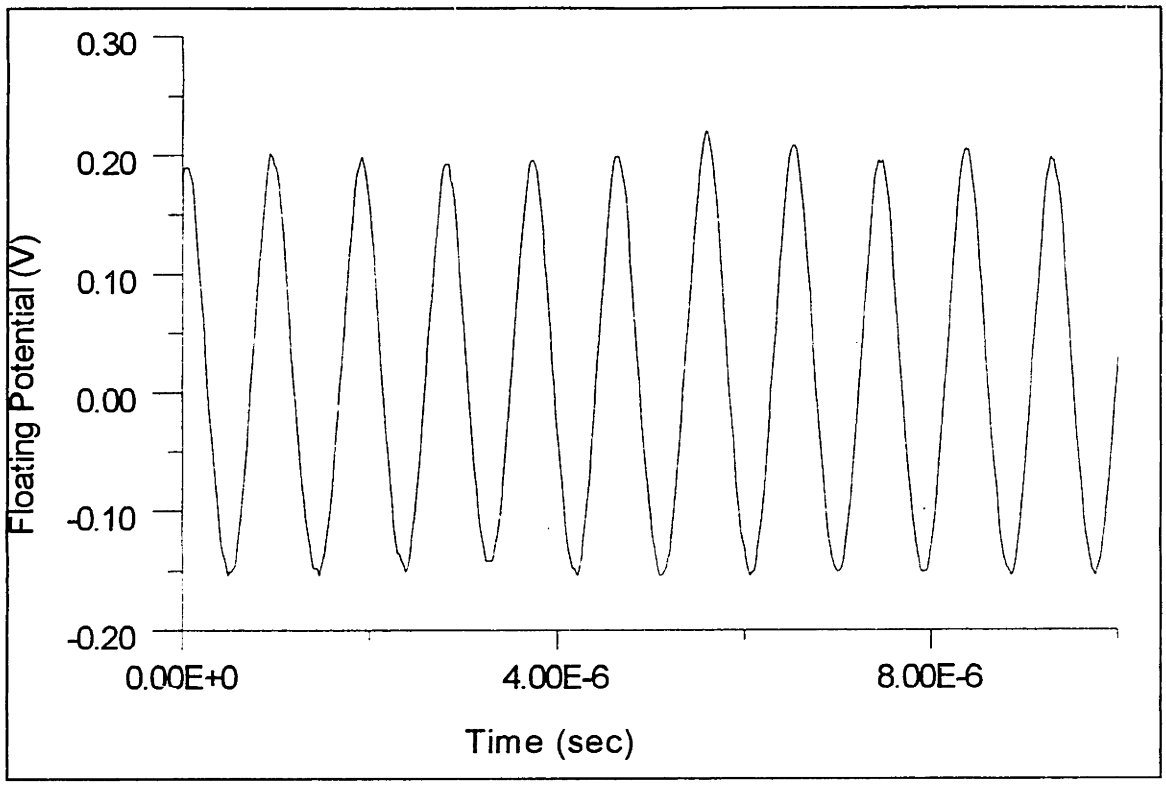

Figure 5-2: Floating Potential Fluctuations Associated with Region U1

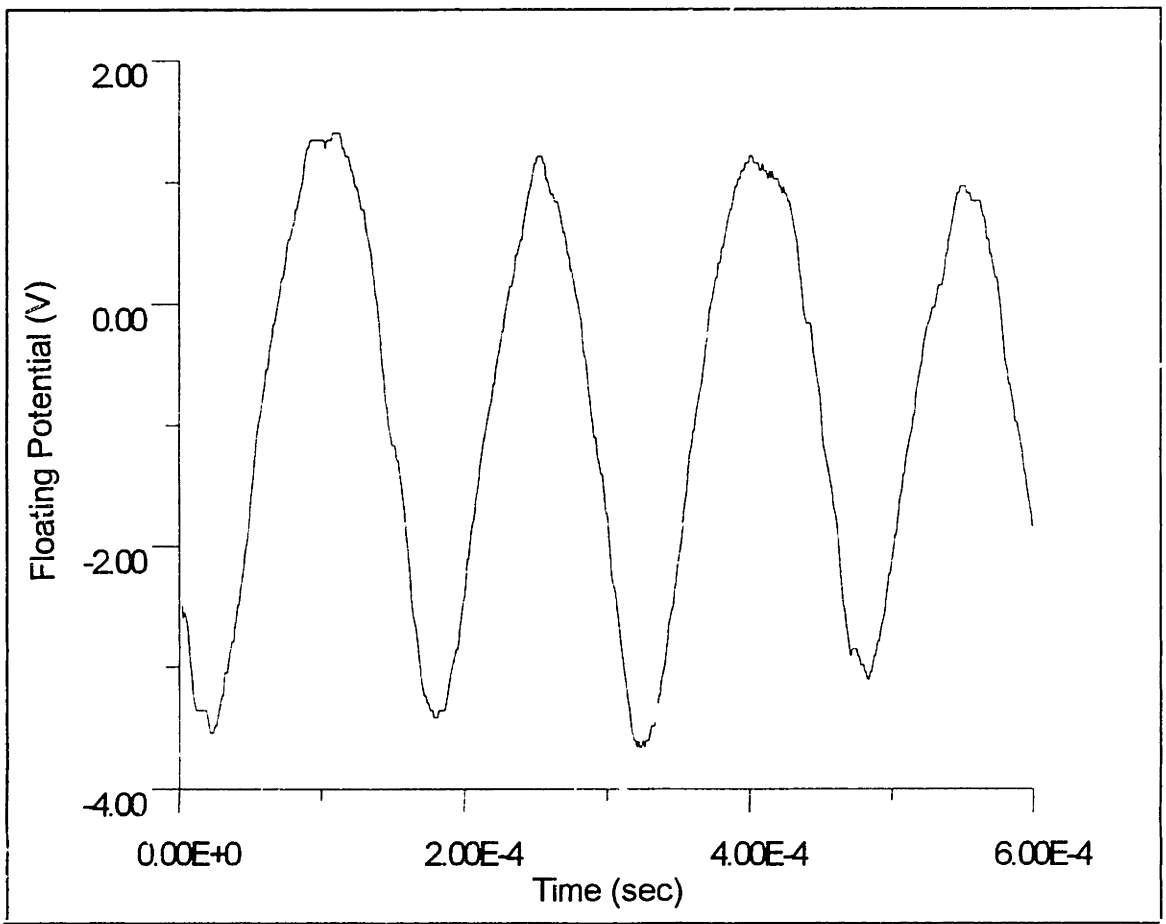

Figure 5-3: Floating Potential Fluctuations Associated with Region U2

($P_{th} \sim 400$ W) is observed for the magnetic beach configuration. The mode observed in that case, however, occurs at frequencies near and above the ion gyro-frequency, and shows some evidence of a radial wavenumber, suggesting that those waves are ion cyclotrons. In any event, these modes seem to have little effect upon the radial profiles, as would be expected for near parallel propagation and relatively high frequencies.

An oscilloscope trace of Mode 2 is shown in Figure 5-3. It is observed to propagate azimuthally in the direction of, and at frequencies near, the electron diamagnetic drift and is almost certainly a drift mode. Whether it possesses straight flutes or has helical structure was impossible to determine since the presence of a downstream probe drastically perturbed the mode. Since this wave appeared at neutral pressures well below those actually used in plasma processing (at least 1 mTorr equivalent of neutral flux is usually required in such applications) it did not warrant further investigation, although it was noted that the wave tended to smear out the usually sharp radial edge which the limiter places upon the parallel ion flux. Similar effects were observed in Mode 3, the Kelvin-Helmholtz instability, and are recorded along with detailed observations later in this chapter.

Bistable Region

The existence of an abrupt transition from a low T_e, high density plasma state to a high T_e, low density state as neutral pressure is decreased through some critical value (and back again, with hysteresis, as neutral pressure is increased) was noticed early on for ECR sources [Gorbatkin, et al. 1988]. The changes in these values across the transition are generally less than a factor of 2 (1/2). A theory was put forward by Dandl and Guest [Dandl and Guest, 1991]

to explain this behavior based on particle and power balances, but it predicted a transition pressure which was much too low (10^{-4} Torr) and electron temperatures (after the high to low pressure transition) of approximately 70 eV, an order of magnitude too high. Aydil et al. found [Aydil et al., 1993], not surprisingly, that it was in fact neutral density, and not neutral pressure, which parameterized the transition point.

Such a transition has been observed in the plasma of this experiment. The parameterization of the transition point in terms of pressure and power (we actually measured neutral density) is shown in the region marked bi-stable in Figure 5-1. The most salient feature of this region is the decrease of transition pressure with increasing microwave power. Depending upon the microwave tuning, the transition could occur anywhere in the bistable region. Figure 5-4 shows normalized axial profiles of plasma density, electron temperature, and plasma potential on either side of the transition pressure. No significant difference in the axial structure of the two modes is observed, which implies that the transition cannot be attributed to a change in axial eigenmode. There do exist, however, significant differences in the radial profiles on either side of the transition pressure. Discussion of these differences is deferred to the last section of this chapter, where it will be made clear that the transition does not represent a change in the radial eigenmode of the plasma.

The most plausible explanation of this change of density concerns the coupling of ECH power into a plasma. Carl et al. [Carl et al., 1991] showed, experimentally, that the effect could be attributed to mode-conversion and subsequent absorption of the LHCP component of the whistlers based on calculations by Musil and Zacec [Musil and Zacec, 1972] for an infinite plasma. With the plasma density sufficiently high such that $\omega < \omega_{pe}$ in the plasma bulk, where ω is the frequency of the incoming wave, the LHCP

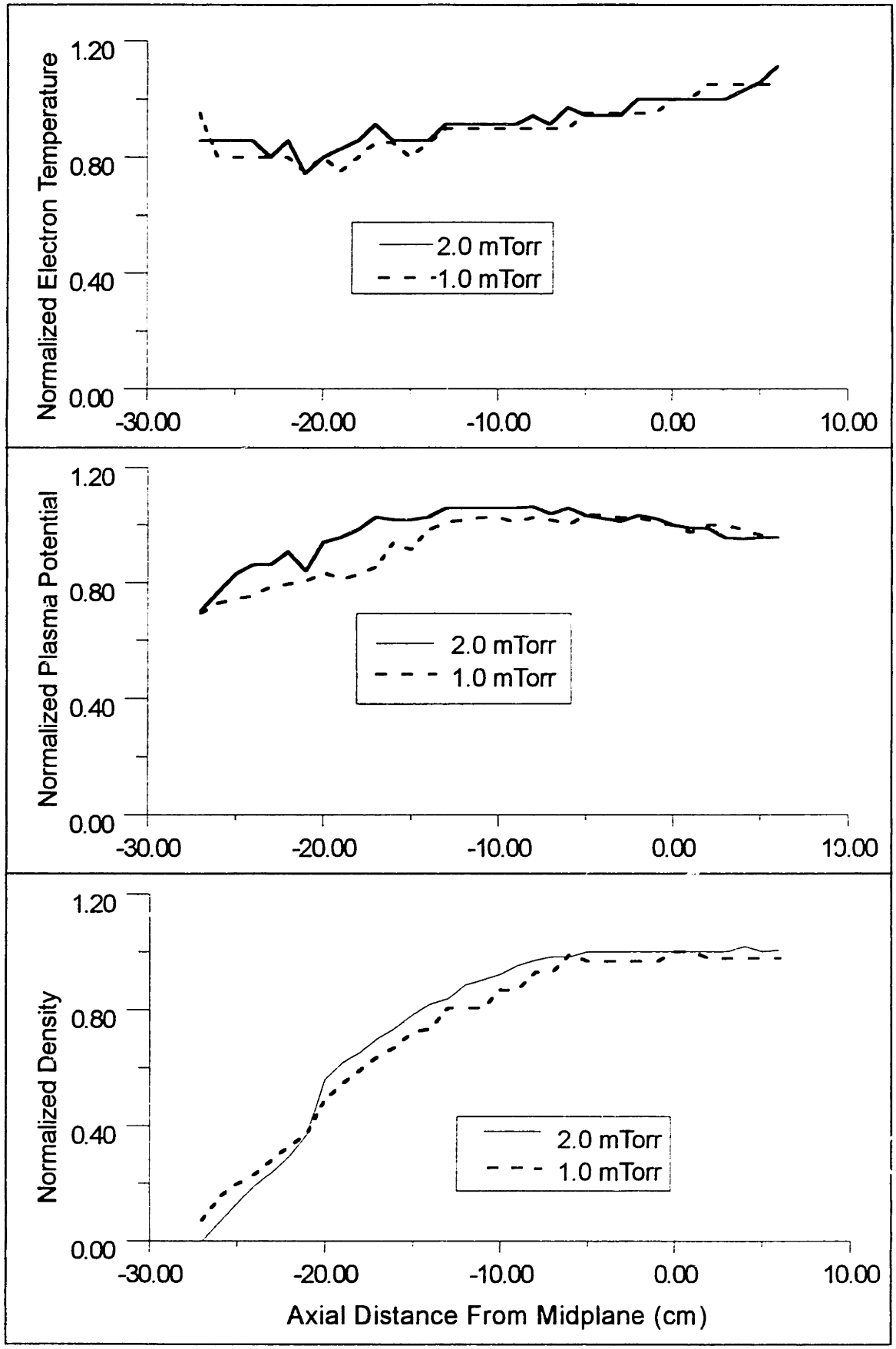

Figure 5-4: Normalized Axial Profiles Before and After Mode Transition

component of the wave can mode convert to RHCP in the layer near the window where the density is low and $\omega = \omega_{pe}$, and be subsequently absorbed at the resonance zone. Below this critical density, the LHCP portion is evanescent and gets reflected, thereby decreasing the plasma density. In our case the effect seems to occur at higher densities than this, but may be accounted for by the fact that two thirds of the plasma volume in the resonance zone is in the shadow of the limiter and of significantly lower density than the core.3

Parametric Variation

With a general picture of plasma behavior throughout the parameter space now established, we proceed to discuss the parametric variation of bulk quantities such as density and temperature. The variation of electron temperature and plasma density with microwave power at 3.0 mTorr are shown in Figure 5-5. The electron temperature is seen to increase weakly with increased power, while the density increases nearly linearly with power. Between 300 W and 1000 W the ionization fraction increases from slightly below 3% to greater than 8% for a pressure of 3 mTorr.

The variation of electron temperature, plasma density, and plasma potential with neutral pressure at 300W is shown in Figure 5-6. The precipitous drop in density between 1.5 mTorr and 1.0 mTorr results from the mode transition discussed above. In fact, the data at 1.5 mTorr, for all the experimental results shown, were taken for a microwave power of 330 W and not 300 W. This is because the transition occurs near 1.8 mTorr at 300 W, and high reflected powers occurred for low mode operation above approximately 1.2 mTorr. Thus, high mode was artificially maintained with

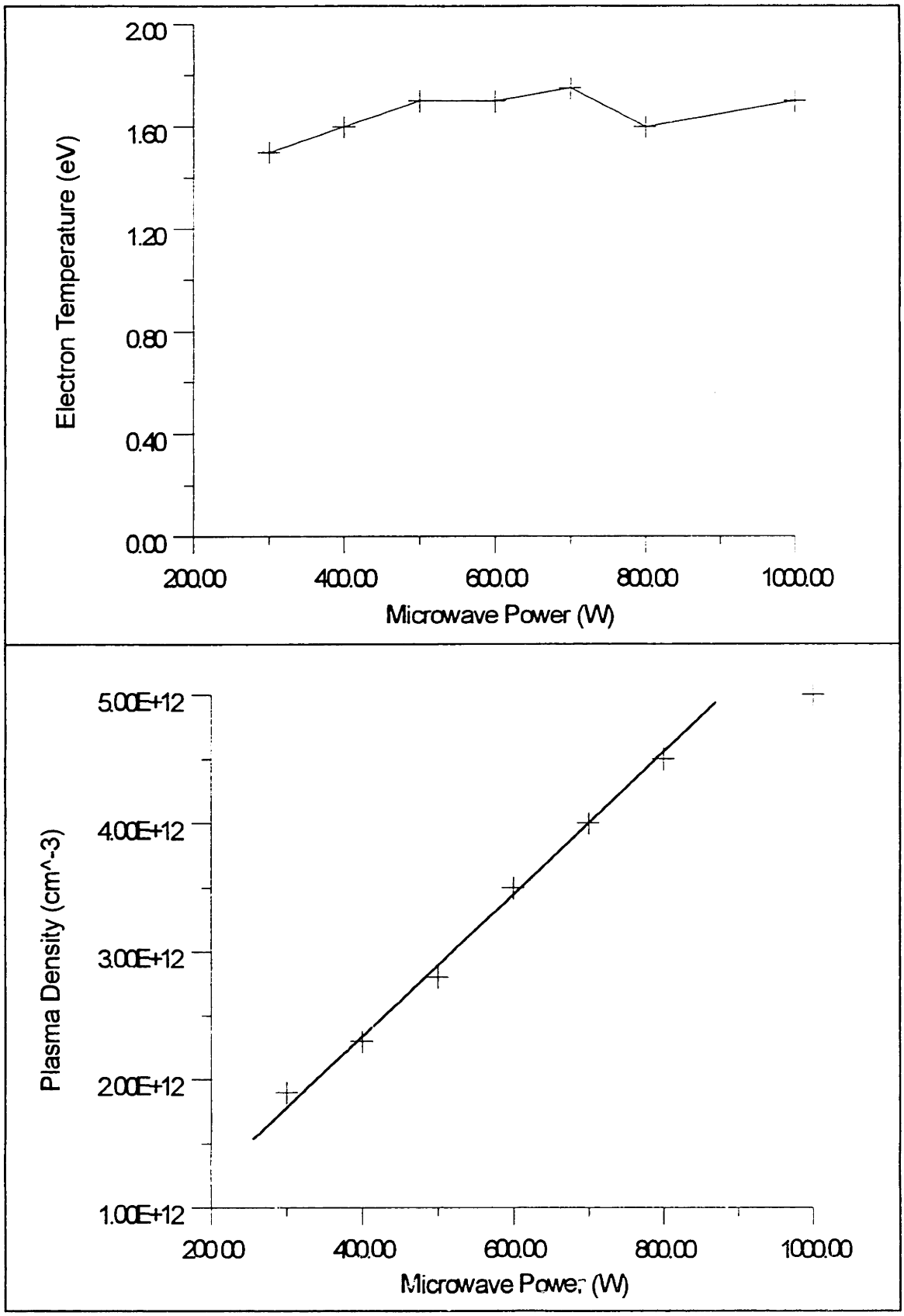

Figure 5-5: Variation of Plasma Density and Electron Temperature with Microwave Power for 3.0 mTorr Neutral Pressure.

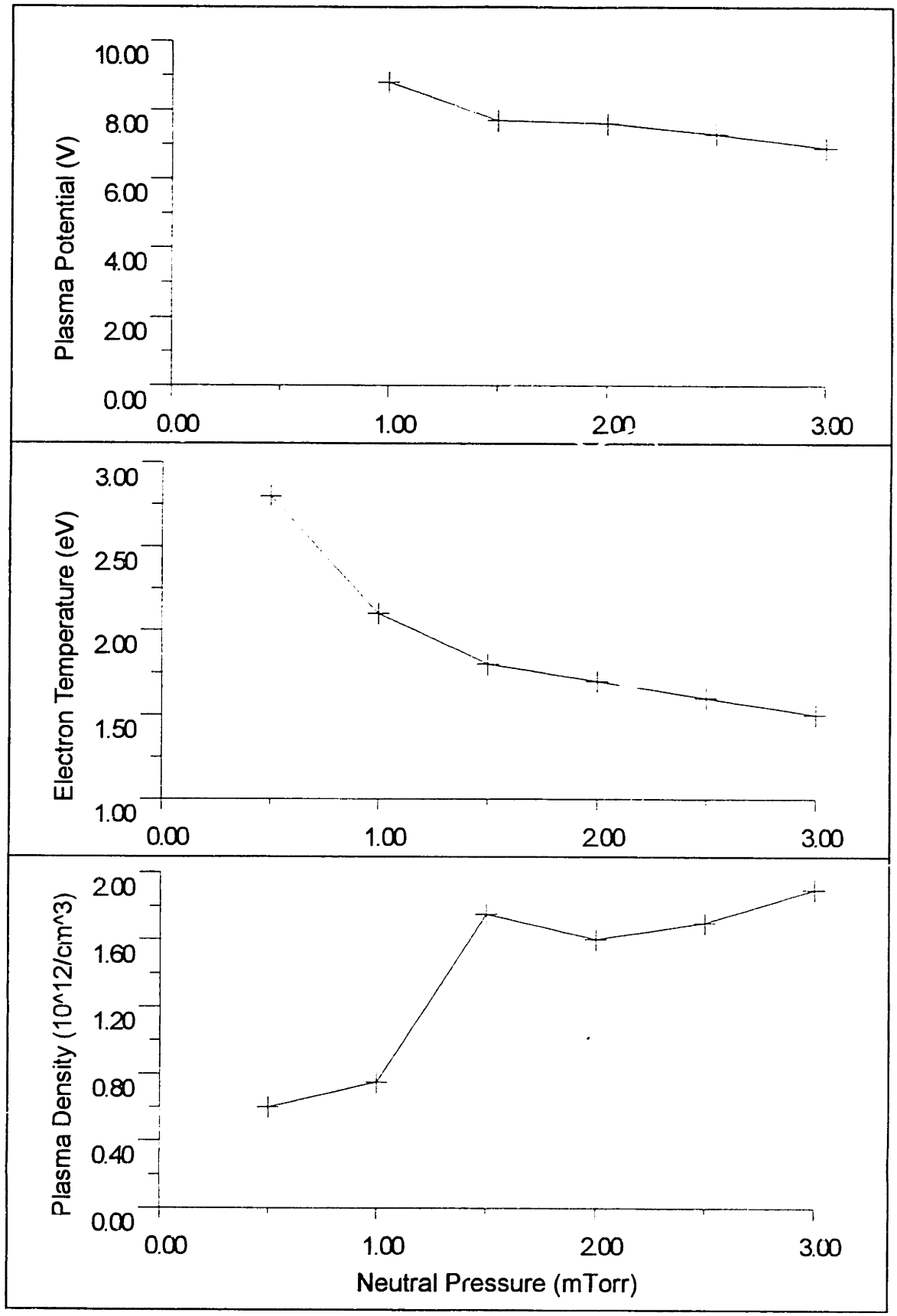

Figure 5-6: Variation of Plasma Parameters with Neutral Pressure at 300 W

the minimum possible enhanced power, 330 W, in order to maintain the good tuning. Electron temperature and plasma potential are likewise observed to vary little over the high-mode pressure range, but are enhanced significantly upon transition to low-mode.

Ion temperatures in the core plasma were observed to remain nearly constant over the range of 3.0-1.0 mTorr for 300 W of microwave power, as shown in Figure 5-7a. The variation of ion temperature with power was somewhat more difficult to ascertain. Figure 5-7b shows peak-normalized ion energy distribution functions for the power range 300W-1250W (3.0 mTorr). The distributions in the 450-800 W range are observed to change continuously from monomodal to bimodal form. The occurrence of this splitting correlates precisely with the onset of the instability occurring in region U1 of Figure 5-1. Because the frequency of these fluctuations (~1 MHz) vastly exceeds the sweep frequency of the RFA, temporal resolution of the distribution function on a timescale shorter than the fluctuation period was impossible. We note, however, that the full width at half maximum for the individual peaks, when well separated, is not much greater than that of the monomodal distributions. It is therefore clear that the bimodal distribution function derives from the mechanism mentioned in Chapter 2. That is, we are observing the time average of the shifts in ion streaming energy caused by modulation of the plasma potential due to a collective mode. At the highest power levels the instability is observed to vanish, and the distribution function returns to monomodal form with essentially the same full width at half maximum which existed at the lowest power levels. Thus it appears that neither power nor pressure alter, significantly, the ion temperatures over the parameter regime studied here.

In Chapter Two, a number of scaling arguments were made based upon

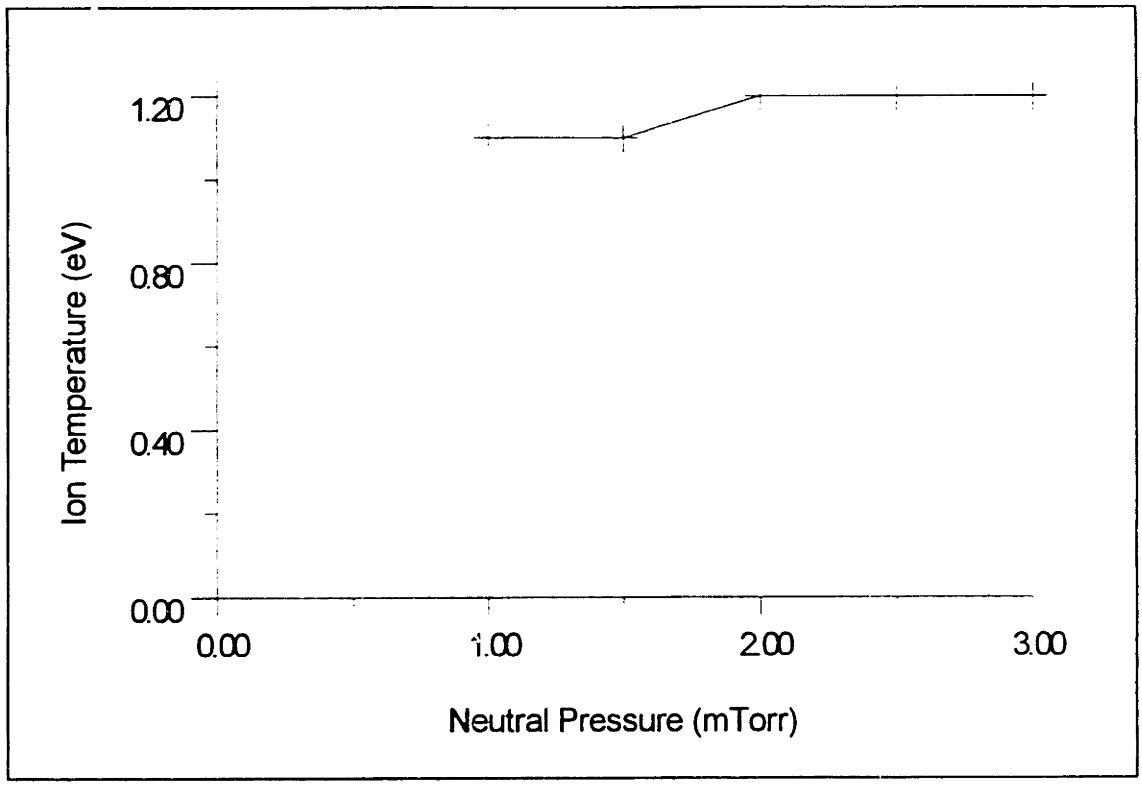

Figure 5.7a: Variation of Ion Temperature with Neutral Pressure

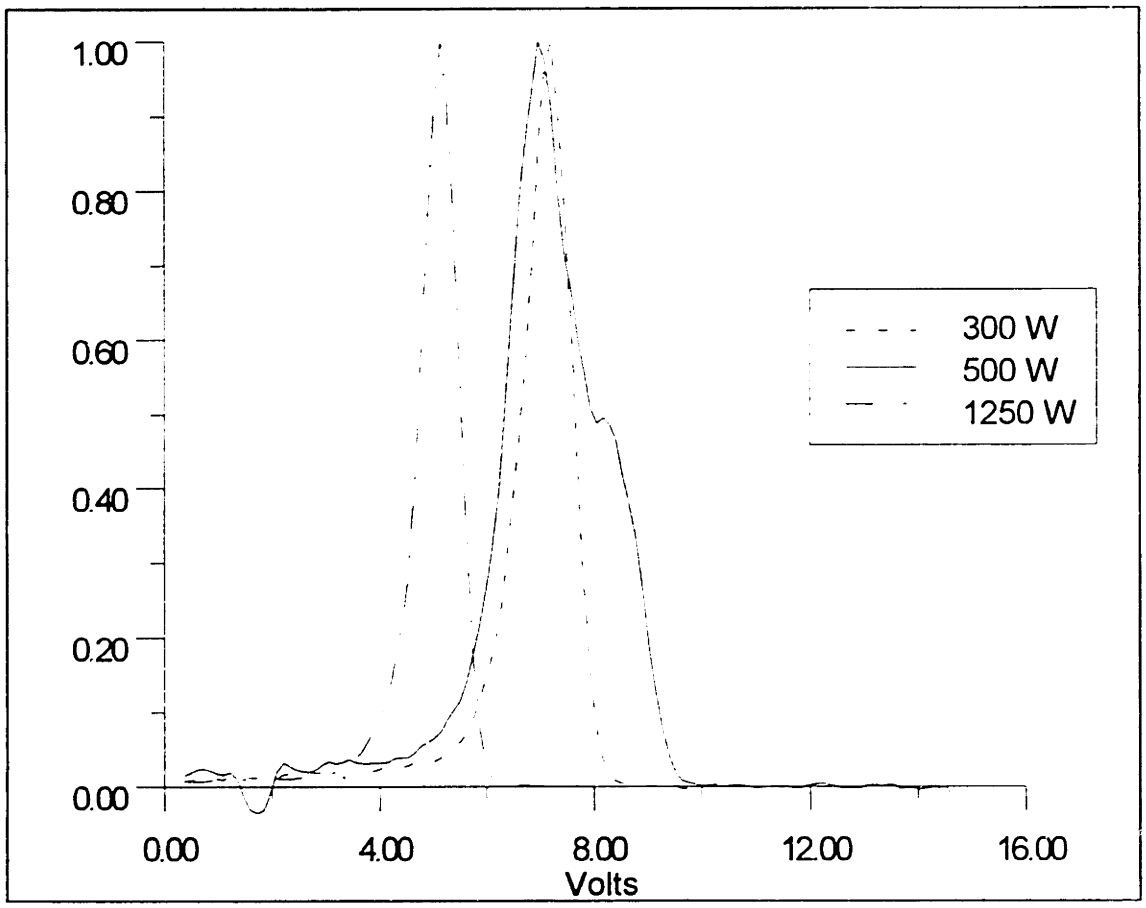

Figure 5-7b: Peak Normalized IEDF's at 3.0 mTorr

ion confinement times within the plasma. We now proceed to justify these assumptions. Figures 5-8a and b show the variation of average ion flux to the wafer with pressure and power, respectively. From these flux values and the densities of Figures 5-5 and 5-6, the confinement times of Figure 5-9 are calculated. The values shown in Figure 5-9 are all in accord with the assumptions of Chapter Two.

5.2 Experimental Determination of Ion Transport

The interpretation of the transport coefficients derived in Chapter Three can, as was stated there, be quite difficult for situations where gradients vary significantly over a random-walk step size. Indeed, the results of the present chapter will place into sharp focus the inadequacy of assuming a *local* constitutive relationship between fluxes and gradients in density and potential under such circumstances. On the other hand, the evaluation of the perpendicular flux in terms of the axial flux and ionization (equation 3.25) is perfectly general, so that any expression at all can be inserted for $\Gamma_\perp$. In this way, one may evaluate candidate models for transport in the same manner as one would check the diffusion model; that is, their coefficients can be experimentally determined and checked against theory, where theoretical expressions for these exist.

In order to give as much physical insight as possible into the ion transport results, this section will present a number of radial profiles of both raw and processed data. At this point we define the flux surface, ψ_L which maps to the limiter inside edge, as a convenient reference for discussing features. The radius for ψ_L at the midplane is 0.043 m, and all data presented will be mapped to the midplane position. The liner is at a radius of 0.068 m.

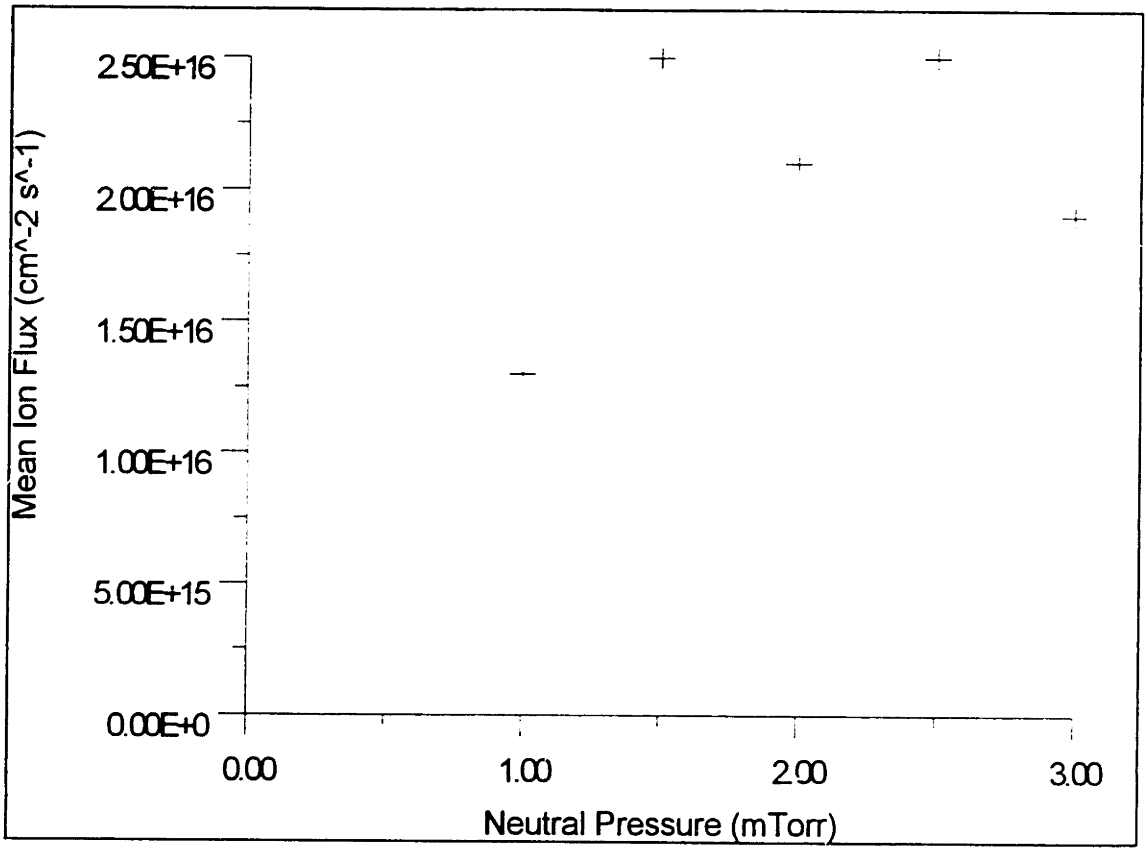

Figure 5-8a: Pressure Variation of Ion Flux at 300 W Microwave Power

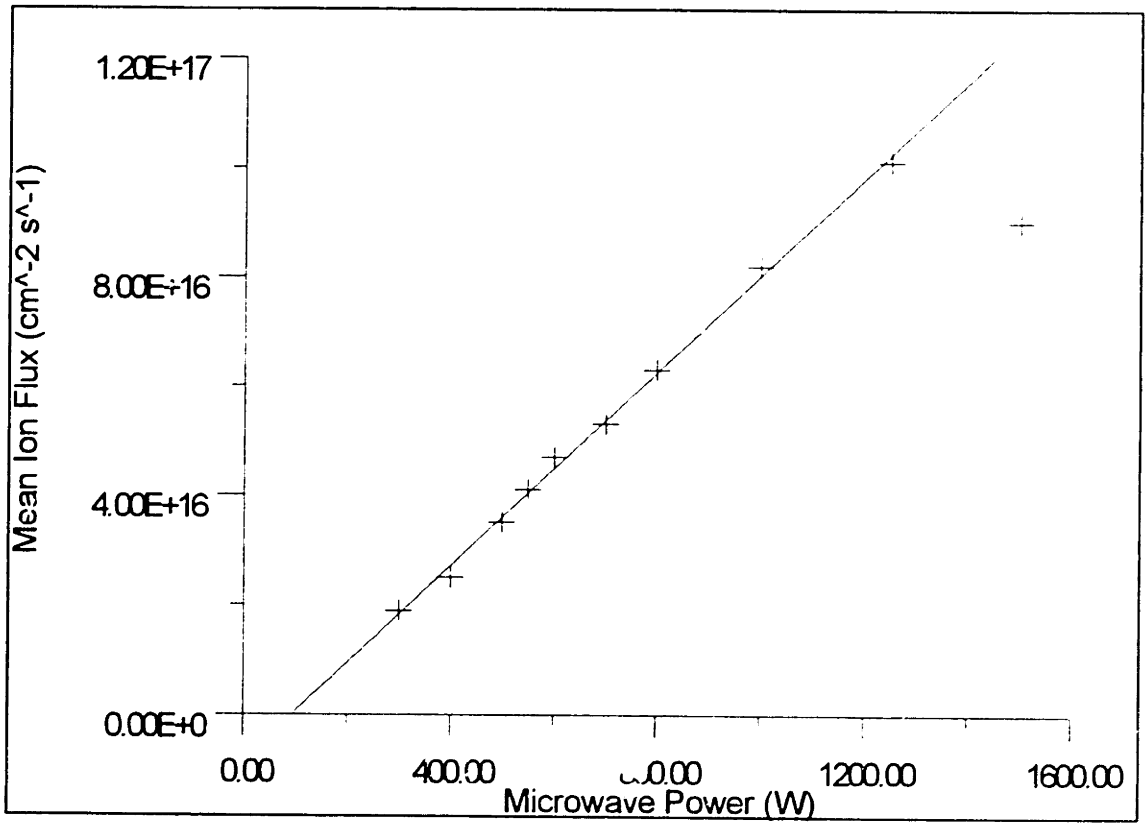

Figure 5-8b: Microwave Power Variation of Ion Flux at 3.0 mTorr

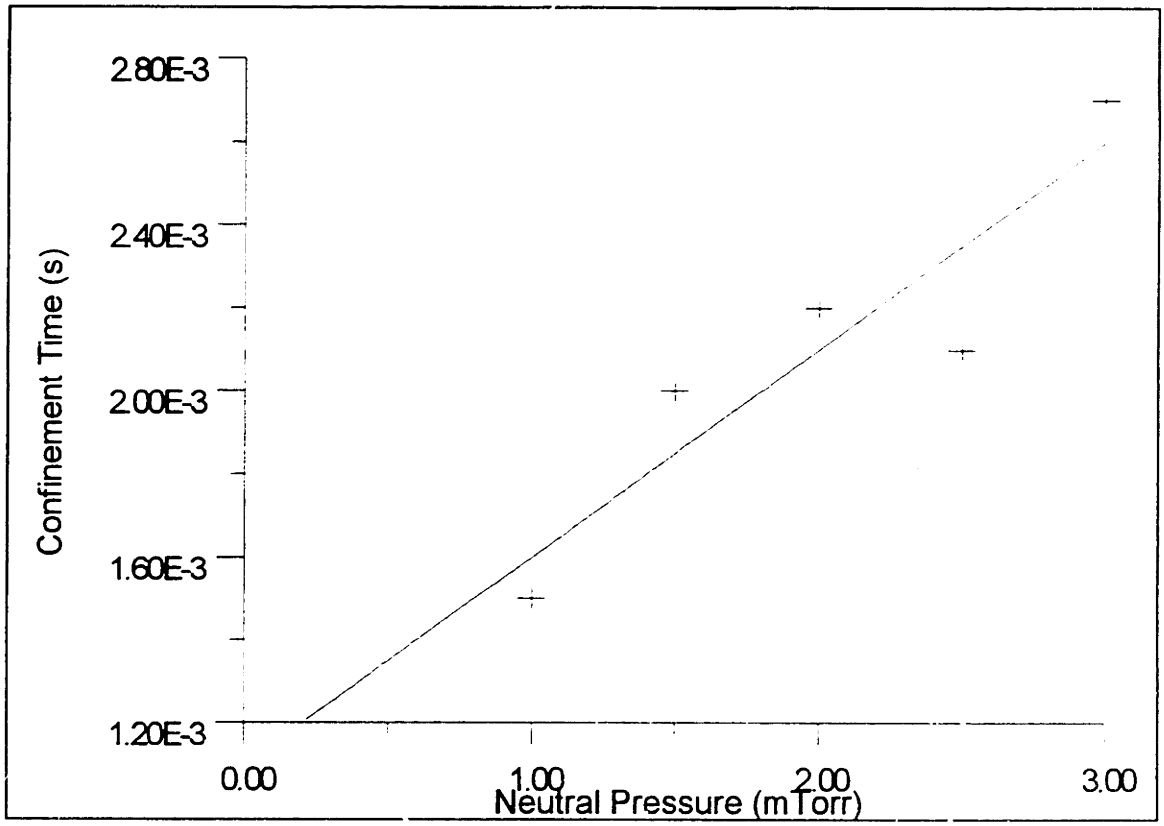

Figure 5-9a: Pressure Dependence of Ion Confinement Times at 300W

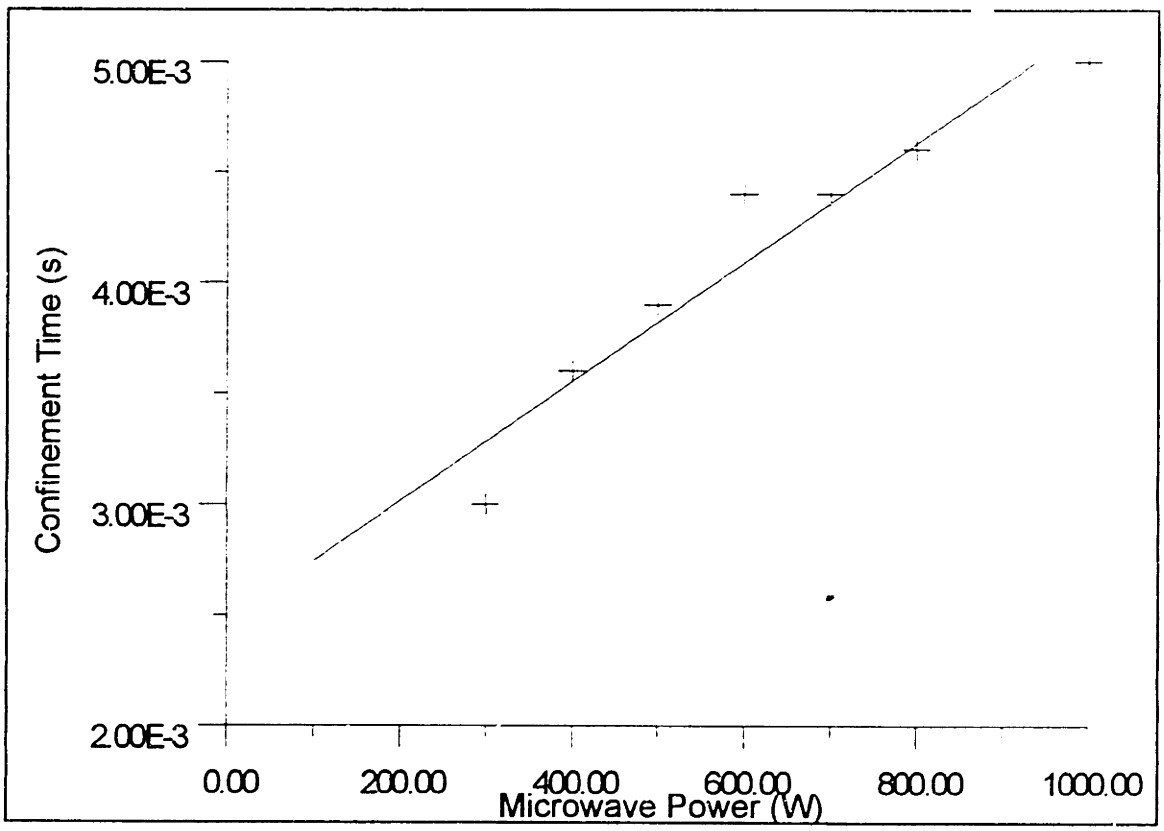

Figure 5-9b: Power Dependence of Ion Confinement Times at 3.0 mTorr

Raw Data

Electron Temperature

Figure 5-10 shows a typical radial electron temperature profile. In all cases, the temperature remains essentially constant over the center two centimeters of the plasma, and undergoes a slight dip followed by a sharp rise before decaying away outside of ψ_L. This rapid decay of electron temperature in the absence of parallel heat flux from the resonance zone is to be expected due to the low perpendicular electron thermal conductivity. At radii greater than approximately 0.055 m, the electron temperature appears to increase.

In this region ($r > 0.055$m) the hyperbolic tangent fit to the FDP I-V characteristic proves to be less than satisfactory, as shown in Figure 5-11. Qualitatively, the distribution appears to be composed of a cold (< 1eV), roughly thermal component, and a much hotter (order 5-10 eV) non thermal part. The plotted temperature in Figure 5-10 represents a "best fit" of the presumed hyperbolic tangent functionality and should, in light of the large departure of the I-V characteristic from this form, be looked at skeptically for the outermost radii. We also show a power law fit to the initial electron temperature decay. This fit drops lower than 0.1 eV in the extreme plasma edge.

The probable explanation for the enhanced electron temperatures at the largest radii invokes e-e-i recombination. As shown in Chapter Three, this mechanism can become operative in plasmas as dense as this one for electron temperatures which are a small fraction of an eV. Thus, if the true bulk electron temperature were represented by the power law fit of Figure 5-10,

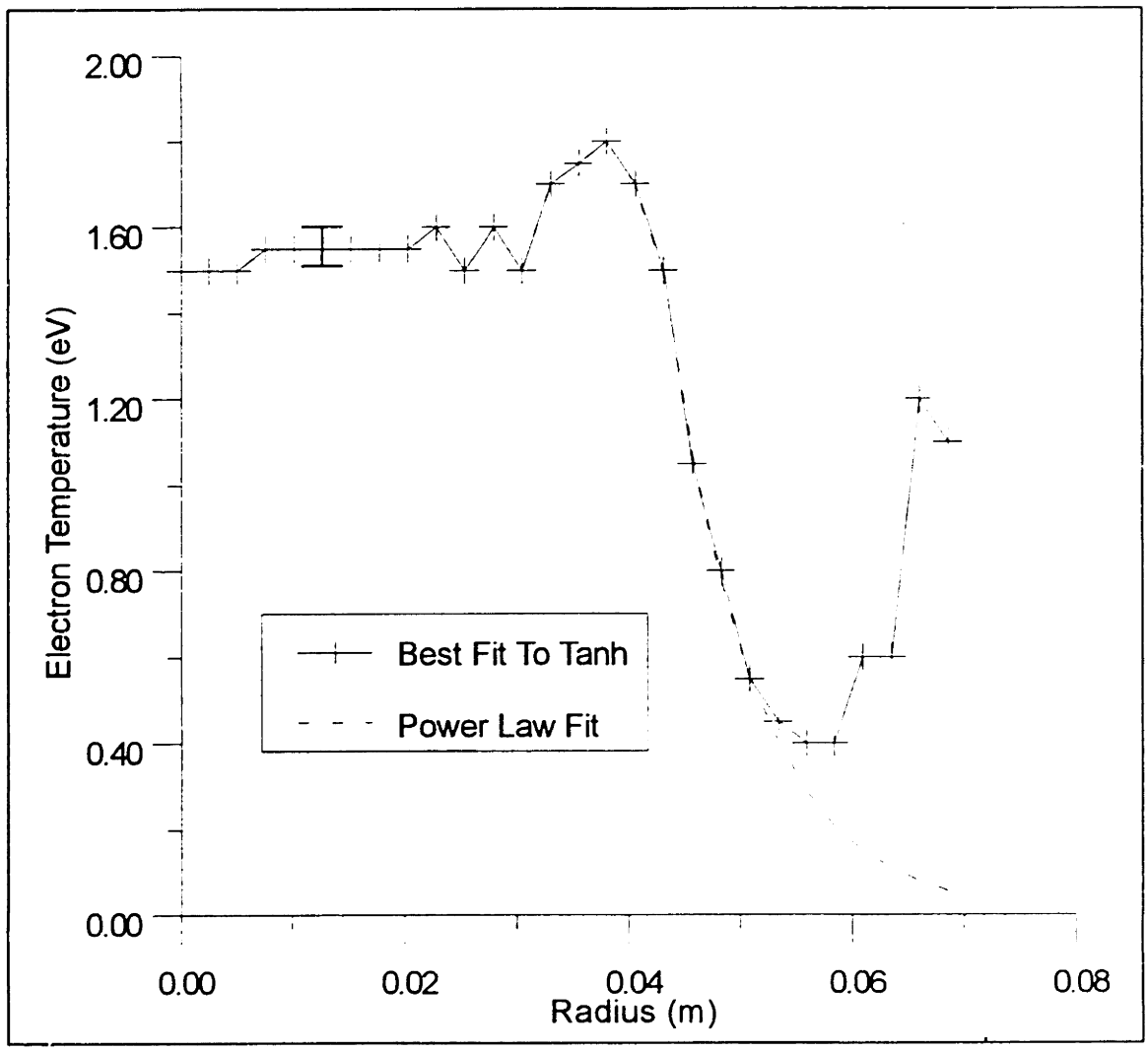

Figure 5-10: Radial Dependence of Electron Temperature for 3.0 mTorr, 300 W Best Fit to Assumed Hyperbolic Tangent is Shown Along With Power Law Fit to the Initial Temperature Decay in the Scrape-Off Layer

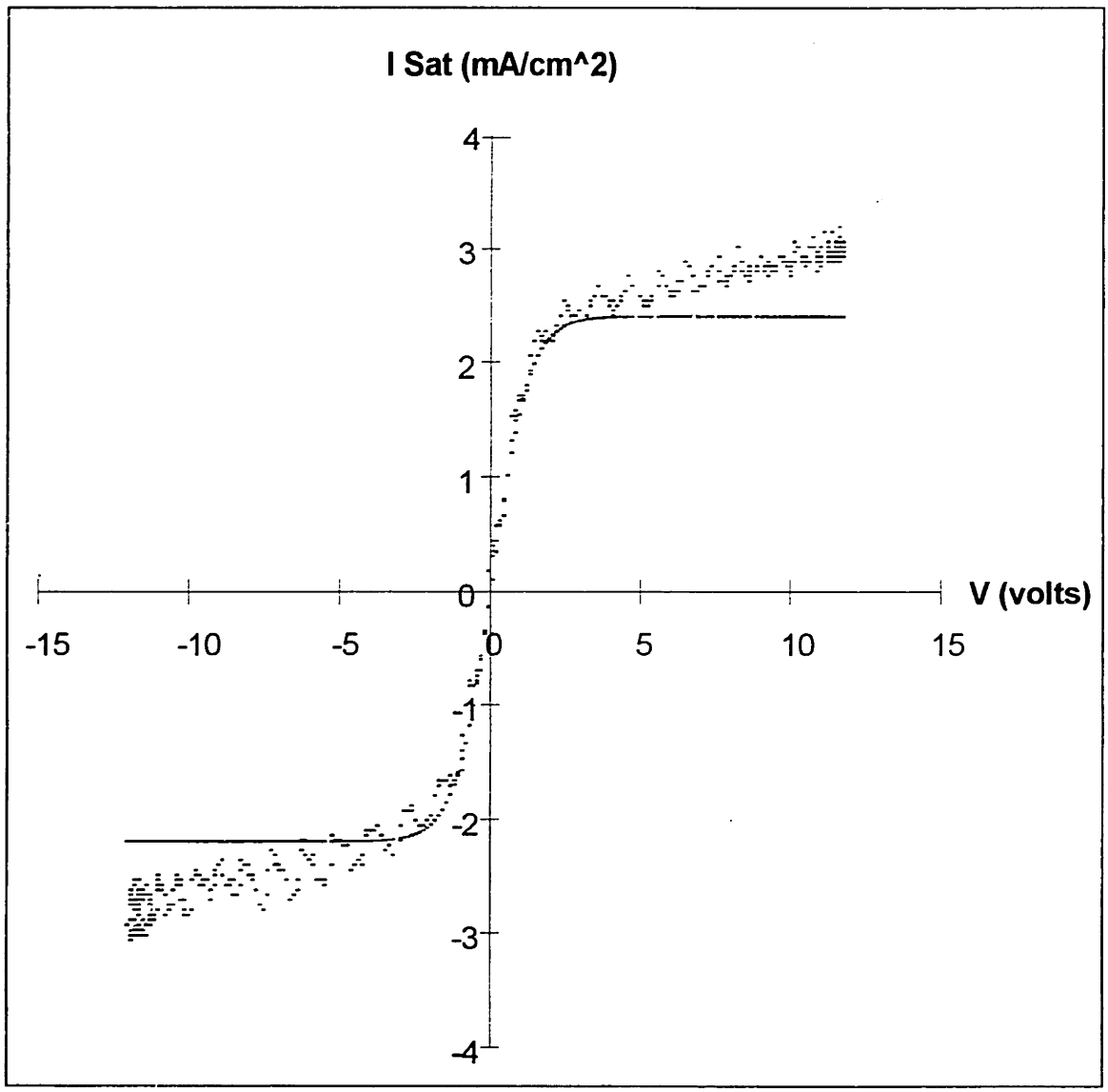

Figure 5-11: Typical Floating Double Langmuir Probe Trace in the Outer Edge of the Scrape-Off Layer.

there might be significant e-e-i recombination. Even if the non-recombining electron carries away, on average, only a small fraction of the 15.75 eV Ar first ionization potential (i.e. the collision places the recombining electron into a high level orbital from which it radiatively decays), a non-thermal component to the electron distribution function would be created for sufficiently high recombination rate. Below, we will show that if the power law fit for bulk electron temperature is assumed, e-e-i recombination occurs at rates smaller than, but comparable to, radial ion transport into this region.

Plasma Potential

Like electron temperature, plasma potential remains approximately constant over the center two centimeters as shown in a typical radial profile, Figure 5-12. In the region immediately interior to the scrape-off layer it dips slightly, and then rises sharply at ψ_L. The potential at radii external to ψ_L depends critically upon the behavior of the electron distribution function. In Figure 5-12 we have shown results for "best fit" electron temperature, and power law fit, which represents a lower bound since it does not take into account the effects of the hot electrons upon plasma potential.

The apparent reason for the existence of the potential step of 1-2 eV (several ion temperatures) at ψ_L is to impede the radial transport of the ions into the scrape-off layer. This potential step is a universal feature of the limited plasmas which have been investigated in this thesis. The fact that this structure possesses radial extent smaller than both an ion Larmor radius and ion-neutral mean free path renders interpretation of transport in terms of a diffusive model rather dubious. Indeed, it behaves much more like a sheath which, unlike the typical case, serves to hold the (radially) more mobile ions in.

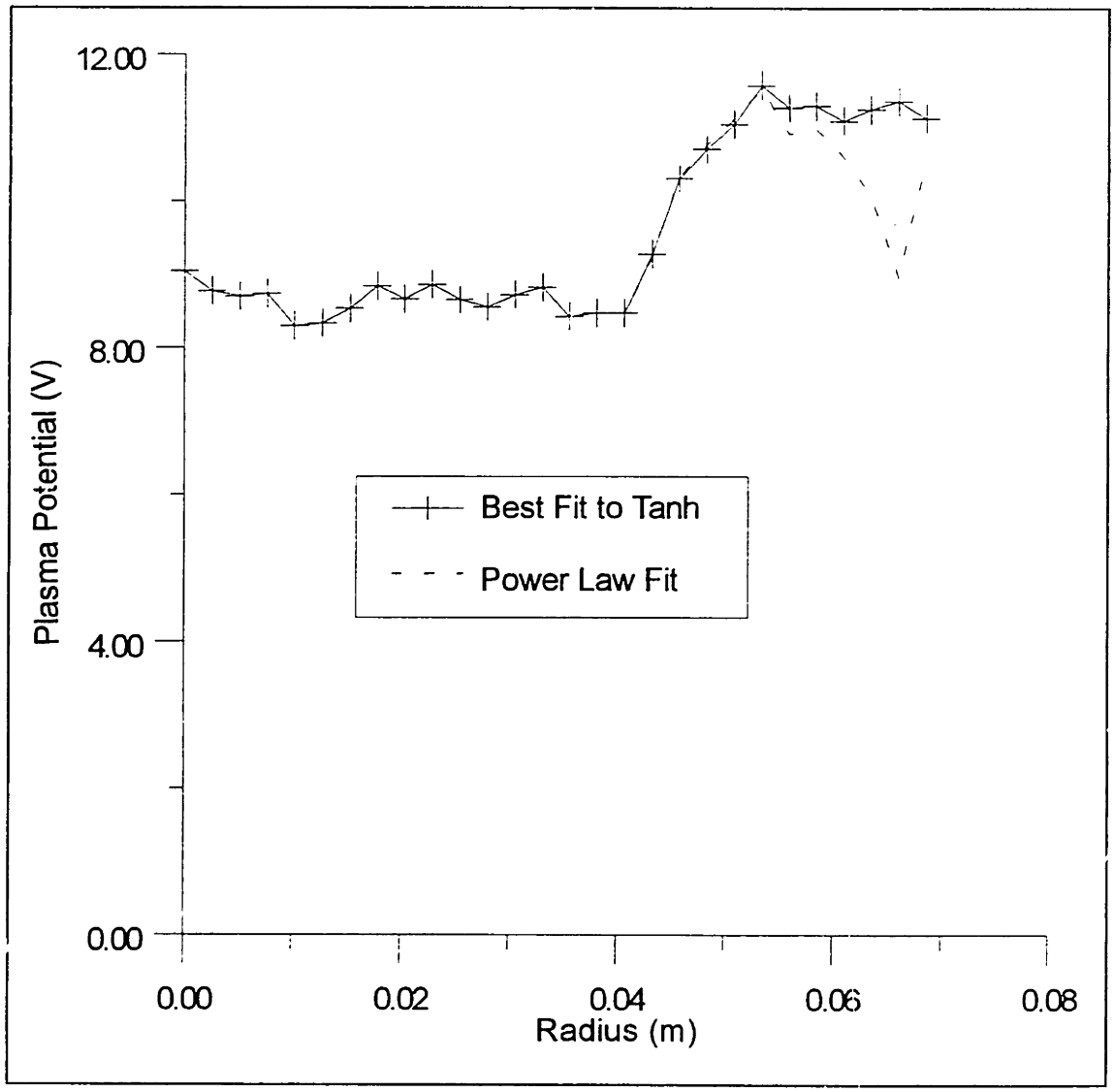

Figure 5-12: Radial Dependence of Plasma Potential for 2.0 mTorr, 300W Shown are Data Using Best Fit to the Assumed Hyperbolic Tangent, and Power Law Fit to the Initial Electron Decay in the Scrape Off Layer.

Electrons located in the vicinity of this region of strong electric field are swept into the scrape-off layer at approximately twice the rate caused by the pressure gradient alone. Once in the scrape-off layer, they rapidly cool. The combination of low electron temperature and enhanced plasma potential immediately exterior to the potential step drastically reduces electron axial flux to the wafer, due to its Boltzmann factor dependence on the ratio of these two quantities. With radial ion flux attenuated by the potential jump, a gradual roll off of plasma potential exterior to the jump might be expected in order to enhance electron endloss in this region. The potential should turn up again near the liner to repel the more mobile ions from the liner wall. Local equilibration of the radial ion and electron fluxes is, as previously discussed, not required due to the conducting axial boundary.

Plasma Density

The radial variation of plasma density appears in Figure 5-13. The most notable feature of this profile is the cusp which occurs at ψ_L. The cusp is observed for all pressures and powers regardless of magnetic field configuration (mirror or beach) when azimuthally propagating modes are absent. The consistent appearance of so sharp a feature in a system where ion Larmor radii and collisional mean free paths are on the order of centimeters is nothing short of remarkable, and provides further evidence that explanation of these profiles in terms of a diffusion equation may lack justification. The cusp must almost certainly be related to the strong radial electric field which exists on the flux surfaces near ψ_L.

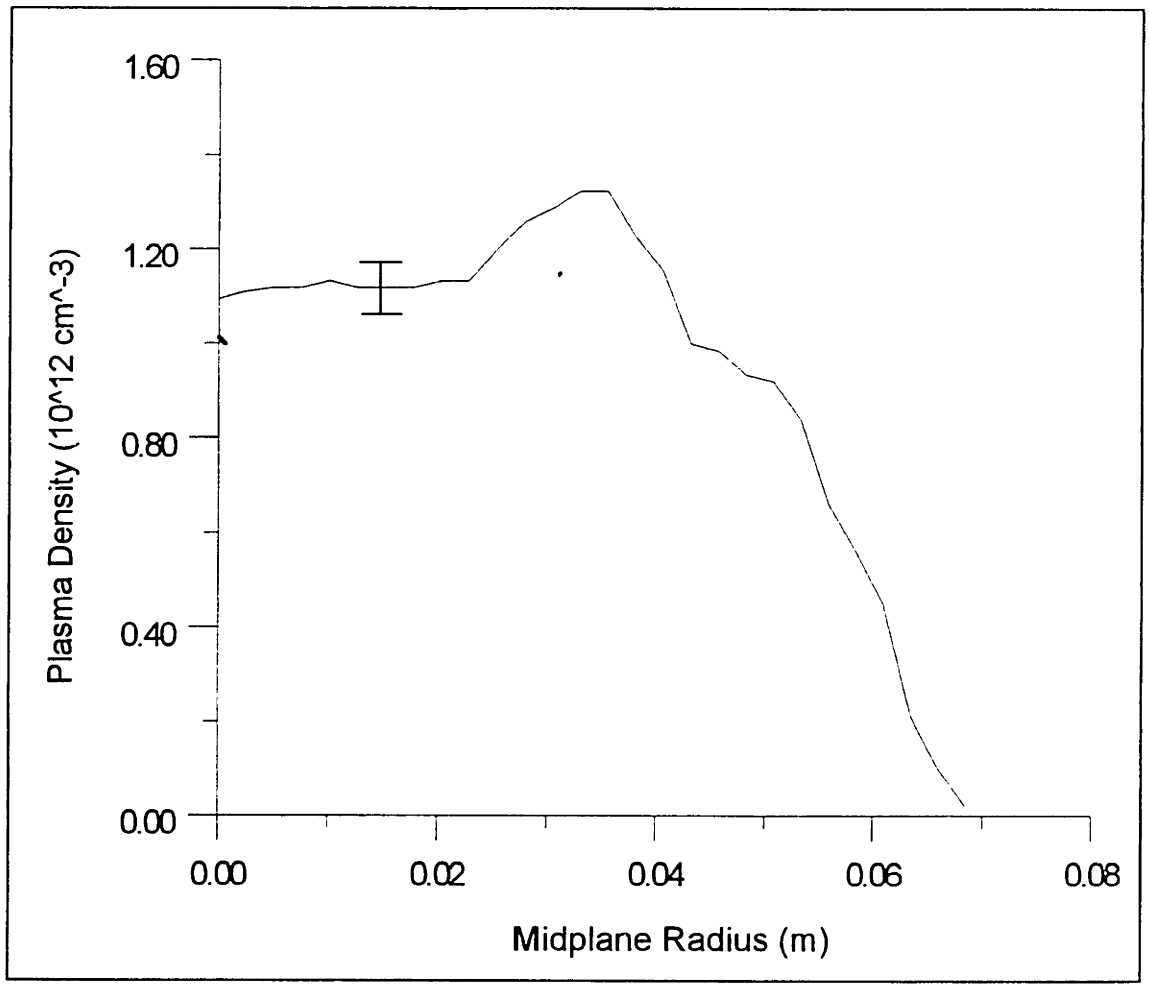

Figure 5-13: Radial Variation of Plasma Density for 2.0 mTorr and 300 W

Axial Ion Flux

The ion flux to the wafer is shown mapped back to the midplane in Figure 5-14. It possesses the complicated internal structure of the density profiles and the concave up decay in the scrape-off layer reminiscent of the electron temperature profiles.

Ion Temperatures

Typical radial variation of ion temperature is shown in Figure 5-15. The ion temperature in the core plasma remains essentially constant at approximately 1 eV for all plasma conditions studied in this thesis (Figure 5-7). Like the electrons, the ion temperature falls off rapidly outside of ψ_L. Although ion thermal conductivity across the magnetic field is much greater than that of electrons, frequent collisions with neutrals provide a large energy sink.

Derived Quantities

Ionization

Plotted in Figure 5-16 is the total ionization in a "cylindrical" shell of area $d\psi = 2\pi r\epsilon$, with ϵ the separation between data points (1.76×10^{-3} m at the midplane), for a typical case. Not surprisingly, the vast majority of ionization occurs on the flux surfaces adjacent and interior to ψ_L, where the electron temperature peaks. Superimposing the "shell integrated" axial ion flux on the ionization (Figure 5-17) makes clear that roughly half of the ion

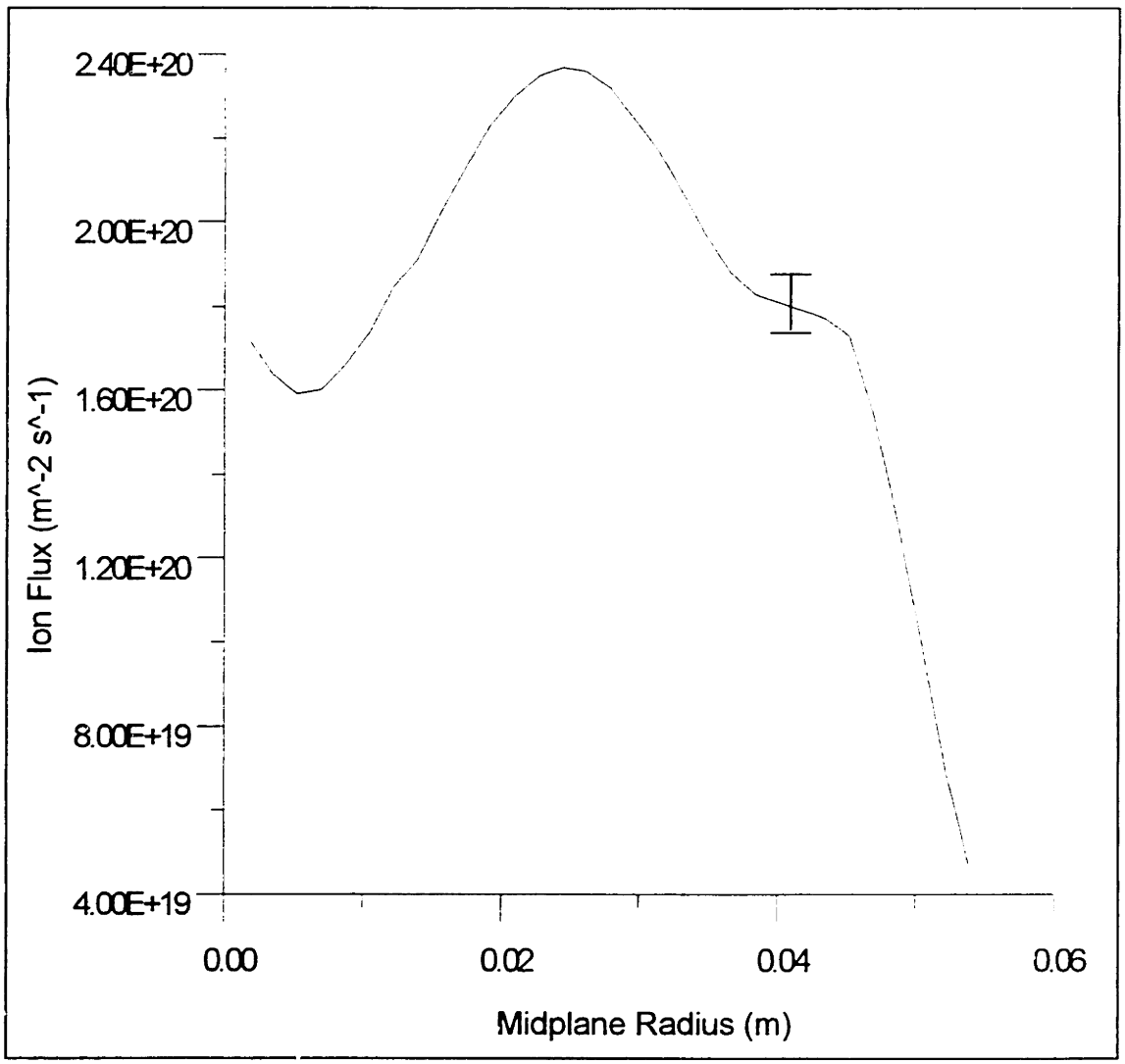

Figure 5-14: Parallel Ion Flux to Wafer Mapped Back to the Midplane 3.0 mTorr, 300 W

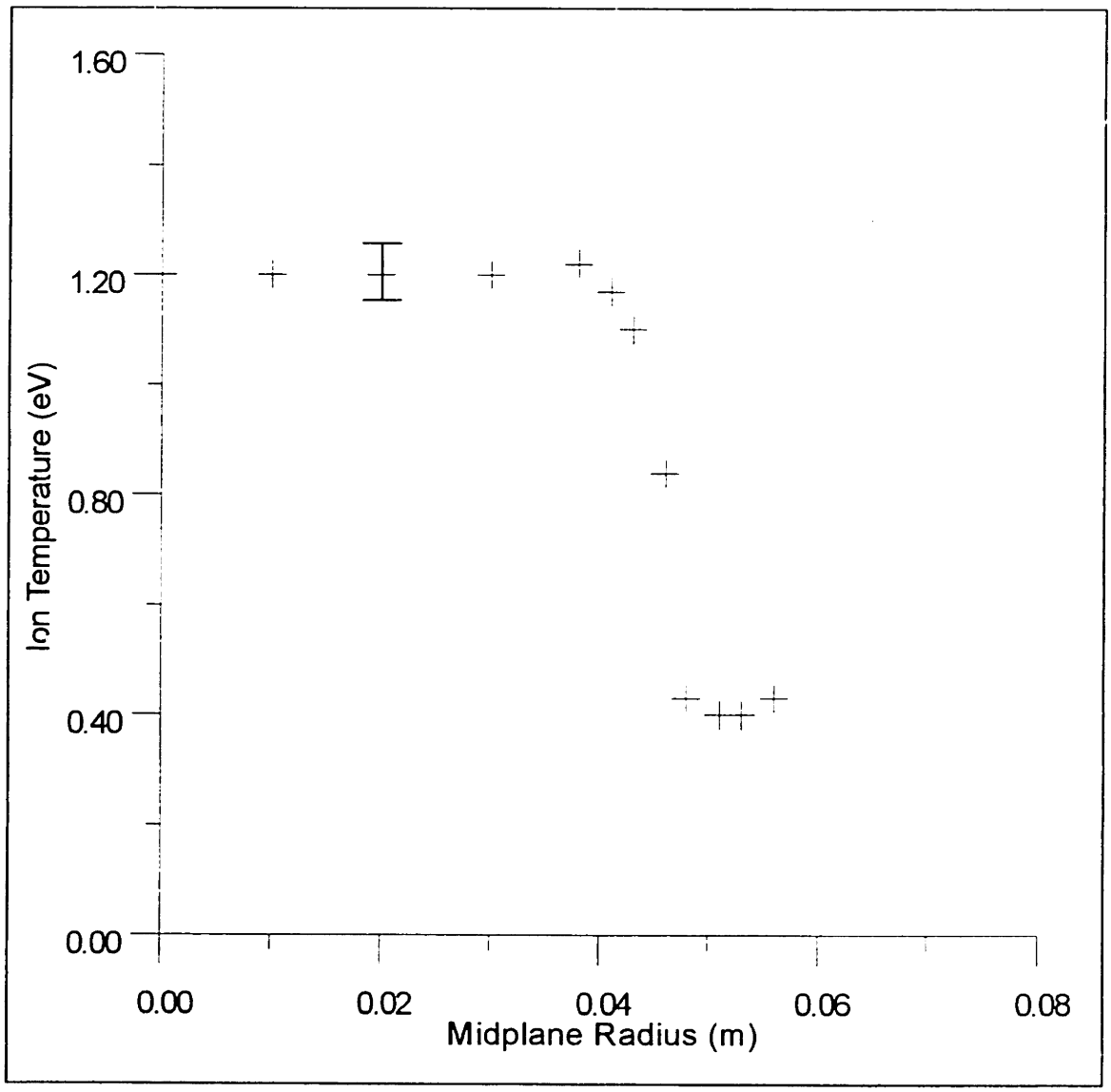

Figure 5-15: Radial Variation of Ion Temperature for 3.0 mTorr, 300W

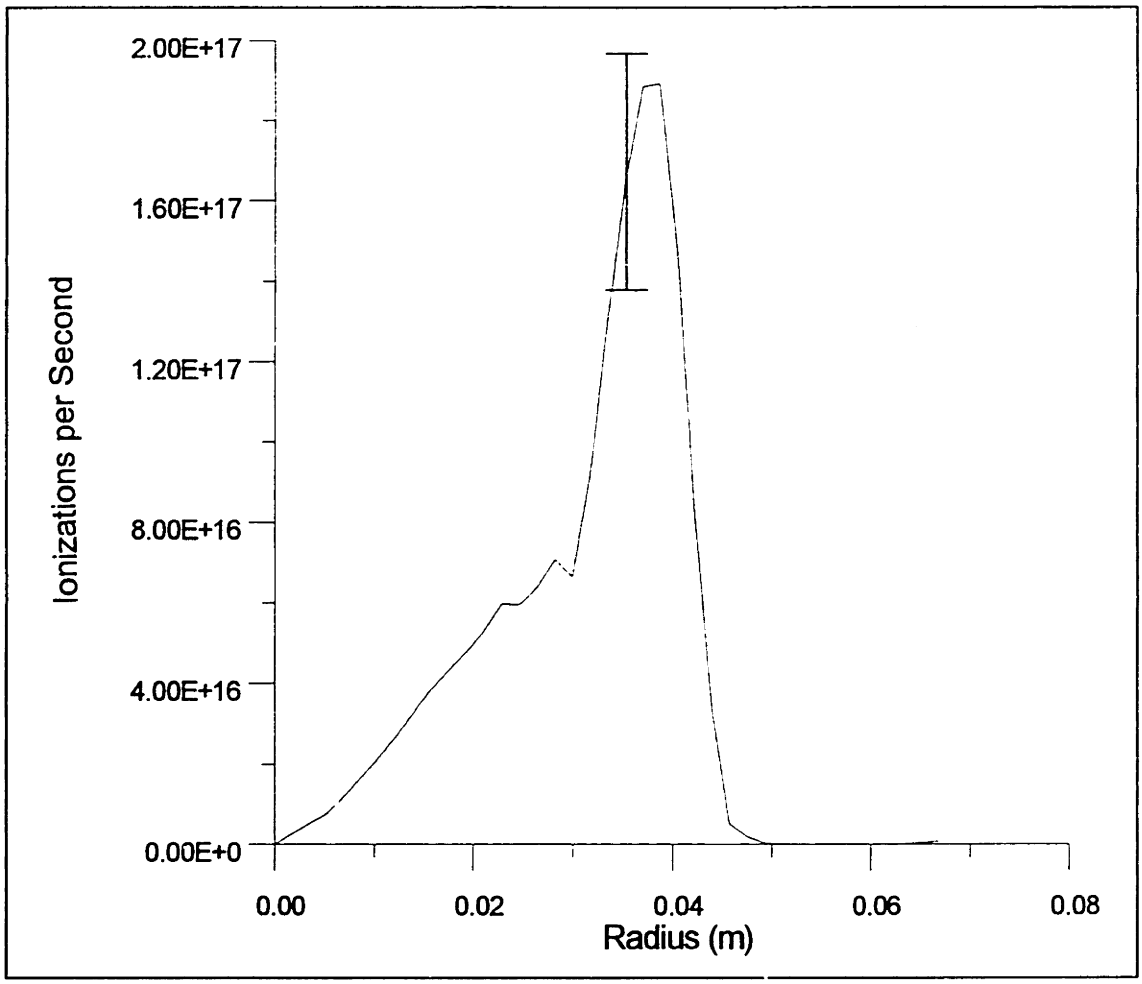

Figure 5-16: Ionizations per Second in a Cylindrical Shell of Width 1.76 mm 3.0 mTorr, 300 W

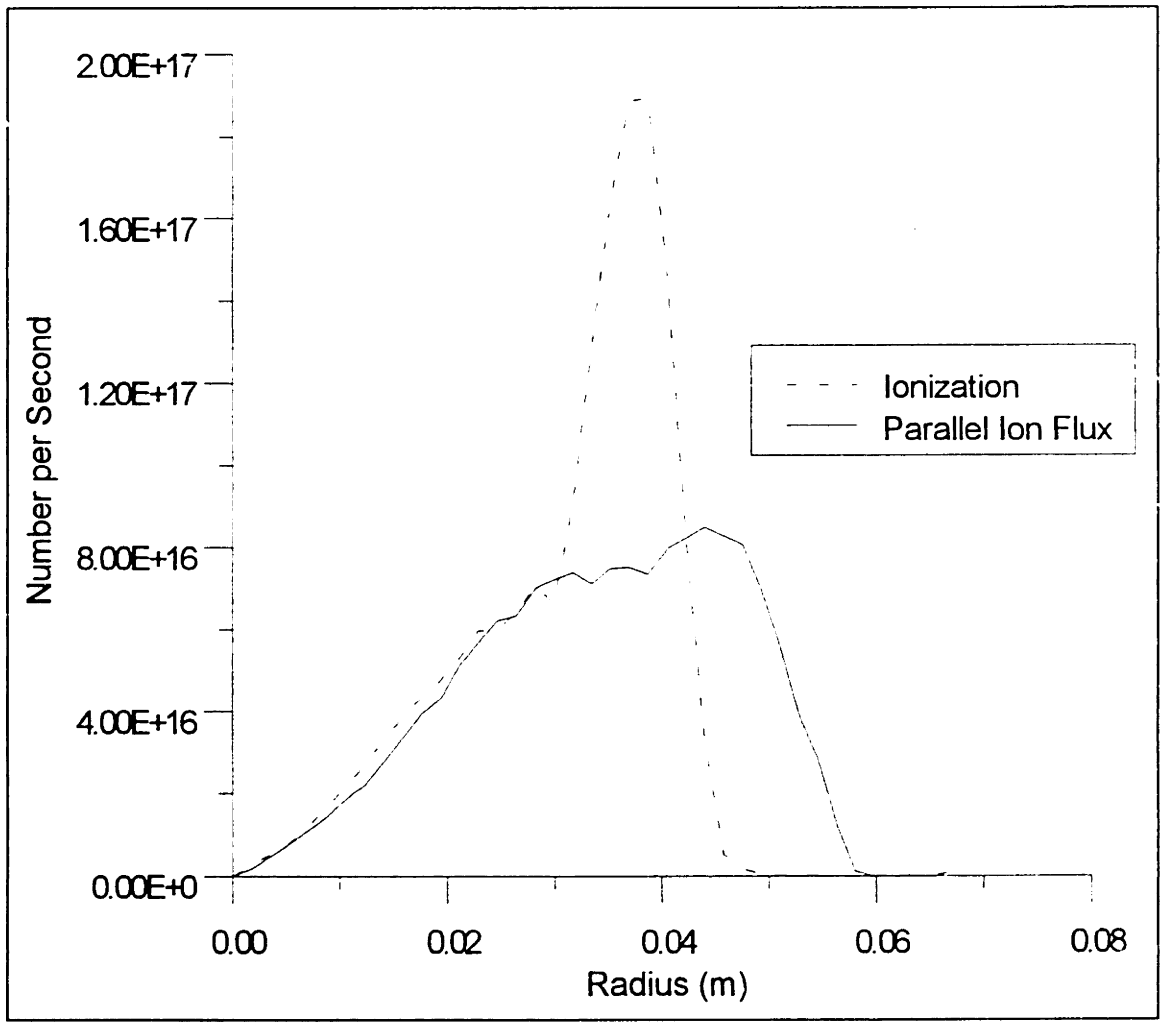

Figure 5-17: Ionizations Within and Parallel Ion Flux Out of a Cylindrical Shell of Width 1.76 mm for 3.0 mTorr and 300 W.

production in this region finds its way into the scrape-off layer. In the interior plasma, production and endloss nearly balance, which confirms observations using Doppler shifted LIF and numerical simulations of ECR discharges [Sadeghi et al. 1991], [Porteous and Graves, 1994] that ions in the core plasma tend to follow magnetic field lines.

Recombination

Figure 5-18 illustrates the magnitude of "shell integrated" recombination under the assumption that bulk electron temperature follows the power law fit (Figure 5-10) to electron temperature decay just outside of ψ_L. Although it constitutes a small correction to the overall particle balance, in the edge region e-e-i recombination dominates parallel ion loss. In addition, the injection of hot electrons into this region will tend to raise the plasma potential there. Thus e-e-i recombination may provide the physical mechanism for creation of the exterior wall of the "potential well" which drives the Kelvin-Helmholtz instability observed in this region.

Neutral Density

As explained in Chapter Four, it was necessary to solve the heat transfer problem for ion heating of neutrals in order to obtain the correct neutral density profiles for calculation of the ionization source and ion-neutral collision frequency. The determination of neutral density and temperature has importance in its own right since the flux of neutrals to the surface being processed has as much, if not more, bearing upon the ultimate uniformity of etching or deposition as does the ion flux.

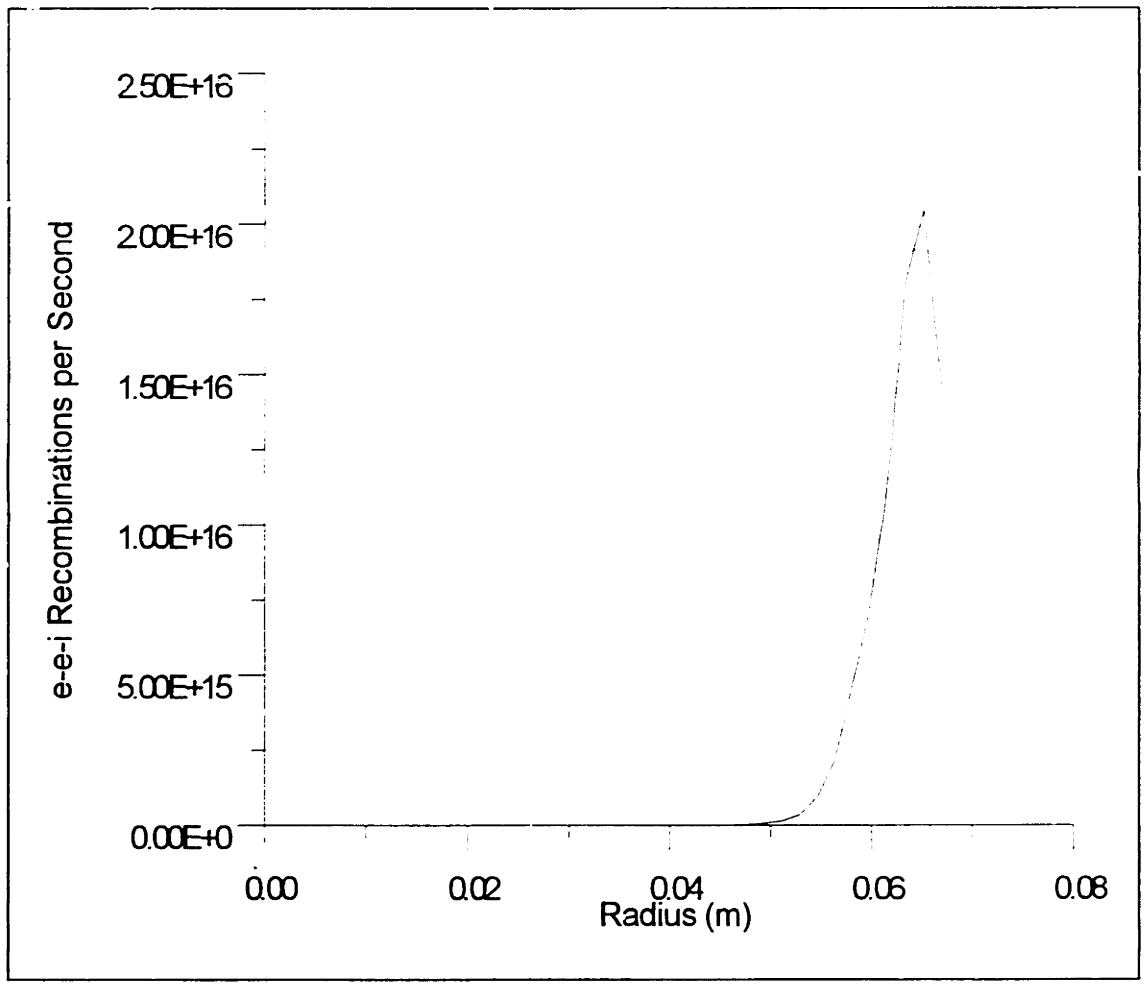

Figure 5-18: Number of e-e-i Recombinations per Second in a Cylindrical Shell of Width 1.76 mm for 3.0 mTorr, 300W

The results of these calculations, shown in Figure 5-19, are in good agreement with the value of 0.068 eV determined by Nakano et al. [Nakano et al., 1991] using Doppler-shifted LIF techniques in the source region of an Ar plasma, with insulating liner. The radial dependence of neutral density is shown in Figure 5-20 with pressure as a parameter. The difference between core and edge temperature increases with neutral pressure, since the volumetric heating of the gas is proportional to number density of neutrals, while the thermal conductivity of dilute gas is essentially independent of gas temperature.

The significant variation of neutral temperature and density across the reactor radius indicates that ion and neutral transport are more integrally coupled than has previously been thought. In fact, this thesis presents the first recognition of such effects known to the author. In the literature, it is generally assumed that neutral density will be uniform across the reactor radius for ionization fractions below 10% (above this value neutral starvation in the plasma core can occur). Since ion temperatures of order 1 eV are the norm for high density sources [Gibson et al., 1994], neutral heating by ions constitutes a generic effect which should be included in all serious attempts to model these sources.

Radial Ion Flux

We now show the experimentally determined radial ion flows in this source. Since both the measured axial ion flux, and the calculated (from equation 3.12) radial electron flux vanish inside of the flux surface which intercepts the liner, the ψ-integrated production (ionization - recombination) is *forced* to balance the ψ-integrated axial ion flux. This constituted a typical

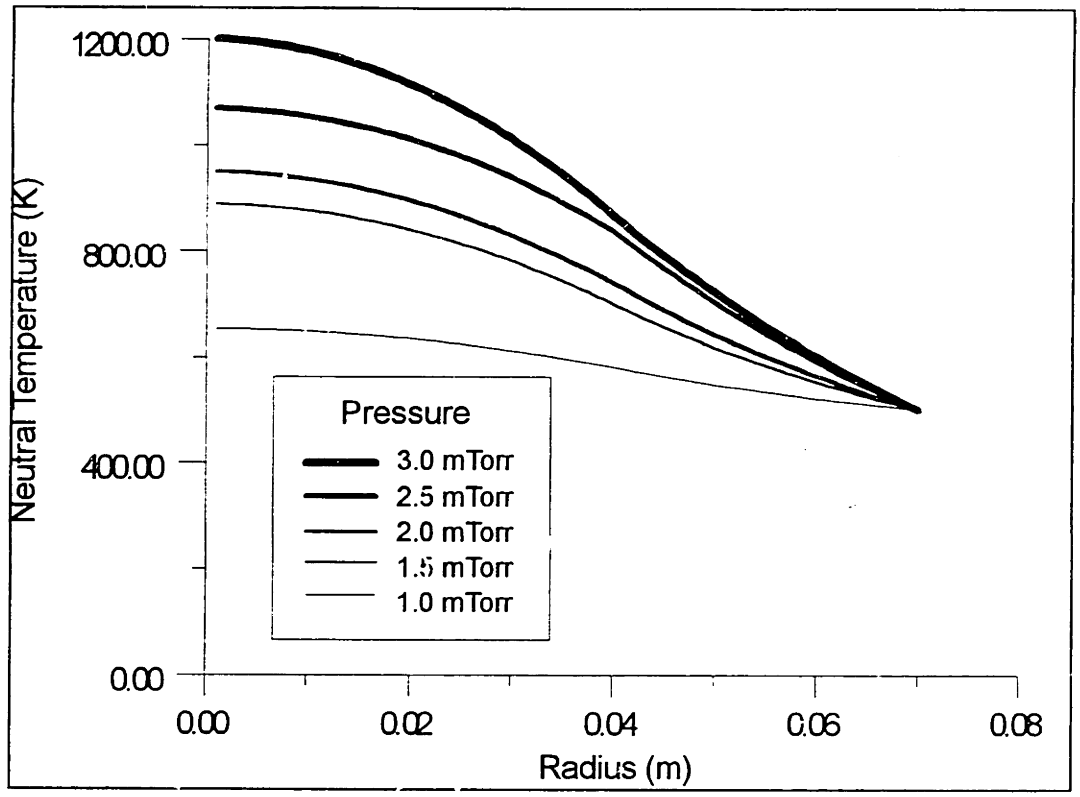

Figure 5-19: Radial Variation of Neutral Temperature due to Ion Heating

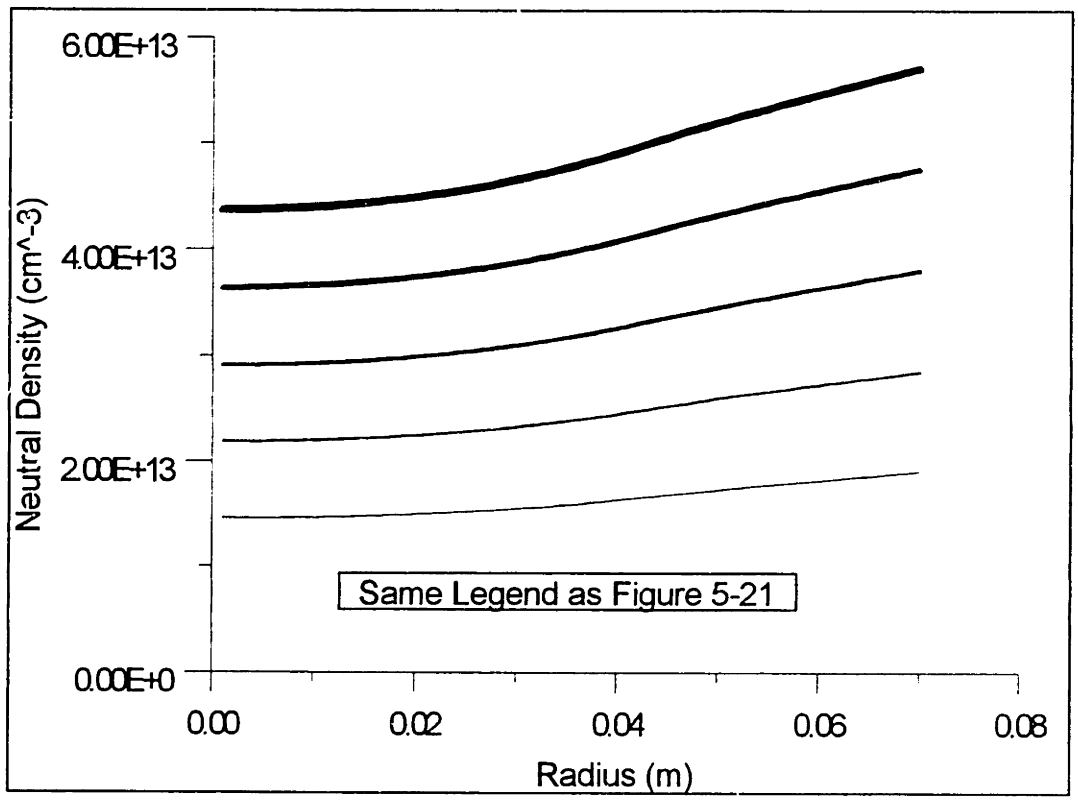

Figure 5-20: Radial Variation of Neutral Density due to Ion Heating

adjustment of 30%. The difference between production and axial flux is, by equation 3.25, the radial flux. In Figure 5-21 the radial ion flux is shown as a function of radius over the range of pressures investigated. In that figure, a positive value corresponds to a radially outward flux, and we see that ion flow is always in the direction of increasing radius, except for the scrape-off layer at 1.0 mTorr. In that specific case, an instability is present on the outer flux surfaces. This will be discussed in the next section. It is clear that the region of maximum radial flux corresponds to that of peak ionization rate. At the potential step, radial ion flux and the radial electron flux calculated from equation 3.12 are always within better than a factor of two of one another.

Discussion

Comparison of equation 3.27 with theory has been rendered difficult by the fact that theoretical values for $D_{\perp i}$ are generally greater than unity for the regimes which have been considered here. Since the typical numerator of equation 3.27 is a factor of 10 less than either of the terms in the denominator ($\Gamma_{\perp i} \leq 5x10^{18}\,m^{-2}s^{-1}$, $\nabla n \approx 5x10^{19}\,m^{-4}$), determination of a diffusion coefficient near the theoretical value requires the balancing of density and potential gradients to within a value small compared to the experimental error. In light of the preponderance of sharp features found in the radial profiles of the plasma parameters, however, one feels compelled to abandon the diffusional picture altogether when attempting to describe radial ion transport in this system.

The crux of these experimental results is that the plasma has employed the long-range nature of the coulomb interaction in order to circumvent behavior which typifies transport controlled by shorter range forces. In Figure

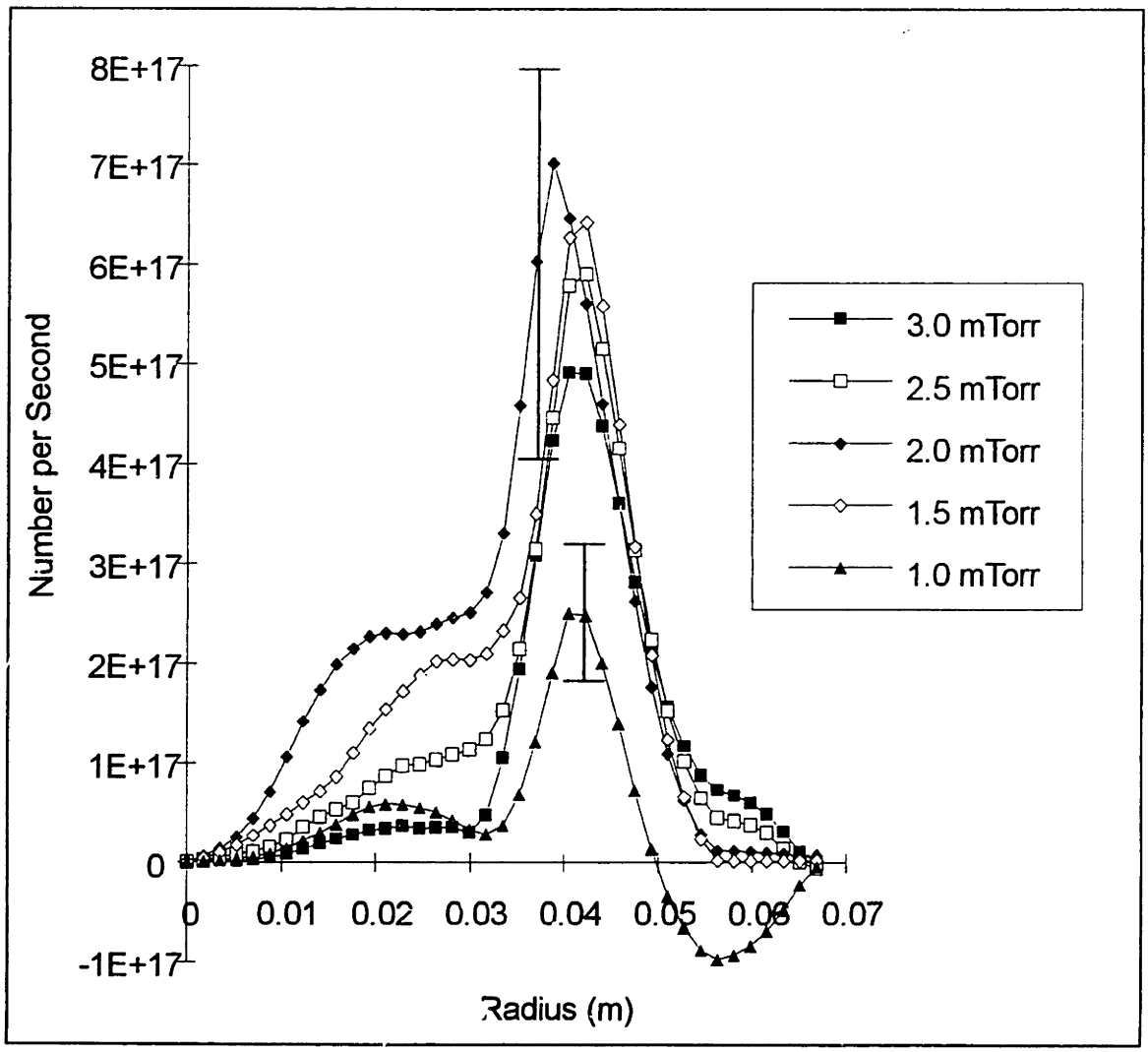

Figure 5-21: Total Radial Ion Flux vs. Radius

5-22, we plot the ratio of total ion flux into the scrape-off layer to the total parallel ion flux between the axis and ψ_L, for a range of neutral pressures. Even with the confining potential step, about 30% of the ions leave the core plasma radially. By plotting the step voltage as a function of pressure, as in Figure 5-23, we can begin to understand the physics of this structure.

Figure 5-24 shows plasma density profiles at several neutral pressures, which have been normalized to unity at the cusp. The lack of a cusp in the 1.0 mTorr case is discussed in the next section. Each of these profiles is remarkably similar at radii greater than that of maximum density, so that the relative contribution of density gradients to radial transport should be the same for all pressures. Ion temperatures change almost discontinuously across the radial voltage barrier at ψ_L (Figure 5-15) from approximately 1 eV in the core to 0.4-0.2 eV in the scrape-off layer, depending upon the pressure. Then, to the core ions, the barrier looks like a true potential step, since it has radial extent smaller than a 1eV gyro-radius (~1cm) and essentially repels all ions with energy less than the step height in Volts. On the other hand, to the cold ions in the edge, the barrier seems like a region of large electric field which sweeps them back into the bulk in a diffusive sense. This observation is essentially an equilibrium population-depopulation statement for the scrape-off layer, with population controlled, to zero order, by the thermal flux of ions over the radial potential barrier, and depopulation determined by diffusive transport driven by the inward radial electric field (and of course axial losses).

This simple model can be written approximately as

$$\left[\frac{n}{4}v_{th}e^{-\frac{\delta\phi}{T_i}}\right]_{bulk} = \left[D_{\perp i}\, n\frac{\nabla\phi}{T_i}\right]_{\psi_l} + \frac{J_{\parallel i}}{2\pi r_{\psi_l} L_p}\Big|_{Scrape\text{-}off} \qquad (5.1)$$

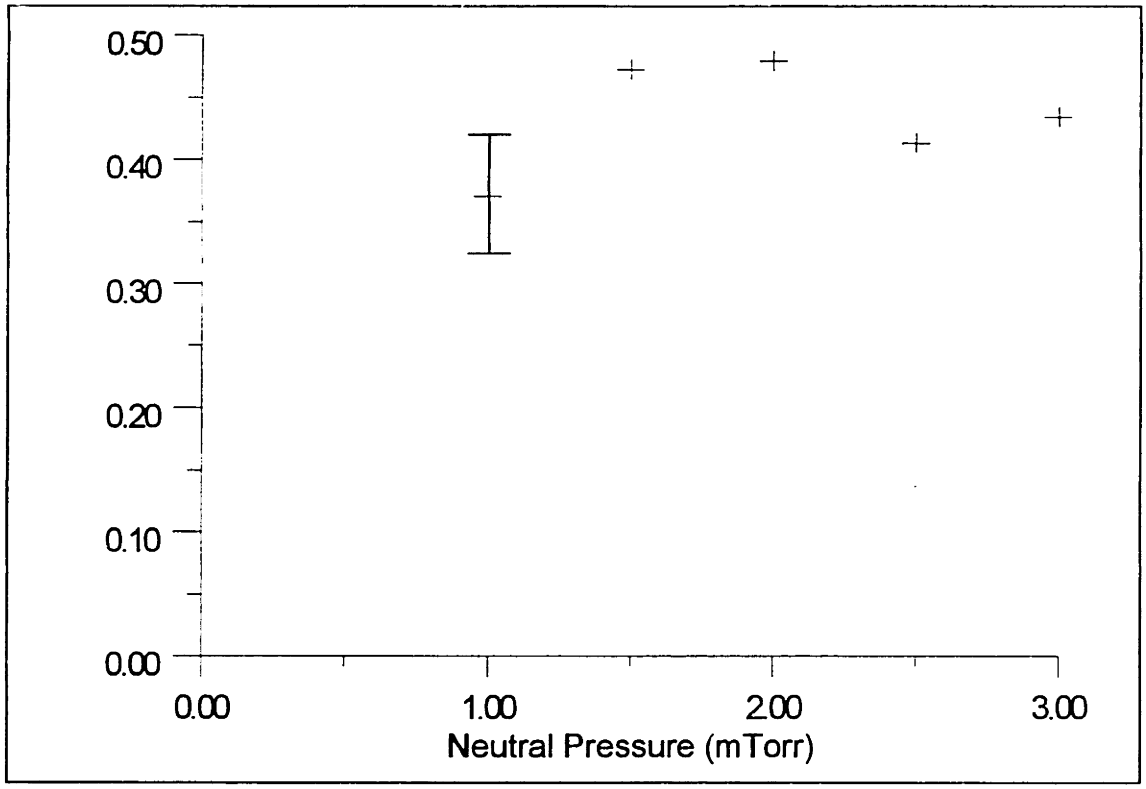

Figure 5-22: Ratio of Radial Flux into Scrape-Off Layer to Axial Flux from the Core Plasma

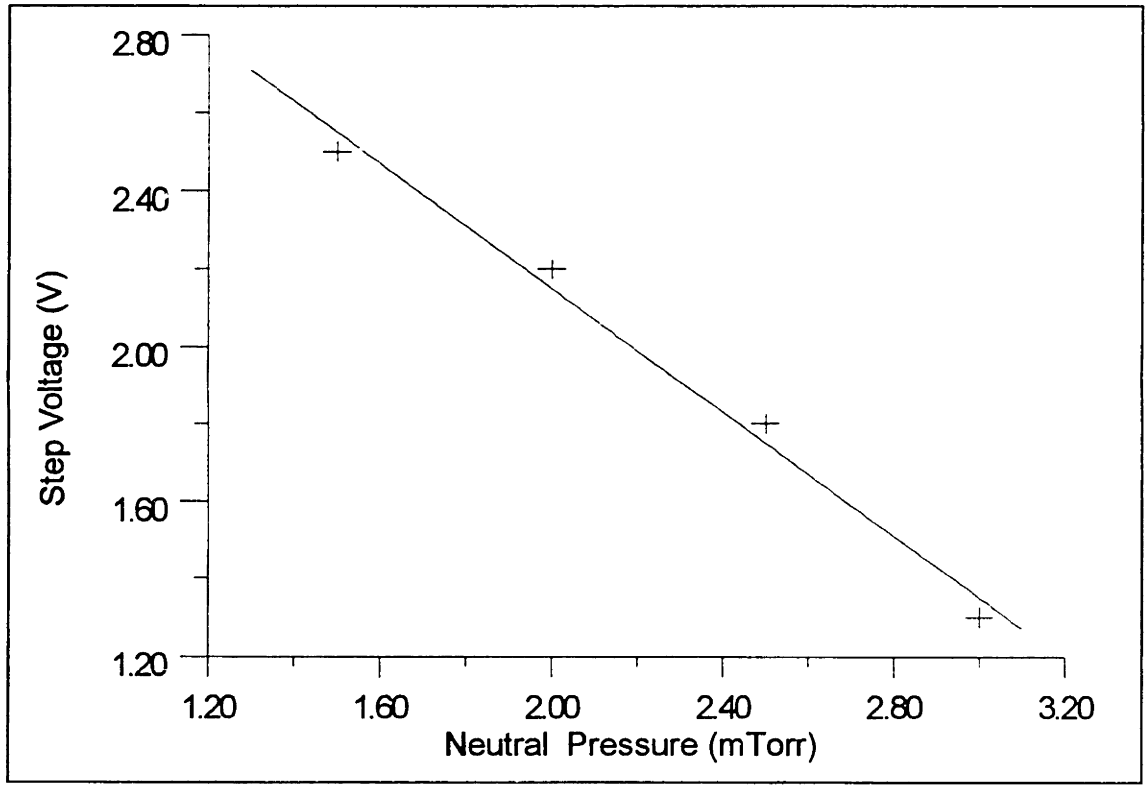

Figure 5-23: Potential Step Voltage versus Pressure

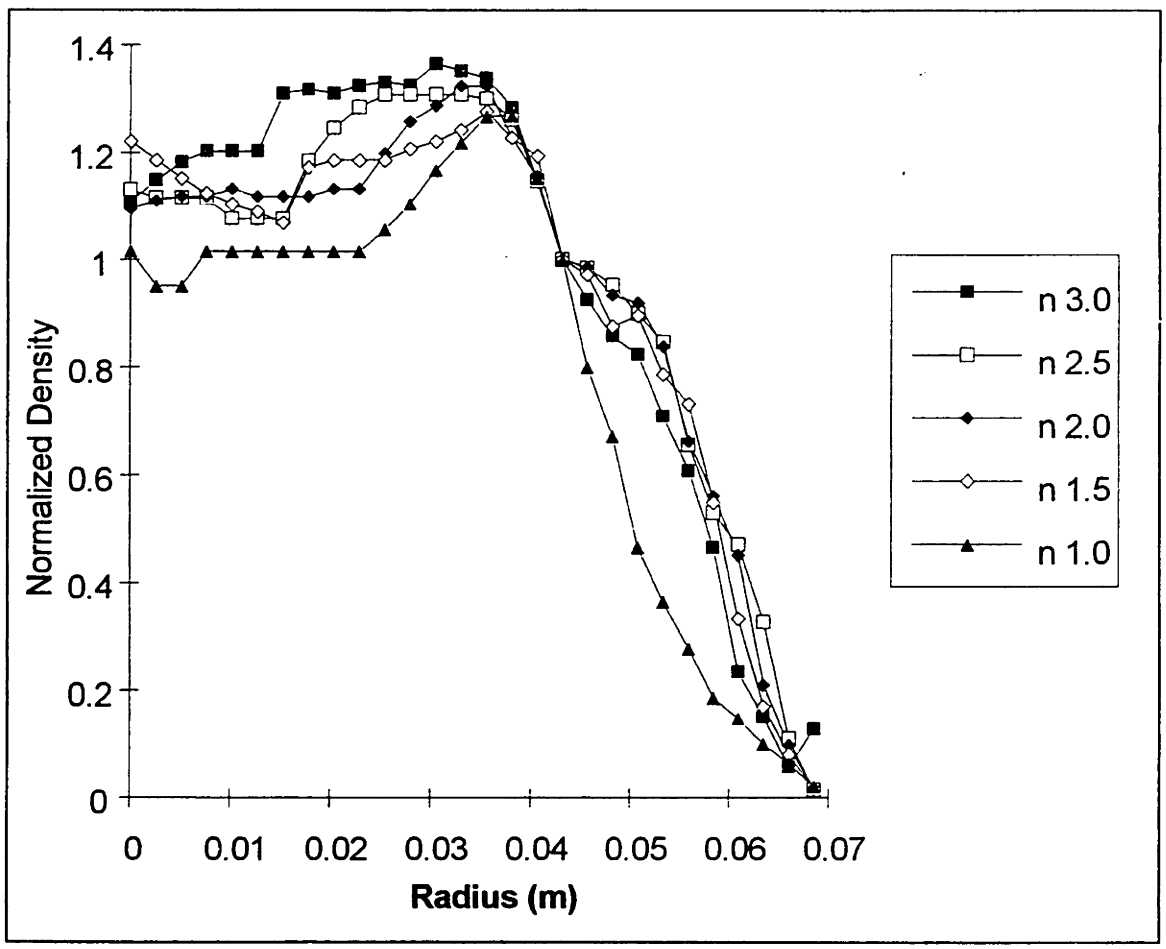

Figure 5-24: Radial Density Profiles Normalized to Unity at the Edge of the Scrape-off Layer

where the LHS is the Boltzmann weighted thermal ion flux to the step, and the RHS has no density gradient term since E dominates here. Obviously, the magnitude of the potential jump will be set by the temperature of the core ions. However, since its value increases almost linearly with *decreasing* pressure (Figure 5-23), we must conclude that the barrier is making up for lost mobility by increasing the electric field. Implicit in this argument is the invariance of both the density gradient length and the radial-to-axial loss ratio (Figure 5-22) with pressure. Using experimental numbers to evaluate the crude expression, equation 5.1, for $D_{i\perp}$ gives values one half to one third that of the theoretical expression.

5.3 Kelvin-Helmholtz Instability

In this section experimental evidence for the existence of the Kelvin-Helmholtz instability described in section 3.3 is presented. Figure 5-25 presents oscilloscope traces of the floating potential on two Langmuir probes located 90° apart in azimuth for conditions of 0.8 mTorr and 300 W microwave power. The direction of propagation is observed to be that of ion diamagnetic drift and the oscillations possess only weak harmonics of the fundamental. The mode is spatially localized near the liner as illustrated in Figure 5-26, which plots a typical variation of fluctuation amplitude as a function of radius. The frequency of the mode does not depend upon radius, but has pressure dependence as shown in Figure 5-27. The pressure dependence derives from the variation in slope of edge density. From Figure 5-28 we see that decreased pressure leads to decreased density gradient length, L_n, at the extreme edge of the plasma which, in turn, increases the ion diamagnetic drift frequency all other things being equal. Edge ion

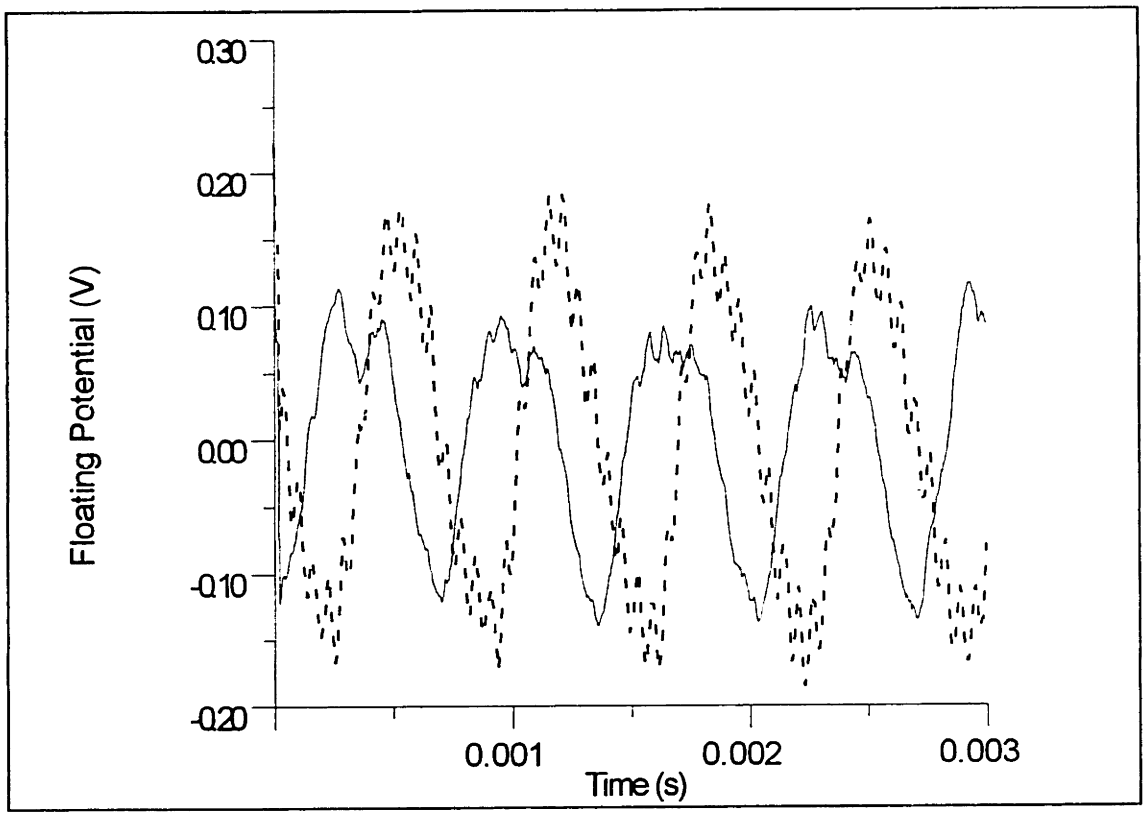

Figure 5-25: Floating Potential on Two Probes Separated by Pi/2 in Azimuth

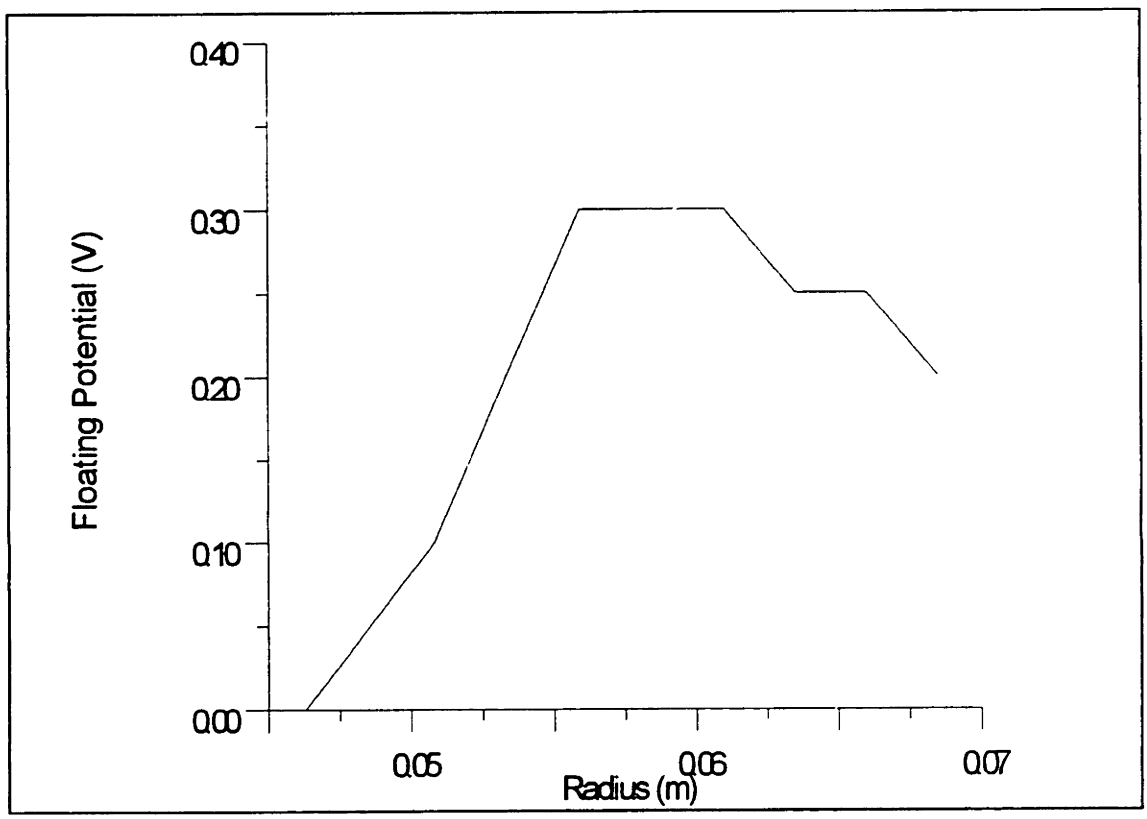

Figure 5-26: Radial Profile of Peak to Peak Fluctuation Level

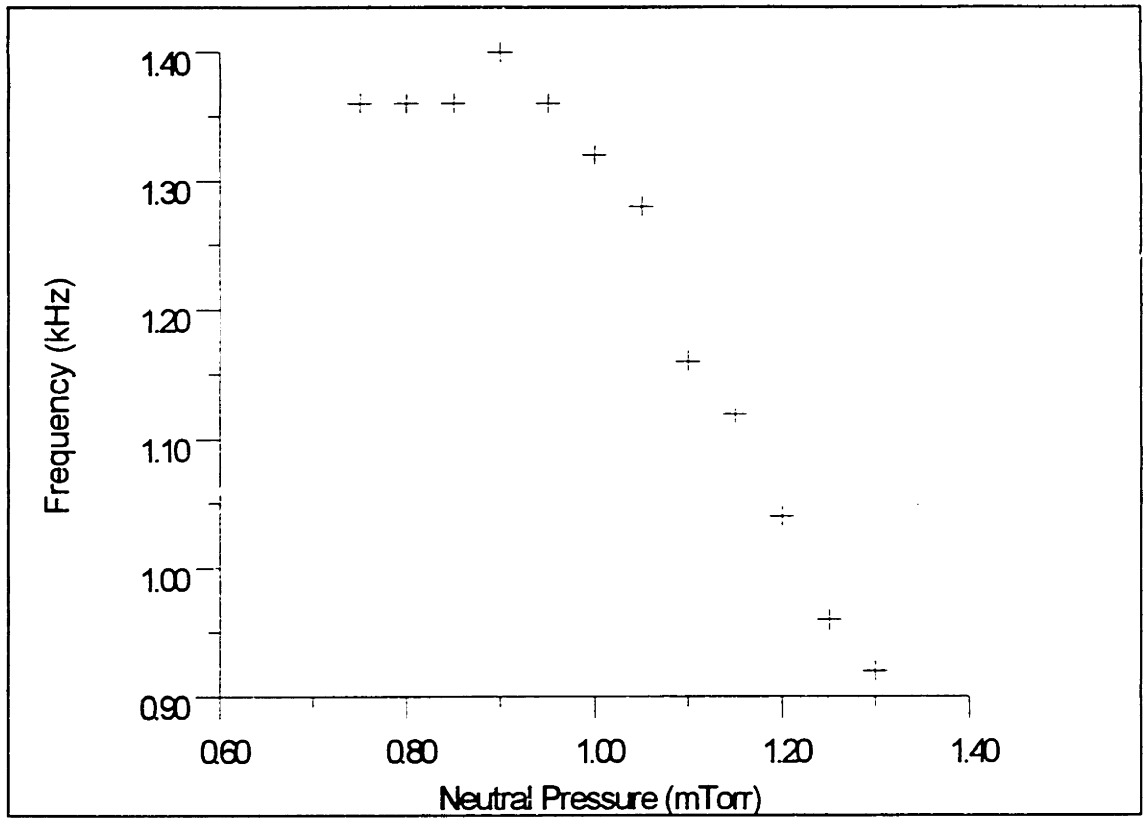

Figure 5-27 Pressure Dependence of Mode Frequency

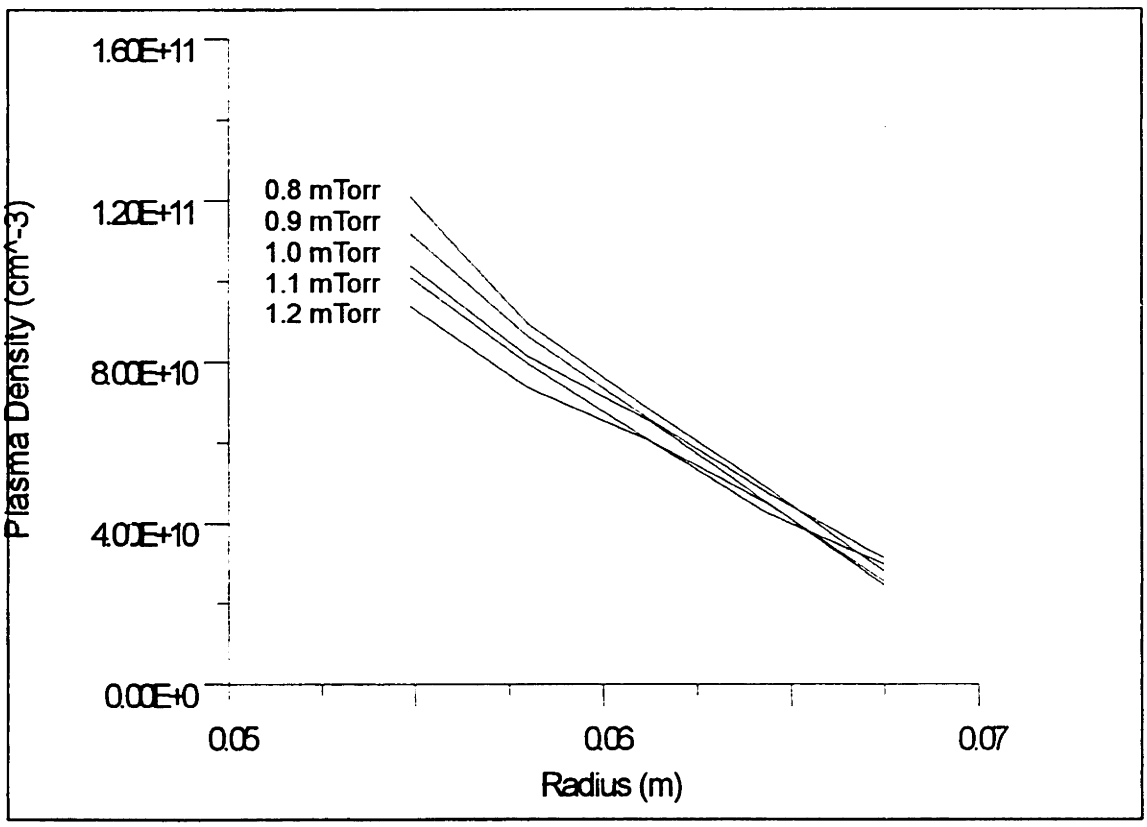

Figure 5-28: Pressure Dependence of Edge Density

temperatures have been measured here as well (Figure 5-29). These measurements were made at a sweep rate of 20 kHz and there should, therefore, exist little or no smearing out of the distribution function by the relatively slowly fluctuating plasma potential (1-2 kHz). One can in fact observe the variation of plasma potential and ion saturation current over a wave period by capturing 10 or 20 sweeps in a single scope trace. Unfortunately, since the electron temperature varies over this region, the net current does not depend upon density alone, and no useful phase information between plasma density and potential can be obtained. At radii where the instability is strongest, some scatter exists in the data, but one can say with confidence that the ion temperatures are known to within 0.1 eV, and further, are uniform to within 25%.

The theoretical analysis of section 3.3 required the existence of a potential trough to bring about instability. Measuring steady state plasma potential presents serious difficulties even in quiescent plasmas. The consistency and apparent accuracy of earlier results, which combined local measurements by floating double Langmuir probe with normalization by RFA, made it plausible that some indication of a trough might be observed. Such a trough occurred repeatably over the pressure range where the instability was observed, and is shown in Figure 5-30. (Its minimum is at approximately r=0.063 m.)

With hard experimental numbers in hand, the expression 3.38 for the instability's real frequency can be evaluated. As a caveat, we note that the linear theory should not be expected to predict precisely the behavior of the fully developed non-linear mode which we actually observe. The curves from Figure 5-29 were used to calculate the density gradient length, L_n at a radius of 0.0625 cm which was taken to be r_o. The width of the assumed Gaussian was

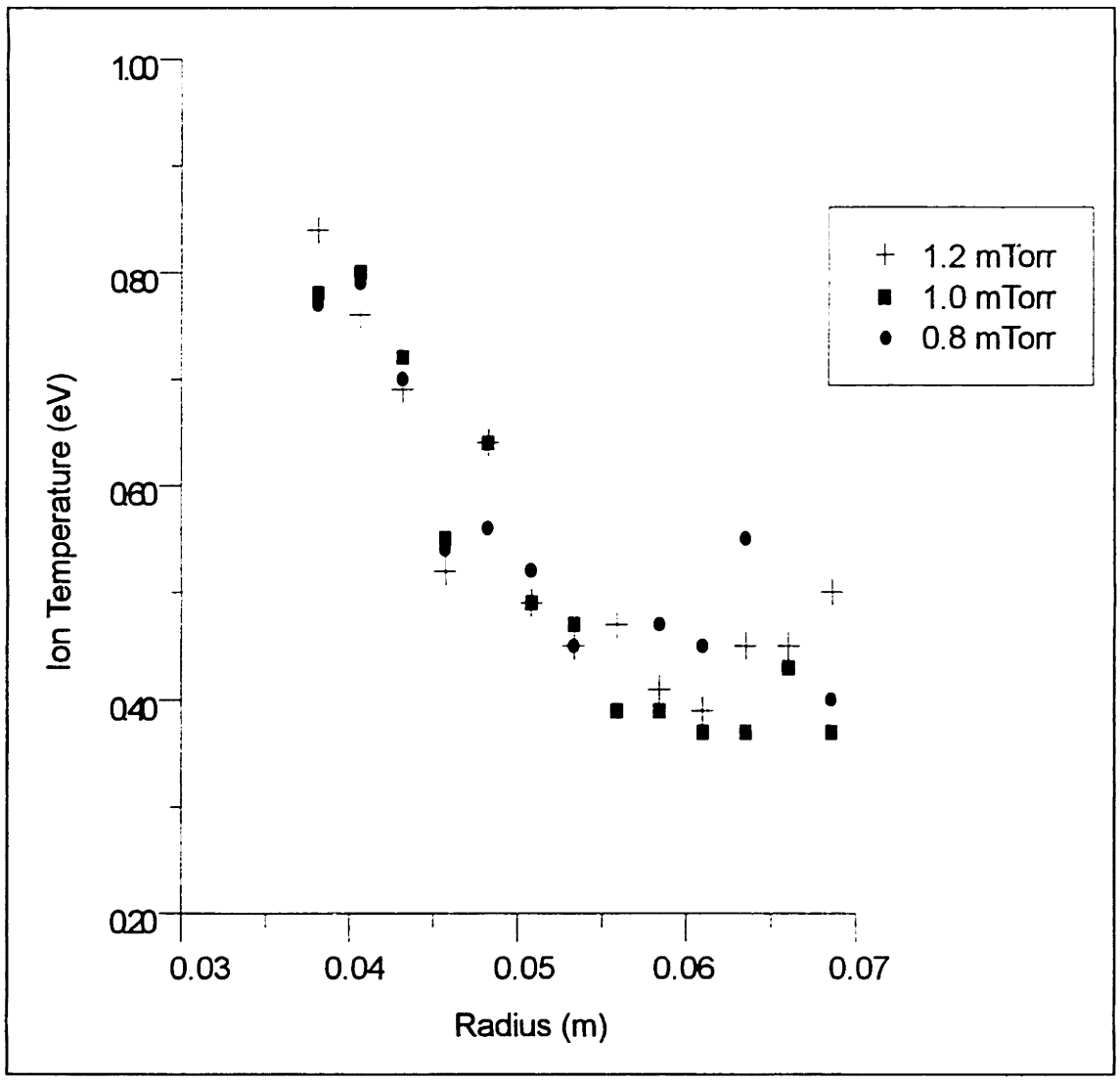

Figure 5-29: Ion Temperatures in the Scrape-off Layer in the Presence of Kelvin-Helmholtz Instability. Data Was Acquired at a 20 kHz Repetition Rate.

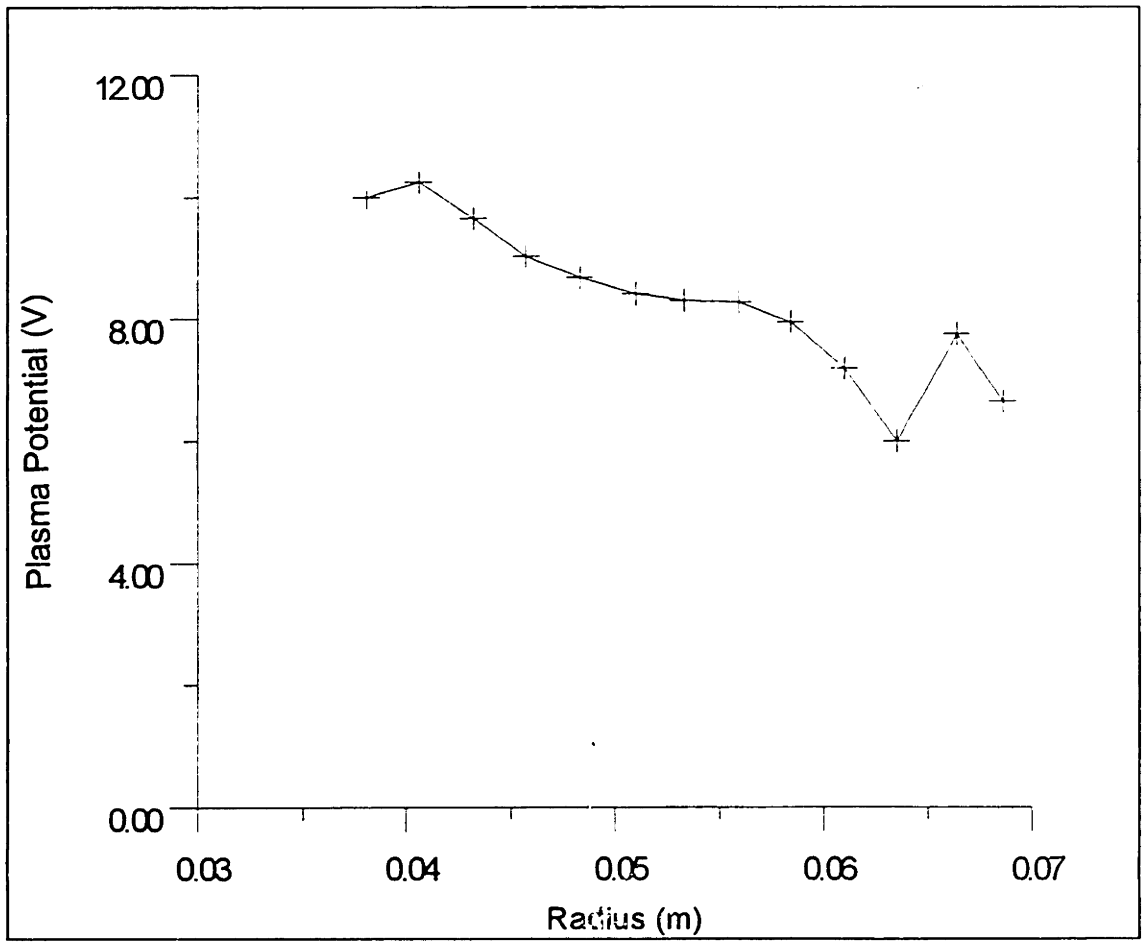

Figure 5-30: Potential Well in the Scrape-off Layer

taken to be the radial extent of the region over which the instability was observed. The values for ω_{di}, κ and δ were then calculated and the expected frequency determined. Figure 5-31 gives the measured and theoretical values of instability frequency along with the calculated ion diamagnetic drift frequency. Trends and absolute values are observed to be in reasonable agreement. Given these experimental values, the well depth necessary to cause instability can be determined as well. The use of equation 3.39 predicts instability for a well depth of just under 1.2 V, which is quite reasonable, and in accord with the data of Figure 5-30.

Data shown in the previous section (Figure 5-12) indicates that a potential dip occurs consistently in the core plasma adjacent to ψ_L. It is therefore reasonable to ask why the instability should not occur there as well. A calculation similar to the one just given for well depth necessary to cause instability was performed for the 1.0 mTorr case which had the deepest potential dip (L_n was nearly the same for all cases). It showed that the mode should be marginally stable (i.e. the well depth less than, but within error bars of, the critical potential). It is also worth noting that the ion larmor radius here is nearly twice that of the ions at the extreme plasma edge, and of comparable dimension to the radial extent of the well. One might therefore expect mitigated effective electric field shear due to finite larmor radius effects, and a corresponding enhancement of the stability threshold.

The qualitative effect of the Kelvin-Helmholtz instability upon the radial transport of ions across ψ_L can be determined by comparing the radial profiles of electron temperature and plasma density in the presence and absence of the instability. Figure 5.24 shows plasma density profiles which have been normalized to unity at ψ_L. The concave down curvature of the profile for flux surfaces immediately exterior to ψ_L has been observed for every

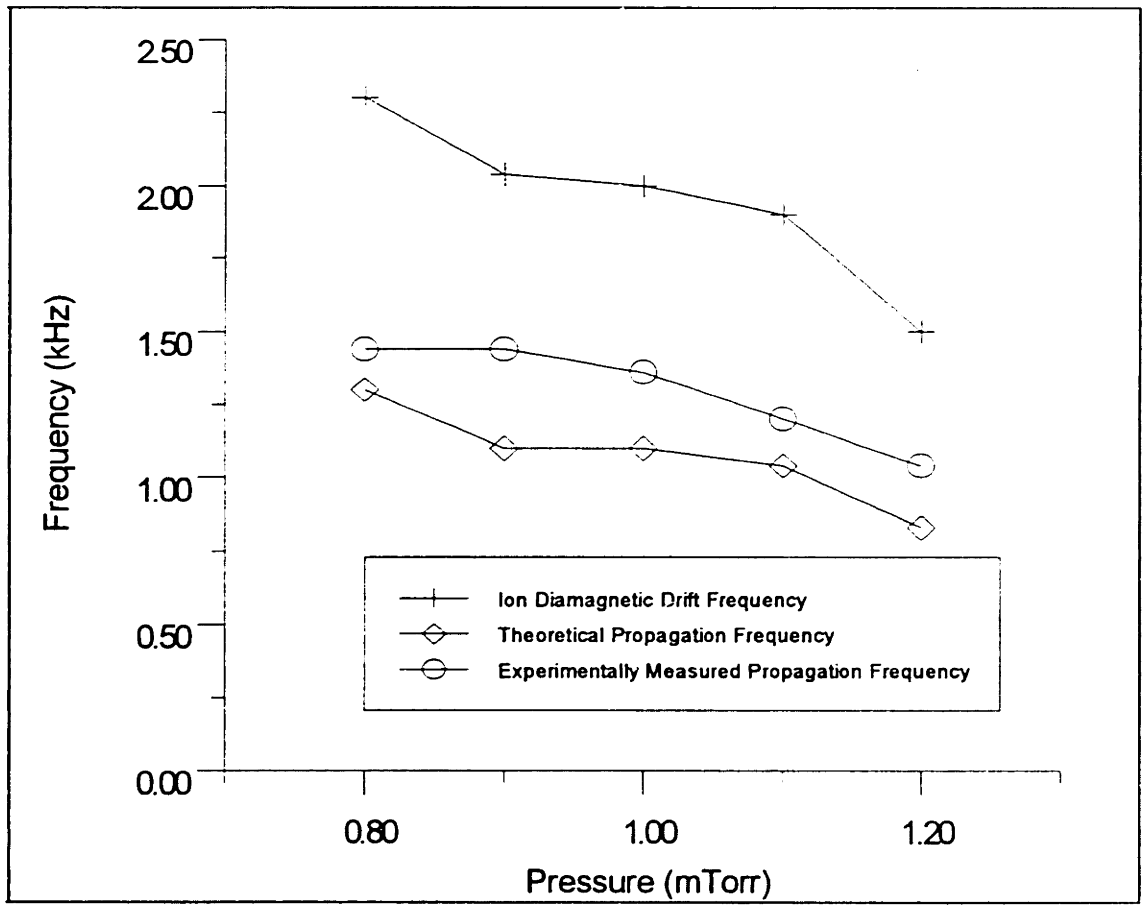

Figure 5-31: Theoretical and Experimental Values for Kelvin-Helmholtz Instability Frequency

case, independent of magnetic field topology or macroscopic (high or low density) mode, where the Kelvin-Helmholtz mode was absent. Conversely, whenever the mode was present, concave up profiles were observed in that range of flux surfaces. We also found that the electron temperature in the scrape-off layer adjacent to ψ_L is always enhanced by the presence of the fluctuations. These qualitative features can be explained by considering the motion of the plasma fluid elements under influence of the instability. The azimuthal electric field of the mode causes radial drift due to ExB motion, of approximate amplitude δr given by

$$\delta r = \frac{V_p}{r_o B f} \tag{5.2}$$

where V_p is the peak to peak potential of the mode, r_o is the radius at which the mode occurs, and f is the mode frequency in Hertz (the units of 5.2 are MKS). Thus, plasma within δr of ψ_L will convect into the plasma core where heating due to the high parallel electron thermal conductivity occurs. For typical values (V_p = 0.1 V, r_o = 6 cm, and f = 1.5 kHz), excursions on the order of 1 cm are expected.

The effect of the enhanced electron heating upon radial density occurs from axial losses which increase exponentially (i.e. by a Boltzmann factor) with electron temperature. The loss term, F, in equation 3.25 must then increase if the plasma is to remain quasi-neutral, resulting in lower densities in the region of elevated temperature.

Chapter Six

Conclusions

6.1 Summary of Results

In Chapter Three, the limiting cases of ambipolar and Simon diffusion were defined, and it is appropriate at this point to ask whether the experimentally determined radial ion flux corresponds to one or the other of these classifications. To estimate the expected magnitude of the transport we can assume a density of 1.5×10^{18} m^{-3} and a gradient length equal to the liner radius (~0.07 m) which gives $\nabla n \sim 2 \times 10^{19}$. Using this in equation 3.12 for the perpendicular electron flux gives 8×10^{17} $m^2 s^{-1}$. The radial ion flux is plotted in Figure 6-1 for several neutral pressures. The flux peaks near ψ_L with a typical value of 6×10^{18}. Radial transport in the interior plasma increases with decreasing pressure. At 3 mTorr, the core transport is nearly a factor of 10 less than that at the peak and is approximately the electron radial flux calculated above, while for the lower pressures, it is roughly half of the peak flux. An estimate of the magnitude of ion diffusion can be made by dividing the typical peak ion flux by ∇n, above, which gives 0.3 $m^2 s^{-1}$. Consulting Figure 3-1 shows that this value of $D_{i\perp}$ corresponds to ion temperatures in the 0.1-0.3 eV range.

The above estimates show that global radial ion transport is bounded from below by that for the electrons, and from above by the value for the cold edge ions, which is an eminently reasonable result. The hot core ions have a diffusion coefficient five to ten times higher than those in the scrape-off layer,

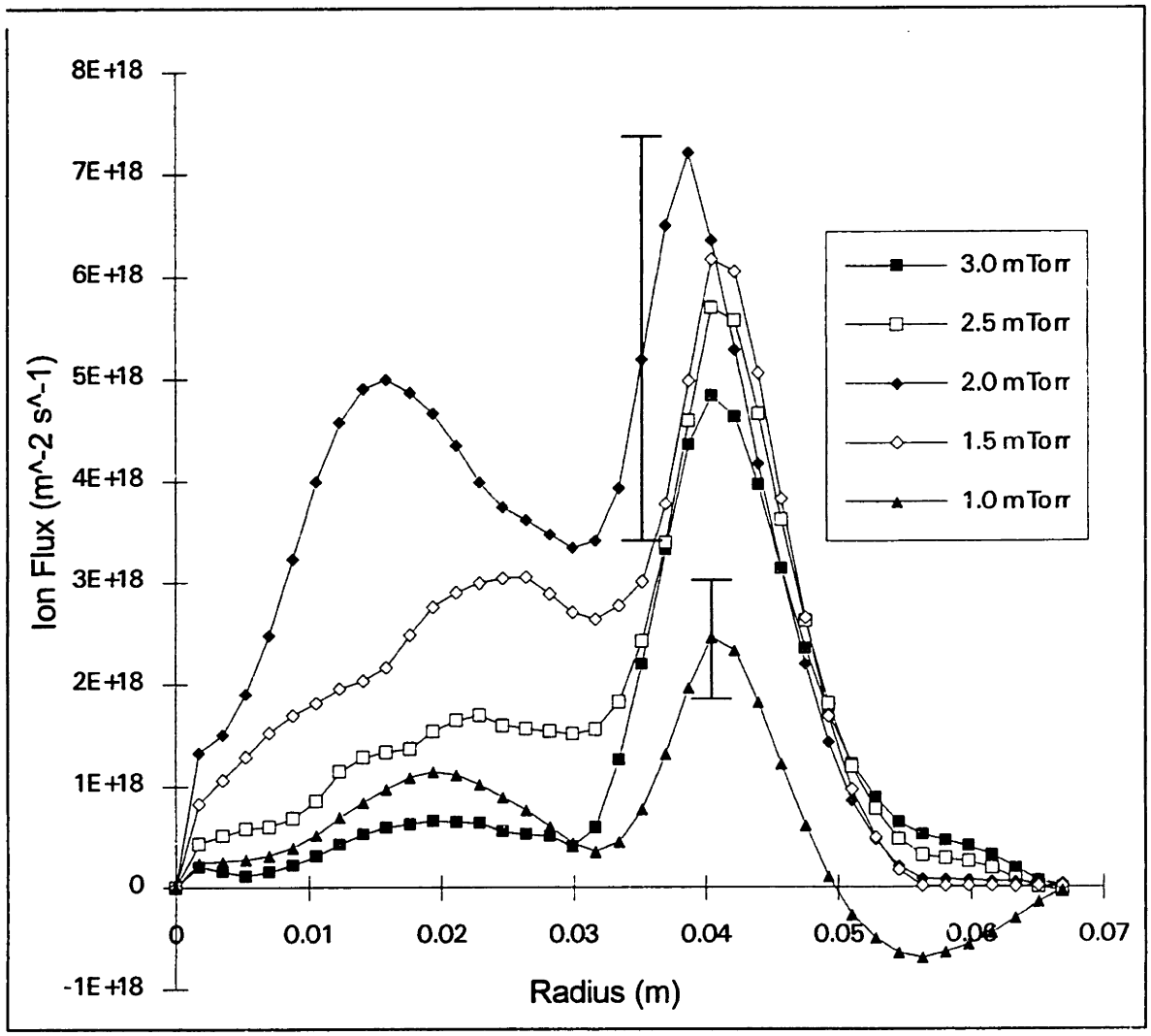

Figure 6-1: Radial Ion Flux as a Function of Radius
for 300 W Microwave Power

and therefore radial electric fields must be set up to reduce cross-field ion transport in the core. Ion temperature across ψ_L changes in a manner practically discontinuous on the scale of a hot ion larmor radius, and it is the resultant precipitous change in perpendicular ion diffusion coefficient which necessitates the formation of a potential step in that region. This structure dominates radial ion transport in the system and is not well characterized in terms of a diffusion equation since it possesses strong shear over length scales of a random walk step size. These assertions are supported by the appearance of qualitatively similar features in a system which was configured identically except that it possessed a *conducting* radial wall [Lane, et al. 1990].

Transport in this system can then, in the global sense, vary continuously between the limits of ambipolar diffusion and Simon diffusion, depending upon both the external experimental parameters and the magnetic flux surface at which the radial ion flux is evaluated. The caveat here is that the local flux may bear complicated dependence (i.e. does not obey a diffusion equation), or no apparent dependence at all, on the local density and potential gradients, and therefore $D_{i\perp}(\psi)$ represents an essentially inappropriate quantity. Furthermore, for neutral pressures below 2 mTorr, steady state transport does not necessarily obtain. We observed in the course of this work that the presence of strong electric field shear (set up by the complicated requirements of particle transport) can lead to time periodic and/or linearly unstable solutions of the ion fluid equations.

Although the usual drift waves (propagating in the electron diamagnetic direction) were experimentally noted, they always occurred at neutral pressures below those practical for plasma processing. On the other hand, low frequency modes propagating at large amplitude in the ion diamagnetic direction appeared at pressures commensurate with the usual processing conditions for

ECR sources. This instability had a significant effect upon both particle and energy transport across magnetic field lines. The sharp temperature gradients in the vicinity of ψ_L were mitigated by the transport of fluid elements from the cold edge into the hot plasma core under influence of the oscillating azimuthal electric field. The instability also altered the radial density gradient and the ion flux.

Although comparison between theory and experiment was made in the edge region at relatively low neutral pressure, isolated instances of a qualitatively similar instability occurred at higher neutral pressure and in the core plasma for both magnetic mirror and magnetic beach configurations. The presence of such modes in a processing plasma is not necessarily undesirable. Even at amplitudes of several volts, these modes pose no danger to the substrate from charging or bombardment energy, and instead serve to smooth radial inhomogeneities in a time averaged sense, as processing times are on the order of seconds, at minimum.

The recognition of the interdependence of neutral and ion transport for plasmas of ionization fraction below 5% constitutes a surprising, and a very important result of this thesis. Ion flux uniformity has always been assumed to determine the macroscopic etch uniformity in semiconductor applications (as long as gas flow in the reactor has been correctly engineered). However, the solution to equation 4.2 for neutral temperature is *not* constant, and is in fact simply parabolic, for constant right hand side (uniform ion density and temperature). Such an effect may well explain what appeared to be anomalous results from our own research [Gibson, et al., 1994]. In these experiments ion flux uniformity and energy spread were determined for two commercial plasma etchers. In each case the temperatures were essentially uniform and approximately 1 eV, while the ion flux to the wafer peaked slightly on axis (10-

20%). When etch rates were measured, however, they were found to proceed more slowly at the wafer center by approximately 5%. Ion heating of the neutrals could well account for the observed effect.

6.2 Future Work

The key experimental question which has been left unanswered by this thesis concerns the relatively high ion temperatures which have been measured. No strong turbulence was reflected in floating potential fluctuations under the conditions where data was acquired, which rules out the often invoked turbulent heating mechanism. The possibility of super-elastic collisions with metastables was also considered, but this does not correlate with the sharp ion temperature gradient at ψ_L since radially, the metastable density is expected to be fairly uniform. The other mechanism which has historically been invoked to explain elevated ion temperatures is radial electric fields; however, in our system, since the radial field ostensibly serves to confine the ions, such an assertion seems to beg the question. A careful, spatially resolved study using a non-invasive technique such as Doppler shifted LIF might provide an answer to this puzzle. The experimental determination of radial variation in neutral temperature can also be accomplished by the LIF technique.

Since radial electric fields have been determined to play a central role in the ion transport, experiments similar to those in this thesis, performed with a biased ring (or rings) around the wafer might shed further light on transport mechanisms, as well as provide a means for tailoring the uniformity of etch or deposition. The bias on the rings could be d.c. or modulated (with or without offset). The rings could also be used to establish conditions under which the Kelvin-Helmholtz instability observed in this thesis work could be more

systematically studied, especially in regard to its interconnection with particle and energy transport.

Appendix A

Instrumentation

This appendix contains schematics and brief descriptions of several specialized electronic circuits which were designed and constructed in the course of this work. Although other pieces of electronic equipment were fabricated for use in these experiments, we include only those which are of non-trivial design, or which are crucial to the accuracy of the experiments. The first circuit to be discussed is a high-bandwidth, floating ammeter for use with the Retarding Field Ion Energy Analyzer (RFA) diagnostic. The second reads off current and voltage from the Floating Double Langmuir Probe (FDP) diagnostic for the generation of the I-V characteristic. In each case an input signal (voltage) is supplied to the circuit. The source of the signal is an Hewlett Packard 3312 A function generator. However, since in both circuits the function generator, used alone, would be driving significant capacitive loads, a simple follower composed of an Apex PA-08 power op-amp is used as a power amplifier and placed between the HP 3312 A and the circuit input. The PA-08 can source up to 150 mA of current, is highly linear, and possesses a gain-bandwidth product of 5 MHz at a frequency of 1 MHz. This configuration insures that input signal quality is unaffected by loading from the circuits.

A schematic for the high bandwidth floating current amplifier used with the RFA diagnostic appears in Figure A-1. Op amp Q1 is configured as a current to voltage converter. The sweep voltage (usually a 10 kHz triangle) drives the non-inverting input of Q1 and the inverting input, which is

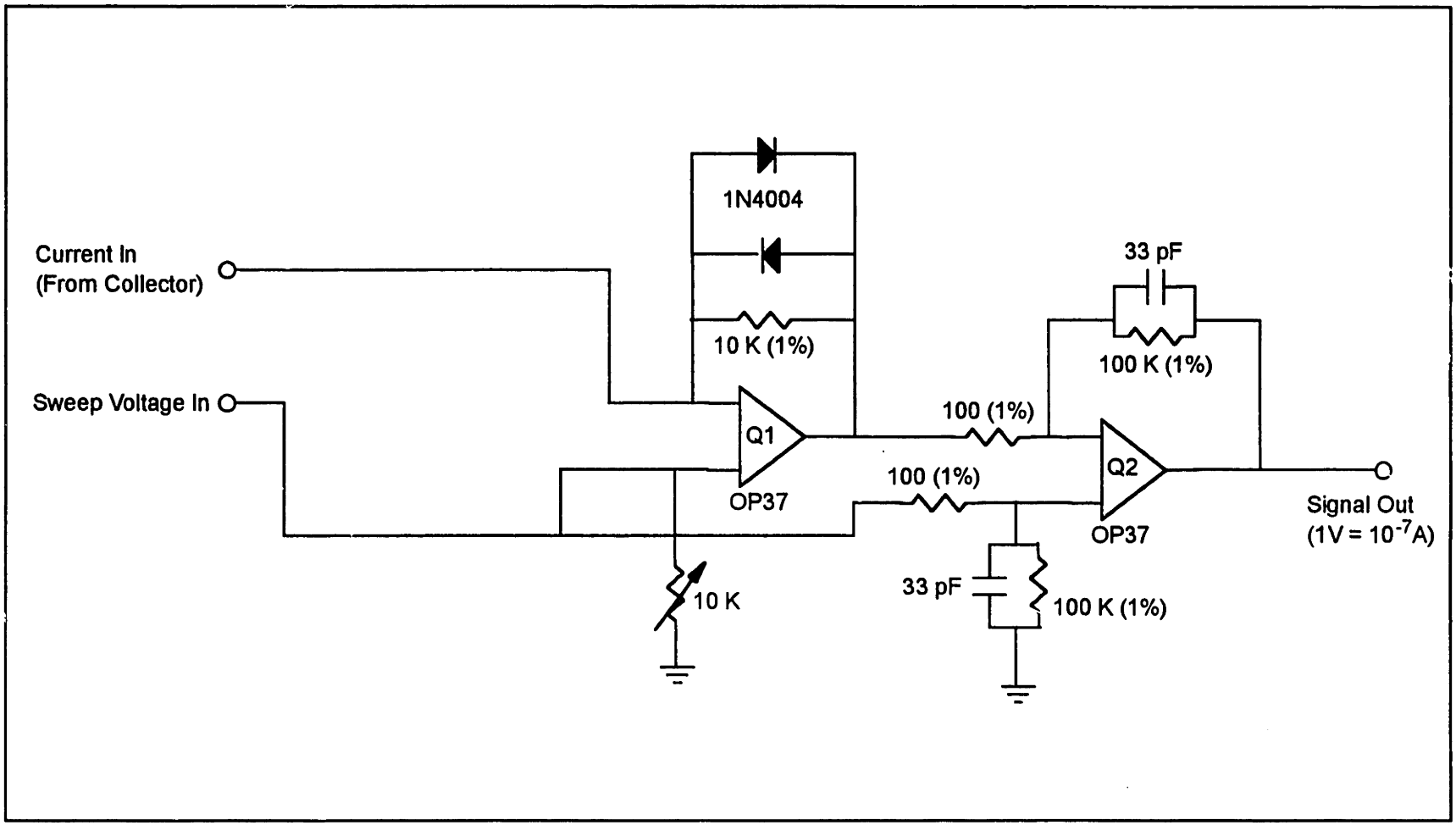

Figure A-1: High Bandwidth Floating Current Amplifier for Ion Energy Analyzer

Gain: 0.1 microAmperes / Volt
Bandwidth: ~100 KHz
Sensitivity: < 10 nA

All Resistors are Metal Film
Q1 & Q2 are Supply Bypassed with 10 uF Ceramic
Q1 Resides on a Driven Shield

connected to the collector of the RFA, follows it. The linearity of the current to voltage sub-circuit is insured by the 10 kΩ trimmer which is adjusted to balance the input impedance of the inputs to Q1. A pair of diodes in opposition appear across the 10 kΩ feedback resistor of Q1. The diodes prevent latchup of Q1. Since both high bandwidth and high current gain are desired of the Q1 sub-circuit, parallel capacitance in the feedback loop must be kept to a minimum. The sub-circuit is thus rendered sensitive to high frequency noise which can lead to latch-up. The output of Q1 is then differentially amplified with respect to the sweep voltage by the gain 100 sub-circuit of Q2 which provides an output level of 10V/μA, with respect to instrument ground.

The OP-37 is a low offset current, precision, high speed op-amp. Its gain-bandwidth product is 63 MHz, which allows the use of only two aggressive gain stages in the circuit. The OP-37 has a common-mode rejection ratio of 126 dB over a +/- 11 V input range which corresponds to less than +/- 1 mV ripple on the output of Q2 at full swing operation. The input offset current is 10 nA, typical, and provides the bound on circuit sensitivity. At sweep frequencies above 20 kHz, the linearity of the current to voltage circuit (Q1) begins to degrade, apparently due to op-amp input capacitance.

The current and voltage measurement circuit for the FDP is shown in Figure A-2. Because a much lower sweep rate was utilized for this diagnostic, the frequency domain behavior of this circuit was much less critical than that for the RFA. As a result we were at leisure to use the uA747 which is a garden-variety dual instrumentation op amp. The overall operation of this circuit was outlined in Chapter 2 and will not be repeated here. The coupling transformer is a Stancor 162-007 rated for use at 60 Hz. Its output was observed to remain quite linear well into the hundreds of Hertz, however. Current to

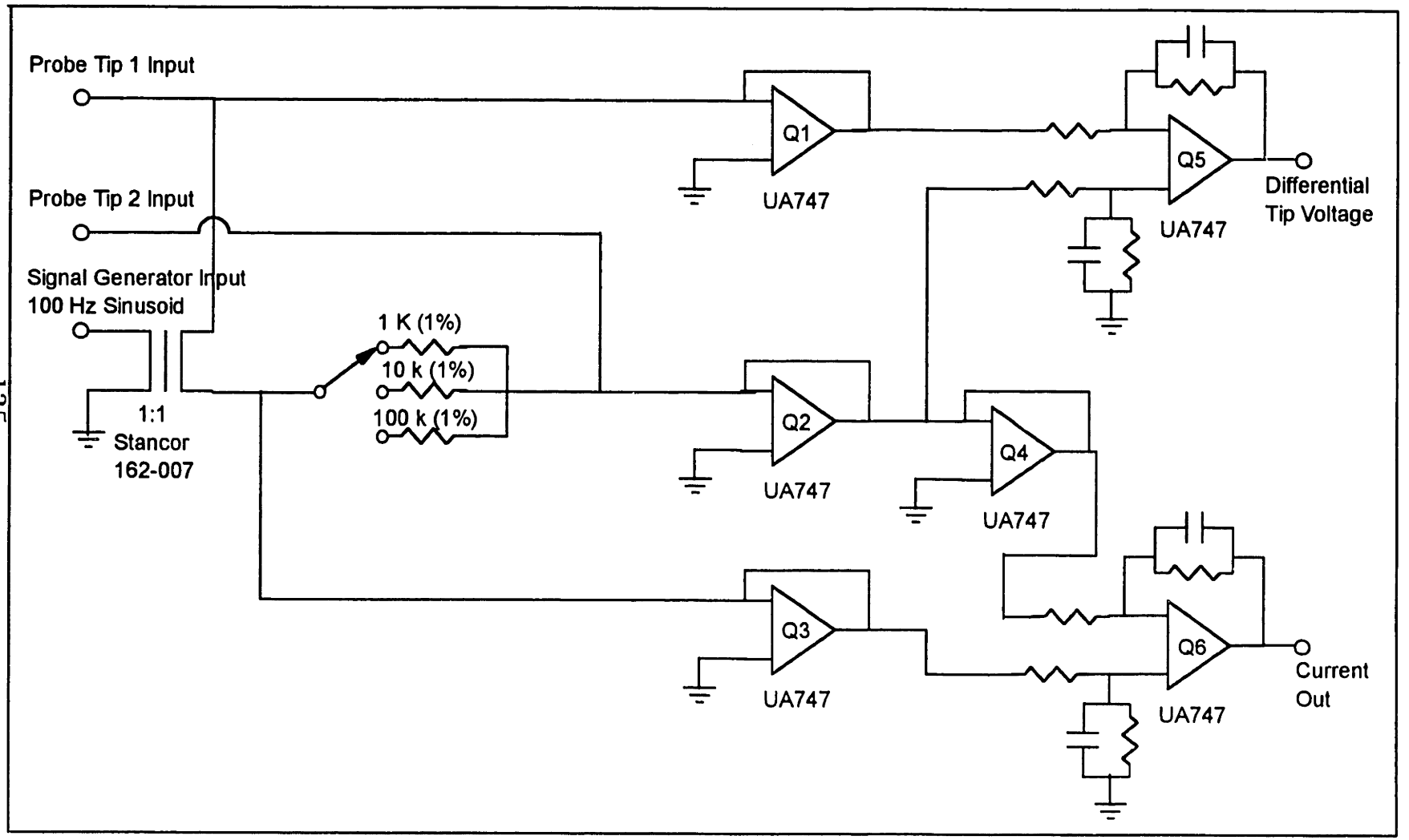

Figure A-2: Current and Voltage Measurement Circuit for Floating Double Langmuir Probe
All unmarked resistors are 1K (1%) and all capacitors are 1 uF.

voltage gain was switch-selectable over three decades (1, 10, and 100 V / mA). Voltages were picked off from the probe through op amp followers, Q's 1-3 (the uA747 has several MΩ input impedance), to insure that current measurements were not corrupted. The differential tip voltage was determined from a unity gain differential amplifier (Q5). The current between the tips was read off from the switch-selectable resistor voltage differentially amplified by Q6. Q4 simply buffered the output from Q2.

Bibliography

[Arfken, 1985] Arfken, G, *Mathematical Methods for Physicists*, Academic Press, 1985.

[Bhatnager et al., 1954] Bhatnager, P.L., Gross, E.P., Krook, M., *Phys. Rev.* , 94 (1994) 511.

[Aydil et al., 1993] Aydil, E.S., Gregus, J.A., Gottscho, R.A., *J. Vac. Sci. Technol. A 11* (1993) 2883.

[Biondi, 1963] Biondi, M.A., *Phys. Rev. 129* (1963) 1181.

[Bowden et al. a, 1993] Bowden, M.D., Okamoto, T., Kimura, F., Muta, H., Uchino, K., Muraoka, K., Sakoda, T., Maeda, M., Manabe, Y., Kimura, T., *J. Appl. Phys. 73* (1993) 2732.

[Braginskii, 1965] Braginskii, S.I., *Transport Processes in a Plasma* in *Reviews of Plasma Physics* Leontovich, M.A. ed. Consultants Bureau, 1965.

[Bowden et al. b, 1993b] Bowden, M.D., Kimura, F., Muta, H., Uchino, K., Muraoka, K., Maeda, M., *J. Vac. Sci. Technol. A 11* (1993) 2893.

[Carl et al., 1991] Carl, D.A., Williamson, M.C., Lieberman, M.A., Lichtenberg, A.J., *J. Vac. Sci. Technol.* B *9* (1991) 339.

[Chen, 1965] Chen, F.F. *Electric Probes* in *Plasma Diagnostic Techniques*, Huddlestone, R.H. and Leonard, S.L. ed. Academic Press, 1965.

[Chen, 1984] Chen, F.F. *Introduction to Plasma Physics and Controlled Fusion,* Plenum Press, 1984.

[Dandl and Guest, 1991] Dandl, R.A., Guest, G.E., *J. Vac. Sci. Technol. A 9* (1991) 3119.

[Delcroix, 1987] Delcroix, J.L., Course Notes for Intorduction to Plasma Physics M.I.T. (1987).

[Gibson et al., 1994] Gibson, G.W., Sawin, H.H., Tepermeister, I., Ibbotson, D.E., Lee, J.T.C., *J. Vac. Sci. Technol. B 12* (1994) 2333.

[Goodman, 1989] Goodman, D.L., Ph.D dissertation, Dept. of Physics, M.I.T. (1989).

[Gorbatkin et al., 1988] Gorbatkin, S.M., Berry, L.A. and Roberto, J.B., *J. Vac. Sci. Technol. A 8* (1990) 2893.

[Hirschfelder, Curtiss and Bird, 1954] Hirschfelder, J.O., Curtiss, C.F., and Bird, R.B., *Molecular Theory of Gasses and Liquids*, Wiley, (1954).

[Hokin, 1987] Hokin, S.A., Ph.D. dissertation, Dept. of Physics, M.I.T. (1987).

[Hooper and Cohen, 1994] Hooper, E.B. and Cohen, R., Private Communication.

[Hutchinson, 1986] Hutchinson, I.H., *Principles of Plasma Diagnostics*, Cambridge, (1986).

[Kent et al., 1969] Kent, G.I., Jen, N.C., and Chen, F.F., *Phys. Fl. 12* (1969) 2140.

[Krall and Trivelpiece, 1986] Krall, N.A. and Trivelpiece, A.W. *Principles of Plasma Physics* San Francisco Press, 1986.

[Lane et al., 1989] Lane, B.G., Smatlak, D.L., Gibson, G.W., Sawin, H.H., Bourget, L., Post, R.S. *Investigation of Limiters in ECR Plasmas for Applications in Plasma Processing* 43rd Gaseous Electronics Conference, 1990.

[Mauel, 1985] Mauel, M. Ph.D. dissertation, Dept. of Electrical Engineering, M.I.T. (1985).

[Makin and Keck, 1963] Makin, B., Keck, J.C., *Phys. Rev. Lett. 11* (1963) 281.

[McKillop et al., 1989] McKillop, J.S., Forster, J.C., Holber, W.M., *J. Vac. Sci. Technol. 7* (1989) 908.

[Morozov and Solv'ev, 1966] *The Structure of Magnetic Fields* in *Reviews of Plasma Physics Vol. 2* Leontovich, M.A., ed. Consultant's Bureau, 1966.

[Musil and Zacek, 1972] Musil, J., Zacek, F., *Czech. J. Phys. B 22* (1972) 133.

[Nakano et al., 1991] Nakano, T., Sadeghi, N., Gottscho, R.A., *Appl. Phys. Lett. 58* (1991) 458.

[Porkolab et al., 1972] Porkolab, M., Arunasalam, V., Ellis, R.A., *Phys. Rev. Lett. 29* (1972) 1438.

[Porteous et al., 1994] Porteous, R.K., Wu, H.M., Graves, D.B., *Plasma Sources Science and Technology, 1* (1994) 25.

[Rosenbluth and Simon, 1965] Rosenbluth, M.N., Simon, A., *Phys. Fluids 8* (1965) 1300.

[Sadeghi et al., 1991] Sadeghi, N., Nakano, T., Gottscho, R.A. *J. Appl. Phys. 70* (1991) 2552.

[Samukawa, 1994] Samukawa, S., *J. Vac. Sci. Technol. B 12* (1994)112.

[Sigmar, 1989] Sigmar, D., Course Notes for Plasma Transport M.I.T., 1989.

[Simon, 1959] Simon, A., *An Introduction to Thermonuclear Research*, Pergammon(1959).

[Stevens et al., 1992] Stevens, J.E., Huang, Y.C., Jarecki, R.L., Cecchi, J.L., *J. Vac. Sci. Technol. A 10* (1992) 1270.

[Vestal et al., 1978] Vestal, M.L., Blakley, C.R., Futrell, J.H., *Phys. Rev. A 17* (1978), 1337.